

KAUNAS UNIVERSITY OF TECHNOLOGY

**ANDRIUS SAKALAUSKAS**

**PROCESSING AND ANALYSIS OF TRANSCRANIAL  
ULTRASOUND IMAGES**

**Doctoral Dissertation  
Technological Sciences, Electrical and Electronic Engineering (01T)**

**2015, Kaunas**

The dissertation was prepared at Kaunas University of Technology, Biomedical Engineering Institute in 2010–2015. Research was funded by the Research Council of Lithuania.

**Scientific Supervisor:**

Prof. Dr. Habil. Arūnas LUKOŠEVIČIUS (Kaunas University of Technology, Technological Sciences, Electrical and Electronic Engineering – 01T).

**Internet website where dissertation is published:**

<http://www.ktu.edu>

**The Language Editor:**

Brigita Brasienė

## ABBREVIATIONS

AC – active contour  
ACM – active contour model  
APS – atypical Parkinsonian syndromes  
ASSM – amplitude based statistical shape model  
AUC – area under the curve  
AVI – audio video interleaved  
B-A – Bland-Altman  
BBB – blood brain barrier  
CNR – contrast to noise ratio  
CR – classification ratio  
CSF – cerebrospinal fluid  
CT – computed tomography  
DBS – deep brain stimulation  
DoG – difference of Gaussians  
EI – echogenicity index  
EO – early onset  
ET – essential tremor  
EX – expert  
FEM – finite element mesh  
FtF – frame to frame  
FtR – frame to reference  
FWHM – full width at half maximum height  
GLCM – gray-level co-occurrence matrix  
GVF – gradient vector flow  
HD – Hausdorff distance  
HDP – hereditary degenerative parkinsonism  
HIFU – high intensity focused ultrasound  
ITB – insufficient temporal bone  
K-S – Kolmogorov-Smirnov test  
LO – late onset  
LUHS – Lithuanian University of Health Sciences  
MCE – misclassification error  
MCI – mild cognitive impairment  
MoI – moment of inertia  
MRI – magnetic resonance imaging  
MSA – multiple system atrophy  
PD – idiopathic Parkinson's disease  
PET – positron emission tomography  
PSF – point spread function  
PSSM – phase based statistical shape model  
RF – radio frequency  
RMSE – root mean squared error  
RN – red nuclei  
ROC – receiver operating characteristic

ROI – region of interest  
RROI – reduced region of interest  
SD – standard deviation  
 $Se$  – sensitivity  
SeP – secondary Parkinsonism  
SFA – averaging of selected frames  
SFS – sequential feature selection  
SN – substantia nigra  
SNR – signal to noise ratio  
SOI – structures of interest  
SoS – speed of sound  
 $Sp$  – specificity  
SP – supranuclear palsy  
SPECT – single photon emission tomography  
SSM – statistical shape model  
STIF – spatio-temporal inverse filtering  
SVM – support vector machines  
TCS – transcranial ultrasonography  
TGC – time gain compensation  
TH – tyrosine hydroxylase  
THI – tissue harmonic imaging  
TR – time-reversal  
UD – unclear clinical diagnosis  
UP – raw (unprocessed) frame  
US – ultrasound waves  
UTC – ultrasonic tissue characterization  
WHO – World Health Organization

# Contents

INTRODUCTION .....	7
1. ANALYSIS OF THE STATE AND CURRENT TRENDS IN THE TRANSCRANIAL IMAGING .....	11
1.1. Idiopathic Parkinson disease diagnostics methodology and the role of transcranial ultrasonic imaging.....	11
1.2. Anatomy of the midbrain .....	13
1.3. Methodology of TCS examination.....	15
1.4. TCS technical and methodological limitations .....	18
1.5. TCS diagnostic value .....	24
1.6. Recent developments in TCS.....	26
1.6.1. Technical improvements in transcranial scanning equipment .....	26
1.6.2. Related works in the TCS image processing .....	33
1.6.2.1. TCS image segmentation algorithms.....	34
1.6.2.2. Automated TCS image analysis approaches .....	38
2. THE EXPERIMENTAL INVESTIGATION OF TCS IMAGING LIMITATIONS .....	45
2.1. Evaluation of the spatial resolution of ultrasound scanner Voluson 730 Expert	45
2.2. Investigation of the TCS intra-observers variability .....	54
2.3. Limitations due to the planimetry in TCS .....	55
2.4. Conclusions of the 2 <sup>nd</sup> chapter .....	57
3. THE PROPOSED TCS IMAGE PROCESSING SYSTEM .....	58
3.1. Multiplanar suppression of noise in TCS images .....	60
3.2. Automated algorithms for the midbrain segmentation.....	64
3.2.1. Shape modelling based approach.....	64
3.2.1.1. Statistical shape model .....	64
3.2.1.2. Detection of midbrain boundary points based on the local phase congruency .....	66
3.2.2. Active contour based approach.....	69
3.3. Segmentation of intra-mesencephalic brain structures.....	72
3.3.1. SN region extraction algorithm.....	72
3.3.2. The segmentation of reduced intra-mesencephalic region .....	75

3.4. Parameters and methodology for the midbrain echogenicity assessment .....	78
3.5. Conclusions of the 3 <sup>rd</sup> chapter. ....	81
4. EXPERIMENTAL INVESTIGATION AND RESULTS.....	82
4.1. Results of multiplanar noise suppression in TCS images.....	82
4.2. Experimental results of the midbrain segmentation.....	85
4.3. The performance of the SN extraction algorithm .....	93
4.4. The results of proposed automated TCS echogenicity analysis system .....	96
4.5. Conclusions of the 4 <sup>th</sup> chapter.....	106
5. GENERAL CONCLUSIONS .....	107
REFERENCES.....	109
LIST OF THE PUBLICATIONS .....	120
APPENDIX 1: .....	123

## INTRODUCTION

### Research object

Algorithms for the automated segmentation and evaluation of the brain structures of interest for Parkinson disease (PD) diagnostics in transcranial sonographic images.

### Relevance of research and scientific problem

Idiopathic PD is one of the most frequent neurological movement disorders (second after Alzheimer). The incidence rate of PD is from 4.5 up to 19 cases per 100 000 population, making 0.3- 1.311 million cases worldwide per year (WHO, 2008). The incidence of the disorder is growing together with the aging of the population, and the dramatical increment of the neurological movement disorders is predictable in the upcoming 50 years. The main PD symptoms are progressing muscle rigidity, resting tremors, bradykinesia, disorders of posture and gait affecting quality of life and increasing the rate of mortality within PD affected individuals. The clinical symptoms of PD are non-specific and frequently overlap with the signs of other neurodisorders in the early onset of the disease. The research performed by London Brain Bank had shown that in 24% of cases (24/100) the clinical PD diagnosis was not confirmed after the post-mortem analysis. The main pathophysiological reason of PD is the loss of dopamine-producing cells. Most of the clinical symptoms of PD could be observed only when the mass (> 50%) of the motoneurons are lost (Fearnley et al., 1991). At present, there are no approved therapies for prevention of the PD (WHO, 2008). The main therapy of PD is based on uptaking levodopa group precursors that could get over blood brain barrier (BBB) and serve for an increment of dopamine concentration in the brain, thus alleviating the symptoms of PD. Deep brain stimulation (DBS) is as well finding the place in the treatment of the PD symptoms (Walter et al., 2011). These methods help to manage the symptoms of the disease and improve the quality of life left, but there is no cure for the PD up to date. However, the outcome and price of the treatment is directly dependent on the early beginning and selection of appropriate treatment strategy.

Unfortunately, there are no accurate and reliable biological or neuroimaging based characteristic PD biomarkers up to date. The diagnosis of PD is typically based on the clinical criteria. Functional imaging methods (SPECT, PET) are considered as a gold standard for PD diagnostics, but these techniques are limited due to cost and radiation to the patient. **Transcranial B-mode ultrasonography (TCS)** is one of the latest neuroimaging methods proposed for the evaluation of the brain parenchyma. TCS is a cheap, non-invasive and sensitive tool for the assessment of abnormalities in the brain. The earlier researches (Berg et al., 2008, Walter et al., 2004; Bartova et al., 2014) and clinical retrospective study performed at the Lithuanian University of Health Sciences (LUHS) (Laučkaite et al., 2012) demonstrated that the PD related brain abnormalities could be detected by TCS. It is assumed that the early stages of PD could be diagnosed by TCS. These findings turn

TCS into a promising tool for screening elderly people. However, TCS has certain limitations. Ultrasonic scanning is performed through the preauricular temporal bone. As a result, the ultrasonic waves (US) are attenuated and distorted in the skull bone layer, thus directly affecting the quality of the acquired images. The brain structures are hardly recognizable in the B-mode images, and only an experienced physician is capable to recognize and interpret the suspect regions in the brain. TCS is an experience demanding ultrasonic examination, having comparatively high intra-observers and inter-observer variabilities.

Such shortages of TCS reveal the scientific – technological problem: how to reduce observer’s variability of neurosonographic approach, thus increasing the objectivity of the examination? The formulated problem shows the demand of image processing algorithms for the automated extraction and evaluation of structures of interest (SOI) of the brain. The manual segmentation is strongly under influence by the quality of data in the ultrasonic imaging. These considerations turn into a **working hypothesis** for the thesis: the sonographic assessment of the brain structures could be automated, thus reducing observer’s variability and saving expensive time of the qualified neurosonologists. Furthermore, the automated image processing tools could serve for the training of the inexperienced neurologists and even for image-guided therapy, since the highly promising techniques for the brain treatment are already in the scientific research stage. An example could be the ultrasound-induced blood brain barrier opening technique, which uses focused ultrasound and microbubbles (Konofagou, 2012; McDannold et al., 2012).

**Aim of the research is** to develop and investigate the image processing system for the automated segmentation and evaluation of diagnostic transcranial ultrasound images.

### **Tasks of the research**

The following tasks were formulated in order to achieve the aim:

- To evaluate the characteristics (particularly spatial resolution) of the imaging system used for the TCS image acquisition and the main TCS technical and methodological limitations (planimetry, observer’s variability).
- To develop algorithms for the denoising and automated segmentation of the informative regions (the midbrain and substantia nigra) in the diagnostic B-mode TCS images.
- To propose a methodology for TCS image based on quantitative estimation of echogenicity degree in the midbrain region.
- To investigate and evaluate efficiency of the proposed image processing algorithms using diagnostic TCS images of the subjects having healthy and pathologically altered (hyperechogenic) midbrain.

## Scientific Novelty

- The novel, fast and efficient image processing algorithm for the extraction of the midbrain region was developed. A unique combination of experience-driven statistical shape model and amplitude-invariant local phase congruency based on acoustic boundary detector was proposed for the extraction of fuzzy boundaries of the midbrain in the TCS images.
- The novel noise suppression algorithm based on the compound of multiplanar data was proposed. It has been demonstrated that a significant ( $p < 0.05$ ) improvement of the image SNR and CNR could be achieved.
- The methodology for the automated evaluation of the midbrain echogenicity degree was provided. It has been shown that the proposed set of potential parameters overcomes the comparative methods based on the image moment invariants (Kier et al., 2009), spatial frequency analysis (Al-Zubaidi et al., 2013) and echogenicity index (EI) (Školudik et al., 2014) presented in the contemporary scientific literature.

## Practical value of the work

- The developed image processing system could serve as a tool for the acquisition of supplementary parameters for the midbrain echogenicity evaluation.
- Moreover, it could be used for the training of the novice neurosonographers to outline the brain structures of interest (midbrain and substantia nigra).
- The automated algorithm for midbrain extraction reduces the existing inter-observer and intra-observers variability.
- The proposed denoising algorithm significantly improves the SNR, thus making the images more convenient for the evaluation purpose.

The results of the research were presented in the following projects:

- “Application of transcranial ultrasound for diagnostics of neurodegenerative diseases”. No.: LIG-28/2010, work sponsored by the Research Council of Lithuania in the frame of the National Health Program of Chronic Non-Infectious Diseases;
- “Research of transcranial sonography biomarkers for diagnostics of Parkinson disease (NEUROSONO)”. Work sponsored by the by the Research, Development (Social, Cultural) and Innovation Fund of Kaunas University of Technology and Lithuanian University of Health Sciences.

## Statements under defence

1. The multiplanar suppression of acoustic interference and electronic noise improves the image quality significantly ( $p < 0.05$ ) from the point of view of SNR and CNR, thus making the TCS images more convenient for the visual evaluation purposes.
2. The novel, fast and efficient algorithm for the midbrain segmentation was developed. The differences between automatically evaluated midbrain

region and the reference evaluations performed by two experts were statistically insignificant ( $p \gg 0.05$ ).

3. The reliability of the proposed methodology for the midbrain echogenicity evaluation outperforms the other automated methods (Kier et al., 2009; Al-Zubaidi et al., 2013; Školudik et al., 2014), which were found in the contemporary scientific literature.

## **Approbation**

In total, the results of the dissertation were published in 11 publications: 2 papers were published in the foreign periodic journals referred in the Journals of the Master List of Thomson Reuters Web of Science (with impact factor), 2 papers were referred to in the periodic journals in the other international databases.

The results were presented in 8 international scientific conferences held in France (Berder) and Lithuania (Vilnius, Kaunas). In 2012 – 2014, a doctoral fellowship, granted by the Research Council of Lithuania, was received.

## **Structure and contents of the dissertation**

The dissertation consists of an introduction, four chapters, general conclusions, the list of references, the list of publications of the author and one appendix. The body of the dissertation is organized as follows:

1. The first chapter presents the TCS as a new neuroimaging modality and discusses its value in the spectrum of the techniques used in the diagnostics of the neurodegenerative movement disorders. Moreover, the main technological limitations and latest TCS developments are briefly introduced.
2. Second chapter introduces the equipment used for the TCS image acquisition. The results of experimental research illustrating TCS imaging limitations are presented.
3. Third chapter presents the concept of proposed TCS image processing system and gives the detailed description of the developed image processing algorithms.
4. The fourth chapter presents the investigation and results achieved when testing the proposed TCS image processing system with a real clinical data acquired at LUHS.
5. General conclusions are presented in the final chapter.

The overall volume of the dissertation is 126 pages, including 53 figures, 17 tables, 59 formulas and 160 bibliographic references.

## **1. ANALYSIS OF THE STATE AND CURRENT TRENDS IN THE TRANSCRANIAL IMAGING**

### **1.1. Idiopathic Parkinson disease diagnostics methodology and the role of transcranial ultrasonic imaging**

Nowadays, the idiopathic PD diagnosis is established by the experts of movement disorders considering the complex of (1) collected medical and family history, (2) results of neurological examination by using objective clinimetric scales (e.g. Unified Parkinson's Disease Rating (Goetz et al., 2007) or Hoehn and Yahr (Hoehn, Yahr, 1967) scales) of a patient and a summary of findings assessed by the medical imaging modalities. The clinical symptoms of PD (muscle rigidity, resting tremors and bradykinesia) are non-specific, especially in the early stages of the disease. The symptoms are as well found in other movement disorders: secondary or hereditary parkinsonism, essential tremor or in the multiple system degeneration. Even experienced experts have difficulties to differentiate these comorbid movement disorders correctly (Aerts et al., 2012). Up to 20% of the PD diagnoses are found to be false after the autopsy (WHO, 2008). There is no accurate biomarker of PD up to date. The loss of neuromelanine-containing dopamine-producing cells in the midbrain region, *substantia nigra* (SN) *pars compacta*, is the main pathophysiological reason of PD. It results in the denervation in pathways controlling major motor functions and thus progressing PD symptoms affecting quality of life and increasing the rate of mortality within the PD affected subjects. Single photon emission tomography (SPECT) and positron emission tomography (PET) are considered as PD diagnostics reference method in the spectrum of the neuroimaging modalities. The decreased uptake of ligand indicates the dopaminergic cell loss in the midbrain (Behnke et al., 2009). Unfortunately, the applications of these techniques are limited due to cost, radiation to a patient and their huge employment in health care departments. SPECT has a high (> 90%) diagnostic accuracy when separating between patients with neurodegeneration from the healthy subjects, but it does not differentiate PD and atypical parkinsonian disorders (Vlaar et al., 2007). Magnetic resonance imaging (MRI) is as well used to evaluate the brain structures. Conventional T1 and T2 - weighted MRI shows the brain volume decrement (atrophy), but in case of PD, a normal SN structure is found (Brooks et al., 2010). Diffusion weighted and diffusion tensor MRI has a diagnostic value in the differentiation of atypical parkinsonian syndromes (Brooks et al., 2010). Few detection approaches of movement disorders based on the biomedical signal analysis could as well be found in the contemporary scientific literature. The authors applied electrooculography (Christensen et al., 2012), voice analysis (Bocklet et al., 2011) and performed gait monitoring via accelerometry data (Mariani et al., 2013) in order to recognize PD affected subjects. The presented results look promising; however, these techniques are in the early development stage and are still not applicable in the clinical practice.

Transcranial B-mode ultrasonography (TCS) was proposed as a diagnostic technique for supporting the clinical diagnosis of PD in about 1995 (Becker et al.,

1995). It was demonstrated that TCS is a sensitive tool for detection of abnormalities of deep brain structures, particularly midbrain (Berg et al., 2008, Walter et al., 2004). TCS is a non-invasive, relatively cheap and harmless to the patient. The main biomarker of PD is a hyperechogenicity found in the cross-sectional B-mode image at the ipsilateral part of the midbrain. This phenomenon was discovered and described by Georg Becker and collaborators (Becker et al., 1995). Several studies (Walter et al., 2007; Berg et al., 2001 etc.) had demonstrated that up to 90% of PD affected subjects have a SN hyperechogenicity property. The causality of hyperechogenicity is undefined well, but the histological findings (Blazejewska et al., 2013; Damier et al., 1999), post-mortem (Berg et al., 2002) and animal studies (Berg et al., 1999) indicate that it is related to the transmutation of neuromelanin-containing cells into the iron related compounds. The mechanisms causing these changes are not clear and well defined up to date. There is a hypothesis that the hyperechogenicity occurs due to the regional iron accumulation and inflammatory processes. It can be predicted that this alteration results into the changes of the acoustic impedance of the medium of interest. TCS was recently involved in a broad family of the diagnostic instruments of movement disorders (in Lithuania, available since 2010). TCS has a substantial advantage to be compared with the other methods. It is supposed that the early stages of PD could be detected by TCS. The parkin and PINK gene mutation carriers, having an increased risk to evolve into PD, as well holds a hyperechogenicity property even before the clinical symptoms (tremor, rigidity of muscles etc.) could be observed (Hagenah et al., 2008; Walter et al., 2004). The research performed by Behnke et al. (2009) showed the relations between the results of TCS and PET investigating group of subjects with hyperechogenicity but without clinical symptoms of PD. Furthermore, in the case of atypical parkinsonian syndromes, the hyperechogenicity is not that frequent, thus showing the different origin of the disorders. These findings indicate that TCS has a potential to be applied for the early diagnostics of PD, since the SN hyperechogenicity correlates with the functional alterations in the brain. This is especially important, since it is supposed that the PD clinical diagnosis could be established only when more than 50% of dopaminergic cells are already damaged and it is predicted that PD presymptomatic phase lasts up to 5 years (Fearnley et al., 1991). The early treatment of the PD could slow down the neurodegenerative process and substantially increase the duration and quality of life left. TCS is indisputably valuable neuroimaging tool and provides unique information about the acoustic properties of tissue, mainly about the density and compressibility of a medium. The transcranial ultrasonic examination was recently officially approved as a valuable imaging modality for screening, diagnosis and differential diagnosis for PD. TCS was included in the recommendations by the European Federation of Neurological Society as approved diagnostics technique in 2013 (Berardelli et al., 2013).

## 1.2. Anatomy of the midbrain

This subsection briefly introduces the anatomy and main functional responsibilities of the midbrain and its internal structures, which could be identified by TCS in the *mesencephalic* scanning plane. Midbrain (lat. *mesencephalon*) is a posterior part of the brain situated at the end of a brainstem between the pons and interbrain (lat. *diencephalon*). The cross-sectional size of the midbrain is approximately  $6 \text{ cm}^2$  ( $3 \times 2 \text{ cm}$ ). Figure 1.1 (A) presents a sagittal cross-section of brain. The midbrain is responsible for the tones and posture of the body, eye movements and contributes to the transportation of visual and auditory information. A cross-sectional sketch of symmetric butterfly-shaped midbrain is presented in Fig. 1.1 (B). The majority of midbrain region is of relatively low-echogenicity. Figure 1.1 (C) presents TCS image with outlined midbrain region and its internal structures.

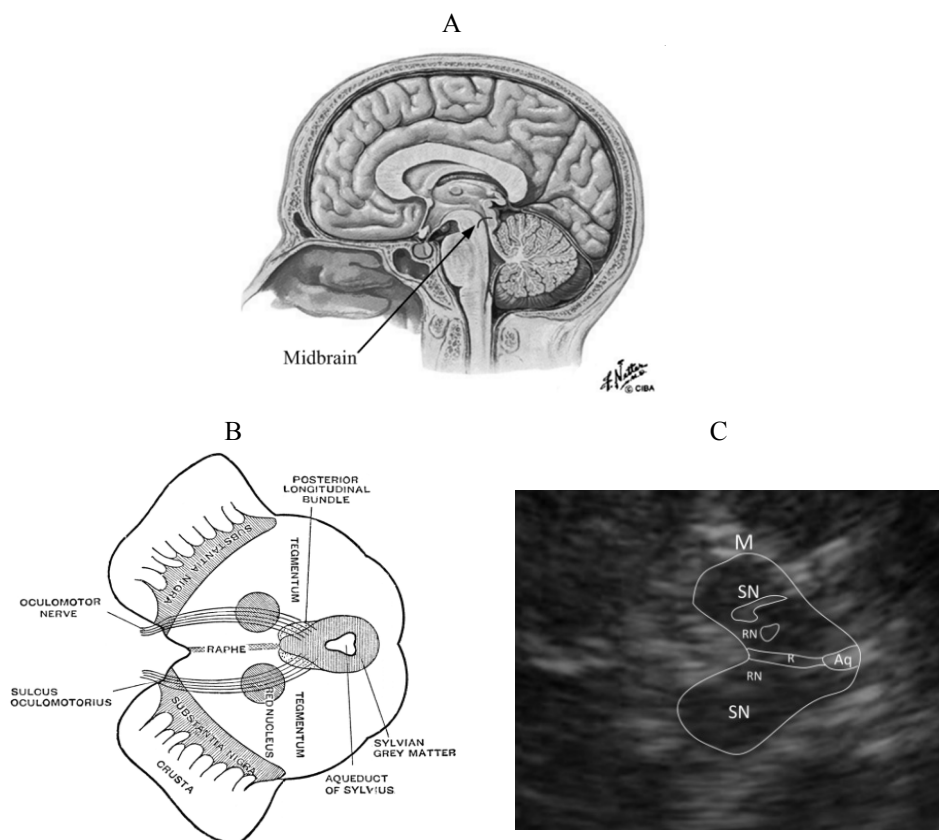


**Fig. 1.1** Anatomy of the midbrain and the main structures visualized by TCS: (A) sagittal plane of a brain (adopted from Netter F., 2011), (B) sketch of the axial cross-section of a midbrain (adopted from Cunningham D.J., 1972), (C) B-scan of the midbrain (mesencephalic plane) together with main structures identifiable by TCS: M – the midbrain, SN – substantia nigra, R – raphe, RN – red nuclei, Aq – aqueduct of Sylvius

The main structures of the mesencephalon identified by the TCS are *aqueduct of Sylvius*, *Raphe nuclei*, *Red nucleus* and *Substantia nigra*.

- *Aqueduct of Sylvius* is a channel in the central part of midbrain going longitudinally to the brainstem. It contains cerebrospinal fluid (CSF) and ensures the transport of CSF into the ventricular system from the third ventricle to the fourth. The walls of the structure are identifiable as two parallel echogenic short lines in acquired TCS image (see Fig. 1.1 (C)).
- *Raphe nuclei* (R) is a seam located at the medial axis of symmetric midbrain. Raphe serves as a dealer of serotonin into the other brain regions. The majority of neurons in this cluster are serotonergic. It was demonstrated that the grade of continuity of *raphe* evaluated via TCS image could serve as an indicator of depression (Becker et al., 1994, Berg et al., 2008).
- *Red nucleus* (RN), sometimes called *nucleus ruber*, is a structure located at the central part of midbrain bilaterally, dorsal to the substantia nigra. The fibers connect red nucleus with a motor cortex, *diencephalon* and *cerebellum*. The *red nuclei* take part in control of the muscle tone coordination, gait and posture. The nucleus is rarely identified in cross-sectional two-dimensional TCS images (an example is presented in Fig. 1.1 (C)).
- *Substantia nigra* (SN) is a stripe-shaped midbrain structure located bilaterally in the frontal part (“wings”) of the mesencephalon. The SN region is histologically divided into the *pars reticulata* and *pars compacta*, and these regions have different connections and functions. Both parts have an influence on dopamine production and respectively to the movements control. Dopaminergic cells of the *pars compacta* contain the dark pigment neuromelanin. Parkinson's disease is frequently interpreted as the death of dopaminergic neurons in the *substantia nigra pars compacta*. Figure 1.2 presents a comparison of anatomical cross-sections of midbrain in case of PD (A) and healthy adult (B).

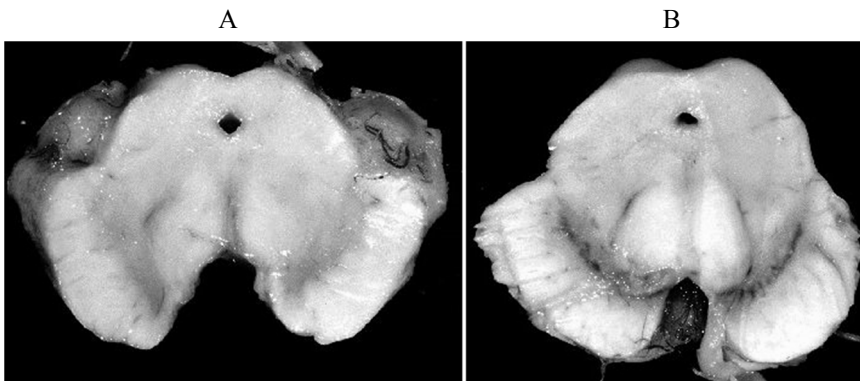


**Fig. 1.2** Anatomical cross-sections of the midbrain: (A) mesencephalon of PD affected subject (depigmented SN), (C) midbrain of healthy adult (adopted from Agamanolis et al., 2014)

The cells synthesize dopamine and connect to either the *caudate nucleus* or the *putamen*. Both are the structures of the basal ganglia involved in movement and

coordination control. The density of *pars reticulata* neurons is lower to compare with *pars compacta*. The thinner *pars reticulata* neurons are connected with the dopaminergic neurons of *pars compacta*. The *pars reticulata region* is responsible for the control of head and eye movement (stabilization of gaze, saccades).

Histologists (Damier et al., 1999a, Damier et al., 1999b) applied calbindin and tyrosine hydroxylase (TH) based staining of the *post mortem* midbrain cross-sections in order to define the nigral structure (Damier et al., 1999a) and PD caused patterns of dopaminergic cells loss (Damier et al., 1999b). TH staining was used for the recognition of dopamine-containing cells. It was reliably determined that 60% of all SN *pars compacta* dopamine containing neurons are within calbindin-rich zone, and it was named nigral matrix; meanwhile, other 40% are calbindin-poor dense clusters of dopaminergic cells. Calbindin-poor insertions of nigral matrix were divided into subregions and named nigrosomes (in total 5). Figure 1.3 presents the calbindin immunostaining representation of an intermediate cross-section of the *substantia nigra* (1 - 4 nigrosomes are marked). In the latter study, the Damier et al. (1999b) involved the PD cases. It was found that the majority of dopamine-containing cells are lost in nigrosomes, and the neurodegeneration starts at the largest nigrosome 1, and it is the most intense closer to the pons. The loss of dopaminergic neurons within nigrosomes was significantly larger in comparison to the loss in the nigral matrix. These studies confirmed the hypothesis that neuronal loss within SN is heterogeneous and showed that the

nigrosome 1 is the region where the PD starts. It was demonstrated (Blazejewska et al., 2013) that the largest nigrosome 1 could be visualized and identified as an individual hyperintense structure by 7T T2-weighted MRI scans in the control group. With an occurrence of PD, the contrast between nigrosome 1 and nigral matrix in MRI scans is lost. Even 3T MRI could be applied for the assessment of substantia nigra degeneration (Schwarz et al., 2011). These findings demonstrate that MRI scans could as well be used for PD diagnostics and even for early detection of PD. Unfortunately, >3T MRI is more an expensive tool of scientific researches than a technique used in a routine clinical diagnostics today.

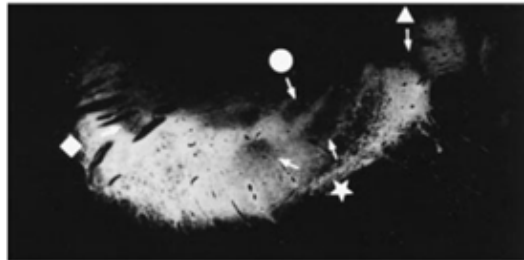


**Fig. 1.3** The calbindin immunostaining representation of an intermediate cross-section of the *substantia nigra*: ★ - nigrosome 1, ◆ - nigrosome 2, ▲ – nigrosome 3, ● – nigrosome 4 (adopted from Damier et al., 1999a)

### 1.3. Methodology of TCS examination

Methodologically, the TCS images are gained scanning through a posterior part of the relatively thin temporal bone, which serves as an acoustic window during

the clinical transcranial applications. The scanning performing operator presses ultrasound probe coupled with a conventional ultrasound coupling gel to the head of a patient in the area of temporal bone. The subjects are laid down into a supine position during the procedure. The transcranial examination could be called dynamic scanning because it is difficult to acquire a suitable image for the evaluation holding the transducer in a fixed position. A sonographer moves a transducer through the acoustic window changing its position and orientation, thoroughly searching for the brain structures that are under observation and seeking for the images which are the most appropriate for diagnostic evaluation. This procedure as well could be called the qualitative optimization of acoustic window, since the best quality images should be obtained where the skull bone layer is thinnest and the most homogeneous.

The sketch in 1.4 Fig. (A) presents the poses of ultrasound probe during the acquisition of informative planes used for the evaluation of brain structures. Three scanning planes are acquired bilaterally (see Fig. 1.4 (A)) if both temporal bones are “permeable”. *Mesencephalic (m)* plane for *substantia nigra* region assessment (the main plane for PD diagnostics) can be acquired when the ultrasonic transducer is mounted in such a position that the axial scanning plane is parallel to the eye line, or sometimes the term orbito-metal line of the skull is used (Berg et al., 2010). The echogenic areas of the midbrain, *substantia nigra*, *red nuclei* and *raphe*, could be identified in appropriately acquired images (see subsection 1.2.). The comparison of images of the same *mesencephalic* plane of the brain obtained by MRI and TCS is shown in Figure 1.4 (B and C).

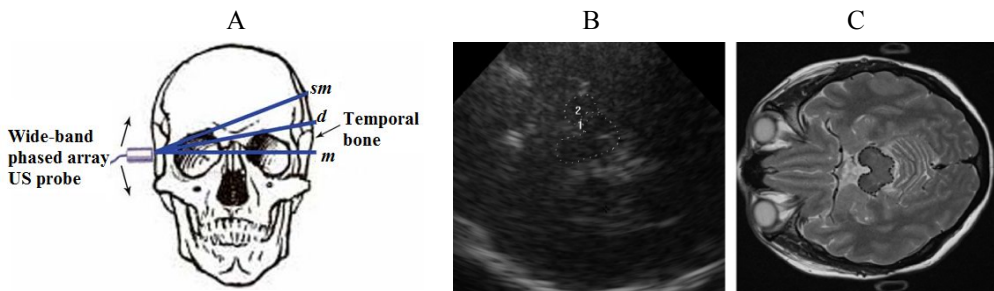


**Fig. 1.4** Methodology of TCS image acquisition: (A) sketch illustrating transducer positioning for acquisition of informative scanning planes: *m* – *mesencephalic*, *d* – *diencephalic*, *sm* – *sella media*, (B) *mesencephalic* plane with an example of manual delineation performed by neurosonologist (1 – midbrain region, 2 – SN), (C) an example of the same scanning plane in the MRI T2W image (SN region is hardly identifiable)

The butterfly-shaped midbrain area is outlined in both images. Moreover, the SN area is marked in TCS image inside the midbrain (marked by No. 2). Other structures of the brain are frequently evaluated using TCS. *Diencephalic (d)* and *sella media (sm)* planes could be acquired tilting the probe 15° - 25° upwards. These planes are used for the assessment of the ventricular system (widths of III ventricle, lateral ventricles); moreover, *caudate nuclei*, *nucleus lentiformis* could be evaluated qualitatively. The *diencephalic* and *sella media* planes are used for the detection of brain atrophy (e.g. dementia or age related atrophy) or hydrocephalus (Berg et al.,

2010) and are not discussed explicitly in the dissertation, keeping the focus on PD and mesencephalic scanning plane.

The routine manual evaluation of brain structures of interest (SOI) in the mesencephalic plane is performed outlining the echogenic SN area and the midbrain in the obtained image, after freezing it, and then zooming the threefold. The initial assessment of neurological condition of a patient is performed estimating the area and assigning echogenicity grade (from 0 up to 5) of the manually outlined SN region (Školoudik et al., 2007). At first, the operator manually outlines the midbrain region, which serves as a reference for the identification of internal structures. In the next stage, *substantia nigra* area is outlined in the “upper” half of symmetric midbrain (see Fig. 1.4 B). The size of SN area is evaluated bilaterally, performing scanning through the opposite-located preauricular temporal bone. The SN closer to the scanning probe is outlined in order to achieve better resolution. In some cases, the midbrain is even unidentifiable in the contralateral to the scanning probe side of the midbrain.

The parameters of the ultrasonic scanners used for the TCS slightly differ between the manufacturers. The “average” TCS scanning parameters were published by Berg and colleagues (Berg et al., 2008). The sectorial phased array ultrasonic probes with 64 or 128 acoustic elements are typically used for TCS. This selection is determined due to limited aperture caused by the area of the sufficient acoustic window. The area is smaller than 5 cm<sup>2</sup>. The transducers working in a relatively low frequency range (1-4 MHz, with fundamental frequency in a range  $f_0$ : 2-3.5 MHz) are typically used for the transcranial imaging. There are few papers where the images acquired by using tissue harmonic imaging (THI) mode is presented (Engel and Toennies, 2009; Plate et al., 2012), but in personal experience, the THI mode could be used very rarely (< 5%). Higher frequencies are attenuated in a skull bone layer, and only the subjects having relatively thin and homogeneous temporal bone layer could be examined by THI. Commercial ultrasonic scanning machines have only a few parameters to adjust: (1) scanning depth in 14-16 cm range (a bit deeper than the contralateral skull bone is found), (2) the gain and time gain compensation (TGC) of the received signals is case-dependent, and it is adopted observing the brightest point in an image (in order to avoid voltage clipping) by scanning performing operator, (3) dynamic range from 45 up to 55 dB, (4) gray mapping (dynamic) curve with a moderate suppression of low echogenic signals, (5) the transmit focal depth is adjusted in respect to the SOI (midbrain is found in 6-9 cm depth range); meanwhile, the automated dynamic multi-depth focusing is applied in a received mode.

The neurological evaluation is typically performed using digital images (JPEG, BMP) stored on a hard disk of the scanner. Digital images were used in the majority of researches later presented in the thesis. The main steps of the image formation engine starting from the reception of echosignals could be arranged: (1) beamforming of RF scanning lines – integration of appropriately delayed (multi-depth, dynamic focusing) signals received by active acoustic elements (number of scan lines depends on the number active transmit/receive elements); (2) RF signal

envelope detection using analytical signal (obtained via Hilbert transform); (3) logarithmic compression (done in order to arrange the echoes from different scanning depths at the same scale); (4) scan conversion (geometric arrangement of scan lines into a sector); (5) image formation: (a) interpolation of scan converted lines into a regular rectangular grid and (b) gray-scale mapping from ADC untints into 8BIT digital image. These steps are mandatory; meanwhile, there are some optional or user predefined steps (settings), such as (i) image processing algorithms (persistence-averaging, speckle reduction filters), (ii) gain engine (analog and digital gain and TGC) that are subject to manufacturer and (iii) the transmit focal depth.

#### **1.4. TCS technical and methodological limitations**

TCS is innovative and undoubtedly valuable tool for the assessment of the brain parenchyma. However, the quantity of diagnostic information provided by TCS is relatively small. The area of comparatively small (size varies from 0.05 up to 0.6 cm<sup>2</sup>) region in the two-dimensional B-mode image serves as the main PD indicator. The estimation of contrast between the SN plot and surroundings or basal cisterns could be employed as a potential parameter, but the amplitude based features are hardly comparable, since it depends on the properties of the path in which the ultrasonic wave travels. The main disadvantage of TCS is poor image quality, and this makes the PD diagnostic more subjective. Only experienced physicians can identify midbrain structures. The transcranial imaging suffers due to certain fundamental physical and methodological limitations, which have to be taken into account. The examination is performed through the temporal bone; therefore, the propagation of the ultrasound waves is affected by the attenuation and refraction of non-homogeneous layers of the skull bone. Vignon F. investigated temporal bone acoustic attenuation map (Vignon et al., 2009). The experiments *in vitro* were performed using two ultrasound probes: matrix array probe X7-2 (2500 elements,  $f_0=3.2$  MHz, bandwidth 2-7 MHz) driven by iE33 scanner (Philips Healthcare, Netherlands) and contralateral single element transducer ( $\varnothing=2.5$  cm,  $f_0=3.5$  MHz, focused at 14 cm) with the temporal bone sample between. Single element transducer served as an active point source; meanwhile, the matrix array probe was operating in a receiver mode. At first, the  $30 \times 30$  mm<sup>2</sup> area was scanned moving the system (beam) through the surface of the bone. In the next stage, the experiment was repeated without the sample in order to acquire a reference. The experimentally obtained an acoustic attenuation map (the authors did not provide the absolute attenuation values) was validated comparing with the optical (a photograph with backlight illumination) transparency of the bone (see Fig. 1.5). The single element probe was substituted by a wire phantom and scanned turning X7-2 probe into the pulse-echo mode. Firstly, the phantom was scanned selecting the probe position by visual evaluation of the obtained image, and thereafter the pose of the probe was optimized. The comparison of the images demonstrated that the contrast (image brightness was improved by 20 dB) and lateral resolution was a bit better after the adjustment of the probe position. In a later study (Vignon et al., 2013), the authors *in*

*vivo* demonstrated that optimal probe placement could noticeably improve the image quality scanning SOI through the thinnest and smoothest part of the bone.

Conventional ultrasound machines assume constant acoustic properties in the tissues. The speed of sound (*SoS*) in a temporal bone is more than 1.5 times greater (Fry et al., 1977) to compare with *SoS* in a soft tissue (1540 m/s) set in the ultrasonic scanners.

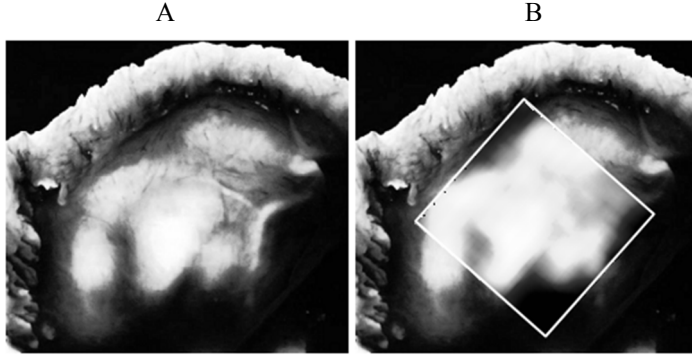


**Fig. 1.5** Acoustic attenuation map of temporal bone (adopted from Vignon et al., 2009): (A) optical transparency of temporal bone sample, (B) the same temporal bone fused with experimentally determined ultrasonic attenuation map

These *SoS* differences and varying thickness of the skull causes phase aberrations of the ultrasound waves. The shifts in arriving and transmission time for array elements have to be estimated. Phase aberrations  $\Delta\phi$  respective to skull thickness  $\Delta z(x,y)$  covered by transducers face could be expressed as (Ivancevich et al., 2009):

$$\Delta\phi = 2\pi f_0 \Delta z(x,y) \left( \frac{1}{c_s} - \frac{1}{c_B} \right), \quad (1)$$

where  $f_0$  – fundamental frequency,  $c_s$  – *SoS* in skull,  $c_B$  – *SoS* in the brain. The skull bone typically could be divided into the inner table ( $\sim 1.46$  mm), the diploe ( $\sim 2.29$  mm) and the outer table ( $\sim 1.49$  mm) causing 23.5 dB/MHz attenuation in total (Ivancevich et al., 2009). Furthermore, the sound energy absorption is spatially variable within the skull bone thus causing amplitude aberration (Vignon et al., 2001). Amplitude and phase aberrations cause distortions of ultrasonic beam and results in defocused images, which are out of the spatial resolution.

TCS examination is performed using phased array transducers operating at a relatively low frequency range (1-4 MHz), because the higher frequencies are strongly attenuated in a temporal bone layer. The used low frequencies limit spatial resolution of the TCS images. The spatial resolution of TCS images is much lower compared with the ultrasound images obtained during the scanning of the soft tissue: an axial resolution is 0.7 - 1.0 mm, and the lateral resolution is approximately 3.0 mm at a 6 - 9 cm depth, where the ROI structures are located (Berg et al., 2010); meanwhile, the resolution evaluated using the soft tissue mimicking phantom is approximately 0.5 - 1.0 mm, 1.0 - 1.5 mm, respectively (at the same depth and

scanning frequency). Walter and colleagues (Walter et al., 2011) aimed to evaluate spatial resolution of systems used for the transcranial scanning. It was reported that the conventional commercial ultrasound scanners (generation of late nineties) achieves resolution  $0.7 \times 3$  mm during the transcranial scanning (Berg D et al., 2010). The *ex-vivo* human skull was used in experiments. At first, the skull was immersed into a water tank in order to eliminate air and was filled with an ultrasonic coupling gel that has acoustic properties close to soft tissue. The Figure 1.6 presents the phantom used in the study. Two nylon thread meshes (thread diameter – 0.3 mm,  $0.8 \times 1.05$  mm, thread to thread distance) were mounted inside the skull and served for the evaluation of spatial resolution (see Fig. 1.6 (A and B)). Two ultrasound systems of different generations (former generation – Sonoline Elegra and present generation scanner Acuson Antares (both Siemens, Germany)) were tested during the experiments. The parameters of the both scanners were set close to the typical TCS settings used for *in vivo* examination: scanning depth 15 cm, high persistence, suppression of low echo signals (gray map curve),  $f_0 = 3$  MHz, 1 focal depth, dynamic range 50 dB. TGC and gain were adapted as needed for the image, which is the best quality respective to the subjective visual evaluation. The authors claimed that the progressive transducer manufacturing and real time speckle reduction signal processing techniques are the main superiority of the present generation ultrasound system. The detailed characteristics of the used probes and algorithms used for the image formation are not provided, but it is not surprising because the manufacturers do not disclose such information, and it is patent protected.

The phantom was as well scanned using two different MRI scanners (both 1.5 T in-plane resolutions  $0.31 \times 0.31$  mm and  $0.5 \times 0.5$  mm, respectively). The images obtained by TCS and MRI were compared analysing the visibility of meshes in axial and lateral directions. The investigation showed that the mesh network is clearly visible when thread to thread distance is 1.05 mm (at scanning depths between 55 and 86 mm). However, it was found that the lateral resolution is remarkably lower when the ultrasound machine of former generation was used (it was difficult to find the differences between the nylon threads). The same problem occurred with the images obtained by the MRI system with resolution  $0.5 \times 0.5$  mm, only the threads in 1.05 mm distance could be recognized as separate. It was concluded that the spatial resolution of MRI scans was higher, but the acquisition of data with resolution  $0.31 \times 0.31$  is time consuming, and it would be difficult to avoid patient movements (especially PD affected subjects). The movements distort spatial resolution, and this fact gives an advantage to TCS. The authors concluded that the high resolution in TCS could be achieved in comparison to MRI, but it should be mentioned that the only single skull was used in experiments; meanwhile, the properties of the bone is a decisive factor.

From 8% up to 20% of subjects (Mehnert et al., 2010; Berg et al., 2008; Vlaar et al., 2008; Okawa et al., 2007) cannot be examined by TCS, since both-sided temporal bones attenuates and distorts the ultrasonic waves too much, and the quality of acquired images is insufficient for the evaluation of brain structures. Approximately 15% of the subjects have an insufficient temporal bone (ITB)

property on one side. The curvature, thickness and homogeneity are the properties of the temporal bone affecting the transmission of the ultrasound beam through the cranium. The inhomogeneous structure of the middle trabecular bone has a higher possibility of attenuation and waves scattering (Kwon et al., 2006). Kwon et al. (2006) and Valdivia et al. (2004) reported that the osteoporosis is one of the most important causes of ITB. Then, the bone mineral density is reduced. ITB is most common among women and in the aged population, because these groups are the most affected by the osteoporosis.

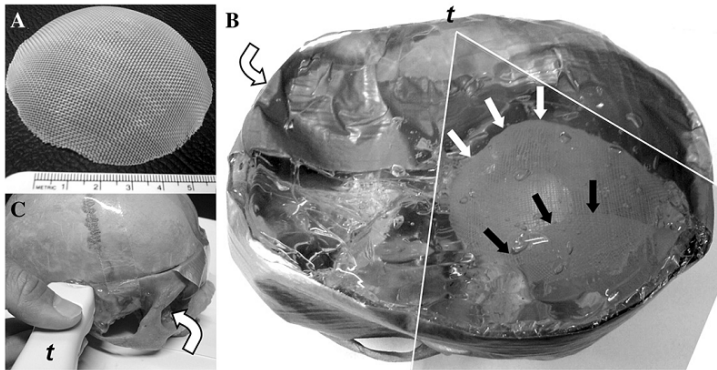


**Fig. 1.6** A phantom used for the spatial resolution evaluation: (A) nylon thread mesh ( $0.8 \times 1.05$  mm), (B) opened skull with a nylon thread meshes (arrows indicate meshes, shadowed area presents scanning plane,  $t$  position of US probe), (C) the closed skull together with the ultrasound probe ( $t$ ) (adopted from Walter et al., 2011)

The refraction of US waves is the other effect, which has to be discussed. The refraction occurs due to the differences of acoustic properties of the layers (skull/soft tissue and vice versa) which are scanned by the US. The refraction effects are the most noticeable when the incidence angle is sharper. Respectively, the lateral scanning lines are the most affected by the refraction. The acoustic differences in a skull and the soft tissue interface even results in the ultrasound wave's mode conversion. It has been shown that TCS suffers from the streak artefacts (Vignon et al., 2007). The theoretical computations and experiments *in vitro* proved that at the critical incidence angle ( $\sim$  approximately  $27^\circ$ ) US waves do not penetrate through the soft tissue-skull interface (Vignon et al., 2007). An example of a TCS image with streak artefacts is presented in Fig. 1.7 The incidence angle could be theoretically determined by a Snell's law:

$$\theta_{crit.} = \arcsin \left[ \frac{c_{L,soft\_tissue}}{c_{L,skull}} \right], \quad (2)$$

where  $c_{L,soft\_tissue}$  is the speed of sound in soft tissue (1540 m/s);  $c_{L,skull}$  is the speed of sound in the skull bone (3300 m/s according to Vignon);  $L$  indicates longitudinal waves. Furthermore, at higher incidence angles, the mode conversion from longitudinal to transverse occurs (see Fig. 1.7). The experimentally determined

acoustic properties of the human skull are presented in Table 1.1 The attenuation coefficient and *SoS* values determined by the different authors differ noticeably. The locations of skull (proportion of cortical and trabecular bone in a layer) and preparation of specimens are the main factors influencing the reproducibility of the assessment. Vignon et al. (2007) did not take into account the typical curvature of the sample during the experiments, and it should be noticed that the area of scanned temporal bone is relatively small. Respectively, the incidence angle of such order is relatively sharp. In personal experience, the streak artefacts are rare in TCS, but there are some cases when the artefacts are noticeable, and it is another factor limiting image quality and the ability to recognize the structures of interest for the examiner.

**Table 1.1** Acoustic properties of the skull

	c, m/s	$\alpha$ , dB/cm
White et al., 2006*	2840 ( $\pm$ 40)	1.2 ... 6.08
Pichardo et al., 2011**	<sup>a</sup> 2053 ... 2384 <sup>b</sup> 1937 ... 2140	<sup>a</sup> 2.9 ... 26.6 <sup>b</sup> 2.9 ... 32.6
Noiguera et., 2012***	1987 ... 2911	4.34 ... 34.74

\* determined at various measurement points of calvaria (attenuation estimated at 0.2...0.9 MHz), \*\* supra-orbital region of the skull (measured at 0.27-2.526 MHz, a – cortical bone, b – trabecular bone), \*\*\* determined at various measurement points of calvaria (frequency range 0.3 ... 1.5 MHz). In comparison to the typical acoustic properties in soft tissue ( $c = 1540$  m/s,  $\alpha = 0.5 \dots 0.7$  dB/cm at 1 MHz).

Other image quality affecting factor is noise. There are two sources of noise: acoustic interference and electronic (Baxter et al., 1999). Acoustic noise is the result of interference of ultrasound waves reflected from the distributed scatterers in a non-homogeneous media. It is frequently called a speckle noise (Burckhardt et al., 1978) and depends on the interference conditions: mainly on the position of a transducer and scanning frequency. Electronic noise is random and appears in the ultrasonic images, because the amplitude of noise, which is produced by the electronic circuits of the scanner and amplitudes of echo-signals, acquired from the deeper structures of the brain, becomes closer comparable, and the noise level is increased during the amplification of the echo-signals (Baxter et al., 1999). Speckle is the dominant noise compared with the random electronic noise. Wavelet based digital filters (Saad, 2006; Yue et al., 2006; Yoo et al., 2008), and anisotropic diffusion based algorithms (Yu and Acton, 2002; Aja-Fernandez and Alberola-Lopez, 2006; Lim and Williams, 2007; Krissian et al., 2007) were proposed for the reduction of the speckle noise in the ultrasound images, but the application of image filtering frequently causes the loss of important image details, such as texture patterns, or blurring edges of an image (Michailovich and Tannenbaum, 2006).

Planimetry is a certain methodological limitation of TCS, since TCS is a single plane evaluation. The selection of the scanning plane for the SN area evaluation is subjective and competence-dependent, thus limiting the repeatability and accuracy of sonographic assessment. The TCS examination is strongly dependent on skills

and experience of the scanning and evaluation performing neurosonologist. Firstly, it is time consuming to pose a probe on the appropriate acoustic window. Secondly, the resolution and contrast of the acquired images are relatively low, thus making the evaluation into challenging and non-trivial task.

Manual segmentation of the ROI structures results into the inter-observer and intra-observer variability, thus restricting reliability of the PD diagnostics. Školoudik investigated (Školoudik et al., 2007) the reproducibility in TCS evaluation.

Four experts (two experienced ( $> 6$  year) neurosonographers, less experienced ( $\sim 1$  year) and without experience) were involved in the study. The SN was evaluated quantitatively (area evaluations) and qualitatively (assignment of echogenicity grade) in 22 subjects. The TCS was performed twice by the first experienced expert (second examination

after a week), and the third examination was performed by the second experienced expert after a month. A Philips HDI 5000 ultrasonic scanner was used in the experiments equipped with P4-2 phased array probe (bandwidth 2-4 MHz). All the digital images used for the evaluation were stored in JPEG format. The correlations (intra-observer from two examinations, intra-observer from two evaluations, inter-observer variability between 3 experts with different experience and inter-investigator between two experienced experts) between these evaluations were determined. The study demonstrated that only an experienced sonographer is capable to reproduce the TCS reliably. The high (Pearson's  $r \geq 0.85$ ) and statistically significant correlation of the measurements performed by the experienced neurosonologist was achieved (evaluating the images collected during the single examination twice). Meanwhile, the correlations between the less experienced operator evaluations were unreliable. A lower correlation ( $r \geq 0.69$ ) was found between the evaluation of the images acquired in two sessions (both performed by the first expert). This finding demonstrates that the reproducibility is under the influence of acquired data as well. The inter-investigator correlation between the two experienced sonographers was as well a bit lower ( $r \geq 0.50$ ). All the images were collected by the experienced sonographers; therefore, it is difficult to weigh the reproducibility affecting components (appropriate scan plane acquisition and delineation of SOI). However, the lower agreement between the evaluations performed using the data acquired at different sessions demonstrates that it is a weighty factor in the neurosonographic assessment. It is supposed that the appropriate evaluation should be performed immediately after the image acquisition (*on-line*). The authors summed up that the automated algorithms for the SN area

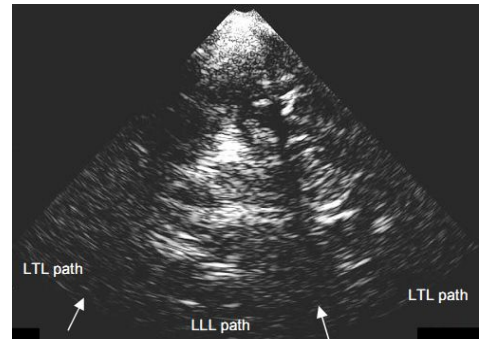


**Fig. 1.7** An illustration of streak type artefacts in the TCS image (streaks are marked by white arrows, L – longitudinal, T – transverse) (adopted from Vignon et al., 2007)

assessment could improve the reproducibility and reduce the variability within the neurosonographic estimations.

Taking into account all the summarized facts in this subsection and considerations made by the other authors, it could be concluded that the TCS is a tool finding a place in the routine diagnostics of movement disorders. The hyperechogenicity phenomenon is weakly explained up to date, and the pathophysiology is undefined well. It has been shown that the hyperechogenicity is as well found in about 10% of healthy subjects (Berg et al., 2008). Unilateral hyperechogenicity is as well frequently detected (up to 15%), but there is no clear correlation between the motoric symptoms and hyperechogenic SN side. It is supposed that the TCS could be used for the evaluation of risk to get PD. The longitudinal studies performed by Berg and colleagues (Berg D. et al., 2005) demonstrated that there are no significant differences in hyperechogenic SN size after 5 years follow-up. In total, 27 subjects were investigated twice (after 5 years from the first exam) with the same ultrasound machine. The significant differences between the evaluations were not found ( $p > 0.05$ : SN right  $r = 0.98$ ; SN left  $r = 0.53$ ); meanwhile, the significant disease worsening was determined according the clinimetric scales and symptoms. This fact was later confirmed (Behnke S. et al., 2013) in 50 PD patients (with 6.4 year average interval between exams). These findings reveal that the hyperechogenicity cannot serve as an indicator of a neurodegenerative process. The limited resolution, planimetry and other TCS constraints potentially limit the ability to follow the process by ultrasound, and the further technical improvements of TCS are mandatory.

### **1.5. TCS diagnostic value**

The diagnostic value of TCS and correlations with other biomarkers was investigated by few research groups (Okawa et al., 2007; Huang et al., 2007; Vlaar et al., 2008; Mehnert et al., 2010; Berg et al., 2010, Berg et al., 2011; Bowmans et al., 2014) up to date. The authors investigated PD affected subjects and patients having other movement disorders such as essential tremor (ET), other forms of parkinsonism (multiple system atrophy (MSA), supranuclear palsy (SP)) and as well searched how the TCS correlates with the other imaging modalities (MRI, SPECT), clinical symptoms and the severity of the disease.

TCS was involved in the routine clinical diagnostics in Lithuania by the end of 2010. The retrospective study was carried out in the Department of Neurology at the Hospital of LUHS (Kaunas, Lithuania) during the year 2011. The aim of the study was to evaluate the diagnostic value of TCS and to establish threshold values of the biomarkers (mainly cut-off value for the maximum SN size) for the PD diagnostics. The main biomarker for PD recognition was manually evaluated the maximal area of SN. The clinical diagnosis made after the follow-up combining anamnesis and the results of the objective clinimetric scales served as a reference in this study. The majority of the PD patients had the early stage of the disease (80.3% were within 2<sup>nd</sup> stage, according to Hoehn and Yahr scale). The obtained sensitivity ( $Se = 94.3\%$ ) and the specificity ( $Sp = 63.3\%$ ) values separating PD from the rest of the cohort (in

total 329 subjects) indicated that TCS is a valuable tool for screening elderly people, but a relatively low specificity limits the ability to apply TCS as a primary test for the diagnostics of neurodegenerative movement disorders. It was determined that the specificity and sensitivity of TCS is relatively high when it is applied for the separation of PD and control group ( $Se = 94.3\%$ ,  $Sp = 83.3\%$ ); meanwhile, the specificity was low in the separation between PD and ET or atypical parkinsonian syndromes (APS), SP groups. Hyperechogenicity is as well frequently found in other parkinsonian syndromes (APS, HDP, SP). The cut-off value of the SN area was established using ROC curve. The maximal area under ROC curve ( $AUC = 0.891$ ) corresponded to the size of  $0.20 \text{ cm}^2$ , and it was determined by separating PD from the rest of the cohort. It should be mentioned that the majority of the excluded patients ( $n = 33$ ) with ITB were female (91.9%), indicating the apparent relation between the quality of temporal bone acoustic window and osteoporosis.

Bowmans and colleagues (Bowmans et al., 2013) recently published the results of the prospective study where 196 patients having various neurological disorders (PD = 102, APS = 24; without parkinsonism = 22 etc.) were examined by TCS and SPECT. The clinical diagnosis established after 2 years follow-up served as a reference in this study. Only 40% TCS sensitivity and 61% specificity was reported; meanwhile, the results of SPECT was  $Sp = 88\%$ ,  $Se = 66\%$ . These results bring some controversy comparing with the previously reported diagnostic accuracy. In the other study performed by Mehnert, TCS was applied for the PD affected and healthy control groups (Mehnert et al., 2010). In total, 400 subjects were examined by TCS (199 had clinical PD, 201 healthy controls), and impressive values of  $Se = 95\%$ , and  $Sp = 96\%$  were established. Huang performed a retrospective study of Taiwanese Cohort (Huang et al., 2007). Ninety PD patients and 192 control subjects participated in this study. PD group was split into two groups (40 with the early onset (EO) of disease and 50 with the late onset (LO) of disease, clinical symptoms appeared before/after age 50). A determined cut-off value of the SN was  $0.20 \text{ cm}^2$ . The obtained sensitivity and specificity:  $Se$  LO group – 85%, EO – 50% and  $Sp$  – 85%, 100%, respectively. The authors proposed to use a relative marker taking the ratio between the areas of SN and midbrain (SN/M). Surprisingly, the higher classification results were obtained by using SN/M: sensitivity LO – 92.5%, EO – 57.5%, specificity 92%, 97.5%. The authors Walter et al. (2003), Behnke et al. (2005), Bartova et al. (2014) had demonstrated that TCS has a potential to be used for the differentiation of atypical cases. In the clinical study (Behnke et al., 2005) of 102 PD patients, 34 MSA patients and 21 SP cases hyperechogenicity was found in 89% of PD cases and only in 25% of MSA cases; meanwhile, 39% of subjects affected by PSP as well had hyperechogenic SN. Hyperechogenicity were found only in 2/23 (9%) APS patients (Walter et al., 2003). The discoverers of the hyperechogenicity phenomenon (Berg et al., 2011) published the results of large longitudinal prospective study. In total, 1800 subjects older than 50 years without clinical PD symptoms were examined by TCS. After 3 years follow-up, 11 of them were affected by PD, and in 8/10 (one subject was excluded from a study due to ITB) the hyperechogenicity of SN was found previously. It has been demonstrated

that the relative risk of PD incidence is close to 18 times higher for the subjects with the SN hyperechogenicity property.

The previous researches and study carried out at the LUHS has proven that TCS is a promising tool for the diagnostics and early diagnostics of neurological disorders; finally, it has been noticed that the weakness of the method is a comparably low specificity, especially than differentiating between the PD and atypical PD syndromes. This brief summary revealed that the diagnostic value of TCS is still inconclusive and denotes it as an object of scientific researches. The specificity of TCS could be increased by combining results of TCS with biomarkers obtained by the other modalities and elaborating TCS.

## **1.6. Recent developments in TCS**

There are few research groups developing TCS technology. The related works are presented and discussed in this subsection. Two main directions of the elaboration were identified: (1) scanning equipment modifications – alleviation of the defocussing effects induced by a skull bone, ultrasonic 3D imaging of the brain and (2) image processing approaches aiming to employ automated algorithms for the evaluation procedure of brain SOI and supplement the set of routine biomarkers (size and grade of SN) by new informative features extracted by the means of image analysis.

### **1.6.1. Technical improvements in transcranial scanning equipment**

The supreme work developing TCS is done by Matias Fink and colleagues. M. Fink invented time-reversal (TR) technique (Fink M., 1992) for the adaptive focusing of acoustic waves. It is an iterative method based on acoustic reciprocity valid for the linear system. The reflection from a point target in a media is assumed as an impulse response of a system, and the transmission of time reversed version of it focuses acoustic waves on the source. The variability of the *SoS* and acoustic energy absorption depend on the of the skull local properties (proportion of the cortical and trabecular bones and porosity). “Therefore the phased array beamforming has to be adaptive (Aubry J.F., 2000)”. TR and spatio-temporal inverse filtering (STIF) were proposed for the aberration correction. It has been demonstrated that TR with amplitude compensation could reduce the level of side lobes to -20 dB (Aubry J.F., 2000), and the directivity pattern comparable to the transmission in water could be achieved by STIF. Aubry et al. presented the extension of the TR to transmit-receive focusing (Aubry et al., 2001). The transcranial focusing is especially relevant not only for the imaging purposes, but also for the application of high intensity focused ultrasound (HIFU) for the treatment of brain tumours. A few different approaches for the adaptive focusing of ultrasonic waves was proposed in recent years (Vignon et al., 2005; Aubry et al., 2006; White et al., 2005 Gateau et al., 2009; Osmanski et al., 2012). Vignon et al. (2005) proposed to use a system of two linear arrays for the non-invasive aberration correction. Fig. 1.9 (A) depicts the experimental scheme used for the acquisition of signals transmitted through the temporal bone using two linear arrays (128 elements, fundamental frequency 1.5 MHz). STIF was applied for the aberration correction:

$$\Gamma(f) = \tilde{\mathbf{H}}(f)^{-1} \cdot \Psi(f), \quad (3)$$

where  $\tilde{\mathbf{H}}(f)^{-1}$  is the inverse matrix of the systems transfer function,  $\Gamma(f)$  is the Fourier transform of the signals to transmit aiming to achieve  $\Psi(f)$ . In fully non-invasive approach, the two layers of the skull have to be taken into account. It was proposed to describe the system function as consisting of the two propagators. One of the transfer functions were determined (“predicted”) by the assumptions about the absorption and the phase shift in the bone layer. The experiments *in vitro* demonstrated that it is possible to soften the defocusing effects. Figure 1.9 (B) presents the beam profile before and after the STIF correction through the one half of the skull. Fig. 1.9 (C) shows the results when the full skull was used in experiments.

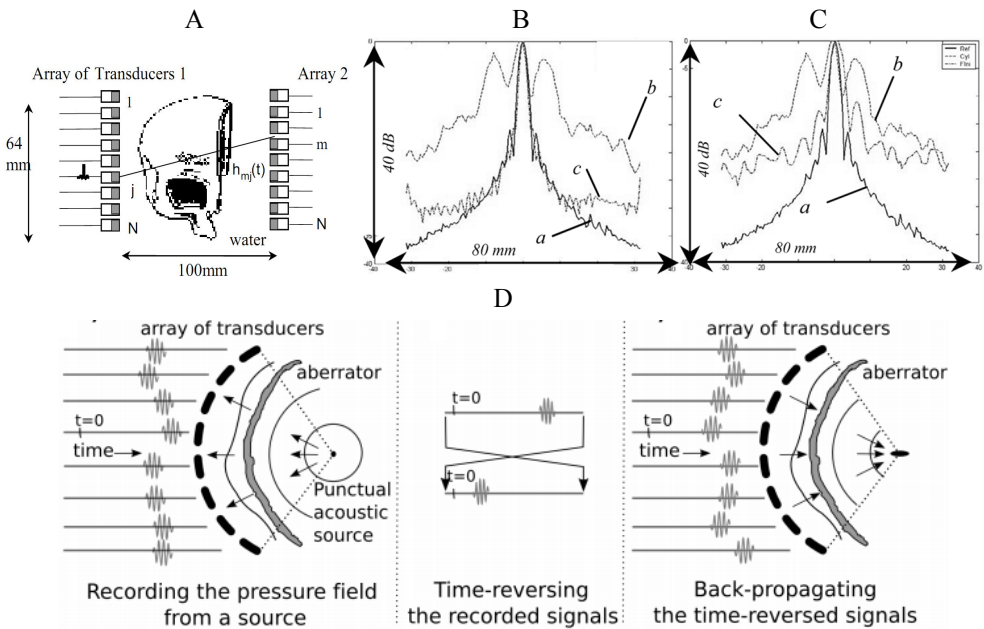


**Fig. 1.9** TR focusing: (A) the sketch of data acquisition procedure for the adaptive focusing; (B) cross-section of a pressure field in the focal plane (results of half skull experiment): a – focusing through water, b – focusing through skull (cylindrical wave front was sent), c – pressure field corrected by STIF (A – C adopted from Vignon et al., 2005); (C) cross-section of a pressure field in the focal plane (results of the experiment with the full skull); (D) scheme for the adaptive focusing using punctual acoustic source (adopted from Gateu et al., 2009)

A bit lower focusing quality in non-invasive case was achieved, but the level of side lobes was reduced noticeably. Aubry and colleagues patented the method and device for non-invasive adaptive focusing of acoustic waves in the heterogeneous medium (Aubry et al., 2006). The structural scheme of the device is presented in Fig. 1.12 (B). The device consisted of two transducers arrays forming imaging network and

target network (no. 5 and 6 in Fig. 1.12 B, respectively). The impulse responses of the medium are determined during the iterative procedure and the optimal set of signals, which has to be sent in order to focus US, is found for the imaging array.

The adaptive focusing has a certain limitations, since during such procedure the point source reflector in the brain has to be determined, and the reference signal has to be acquired from the focal spot in the brain. The partial compensation could be achieved using the multi-element transducer arrays for the acquisition of signals transmitted through the skull. These techniques are finding a place in the HIFU applications for the brain treatment. The cavitation bubbles induced by the short intense ultrasonic pulses were proposed as an active source inside the brain (Gateu et al., 2009). The feasibility study *in vitro* demonstrated that it is possible to generate cavitation bubbles acoustically and to use the reflected signals for TR. An illustration of the structural scheme applied to the time-reversal adaptive focusing using cavitation bubbles that are presented in Fig. 1.9 (D). Moreover, the aberrations could be partially compensated by using prior of skull bone profile (estimated density and *SoS* maps) obtained by computed tomography (CT) (Aubry et al., 2003) or even TCS itself (Aubry et al., 2002). MRI-guided adaptive focusing approach was presented by Larrat et al. (2010). Motion sensitive MRI sequences were used for the estimation of tissue displacement; thus, the indirect estimate of the ultrasonic beam intensity was established. This estimate served as a reference channel for the adaptive focusing and maximization of the ultrasonic wave intensity at one targeted point in space (Larrat et al., 2010). The speckle properties and dynamics arising due to pulsatility in tissues could be exploited for the TR based focusing (Osmanski et al., 2012). The echoes from moving tissue (for example, blood cells), could be used for the generation of the virtual point reflector.

The improvements in transcranial Doppler imaging were proposed by Ivancevich et al. (2006), Ivancevich et al. (2008). The authors implemented phase aberration correction and tested the technique applying for real-time three-dimensional Doppler imaging of brain vessels. The sparsed matrix array probe was used for the data acquisition. Figure 1.10 (A) depicts the sketch of matrix array probe and scanned pyramidal volume (Ivancevich et al., 2006). The multi-lag cross-correlation based method was applied for the phase shifts estimation. The needed transmitting and receiving shifts are estimated by the normalized covariance of the neighbouring ( $2 \times 2$ ) elements in receiving aperture. Figure 1.10 (B) shows a sketch of matrix array probe used for the transcranial scanning. In total, the array consisted of 440 active elements (all the elements used for transmission receive only elements marked by squares). The overlapping solid and dashed boxes demonstrates an example of the apertures ( $2 \times 2$ ) used for the focusing delay estimation in a neighbouring elements. The needed time-shifts  $\Phi$  is found by the following formula:

$$\Phi = (\mathbf{M}^T \mathbf{M}) \mathbf{M}^{-1} \mathbf{D}, \quad (4)$$

where  $\mathbf{M}$  is the matrix specifying the relation between the arrival times and time between the element pairs;  $\mathbf{D}$  is the vector of time shifts between the acoustic elements (Ivancevich et al., 2009). The time shifts are estimated preserving the

probe in the fixed pose. It was declared that all the delays are added and full calibration is achieved in approximately one minute. The experiments were performed using the electronic (simulated) and physical (phantom) aberrators, and it was shown that the proposed technique improves the contrast to noise ratio (CNR) significantly. The number of detectable cysts in the image of a phantom with an aberration layer was increased. Moreover, the clinical study was carried out. Fig. 1.10 (C) and (D) presents 3D image of brain arteries before and after the phase aberration correction.

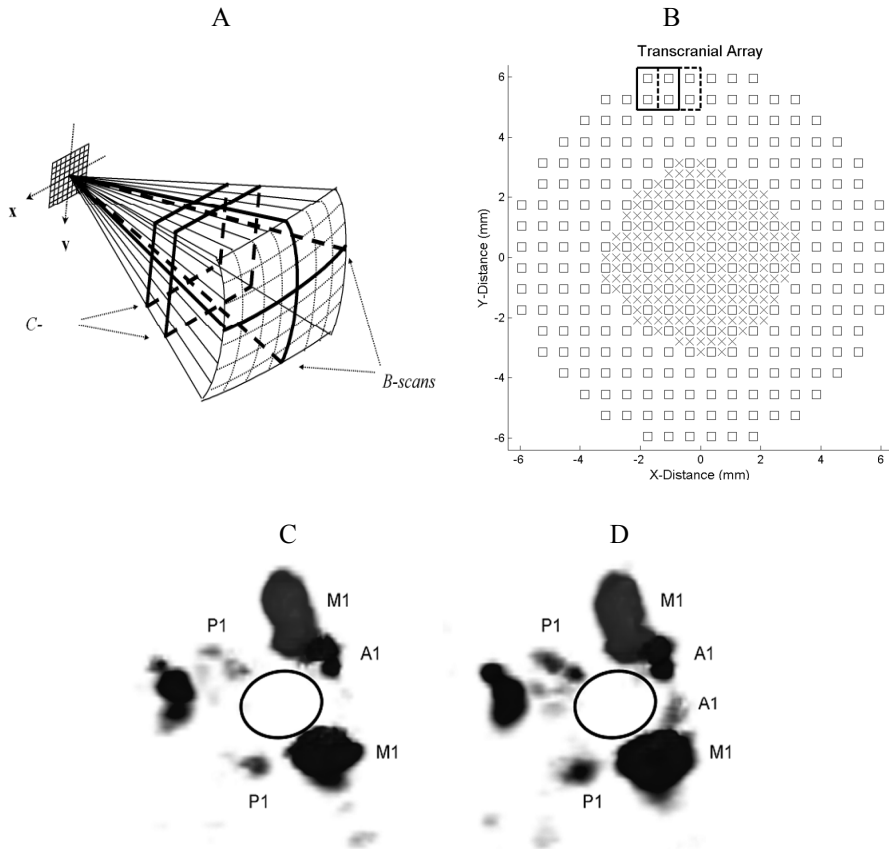


**Fig. 1.10** Phase aberration correction in Transcranial Doppler applications: (A) Sketch of 2D matrix array probe used for the visualization of pyramidal volume, (B) a matrix array probe front view (overlapping solid and dashed boxes demonstrates an example of the apertures ( $2 \times 2$ ) used for the focusing delay estimation, all the elements used for transmission, receives only elements marked by squares), (C) 3D volumetric image of Willis circle (aberrated), (D) 3D volumetric image of Willis circle after the phase aberration correction (adopted from Ivancevich et al., 2009)

The experts who evaluated the data observed that, in the most of the cases, the 3D volume of brain vessels is more informative after the aberration correction. It could

be noticed that some vessels (especially A1 segment) are even unrecognizable in the Figure 1.10 (C).

Philips Medical Systems (Vignon et al., 2013) developed a multistep approach in order to improve the transcranial image quality. The method consisted of three main independent stages. In the first stage, the optimal transducer position with respect to temporal bone was determined in order to improve SNR. Potentially, the thinnest and the smoothest region of the bone is found. Matrix array probe with a relatively large footprint ( $4 \times 2$  cm) was used in the experiments. The optimal scanning plane selection was based on the visual evaluation by scanning performing operator. Secondly, the receive sub-aperture aberration correction was applied. Time-shifts were estimated via cross-correlation between the received signals in the neighbouring acoustic elements similarly as it was performed by Ivancevich et al. Finally, the optimal Wiener post filtering was applied in order to achieve image contrast enhancement. The approach was tested using the synthetic data. It was demonstrated that the improvements in all three stages are achieved. However, the experiments *in vivo* showed that the diagnostically significant improvement (subjectively evaluated the amount of diagnostic information) was not achieved by the aberration correction. The TCS image quality was marginally improved by the optimal scanning plane selection and Wiener filtering (Vignon et al., 2013). The examples of TCS image after each processing stage provided by Vignon et al. (2013) are presented in Fig. 1.11.

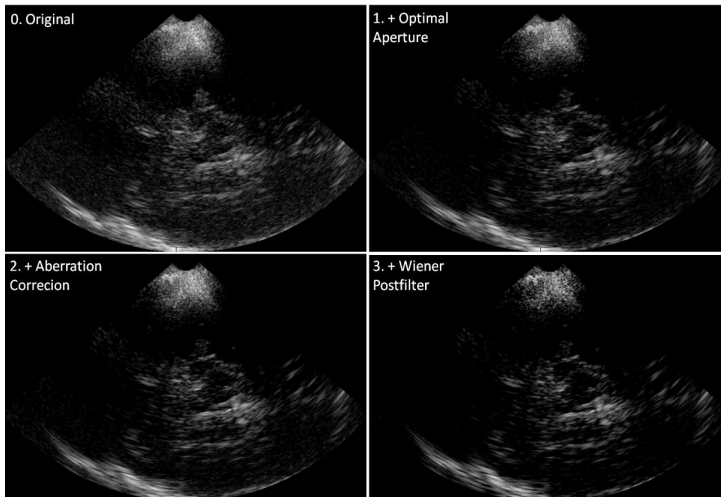


**Fig. 1.11** TCS image processing results after each stage of a multi-step approach (adopted from Vignon et al., 2013)

Červiakov et al. patented the device for high quality ultrasonic imaging of the brain with a correction of the aberrations. The structural scheme of a system is presented in Fig. 1.12 (A). The system consists of two matrix-array ( $20 \times 20$ ) probes (Fig. 1.12 (1) and (2)) mounted on the frame (3) and matched coaxially; 4 is the beam forming block, 5 – receiver, 6 – controller, 7 – image formation and processing block, 8 –

display. The frame could be shifted by precise stepper by a surface of the head. The ultrasonic signals transmitted through the skull are used for the calibration. The estimation of the additional delays and amplitude corrections are needed for transmit and receive focusing of the phased array probe. Unfortunately, there are no publications except the patent providing evidences about the efficiency of the proposed system and related products in a market today. It is relatively difficult to preserve transducer and the surface of head in a satisfactory contact, and comparatively huge amount of coupling ultrasound gel is used during the transcranial examination. Respectively, it can be predicted that it is complex to preserve the contact when the system is steered mechanically.

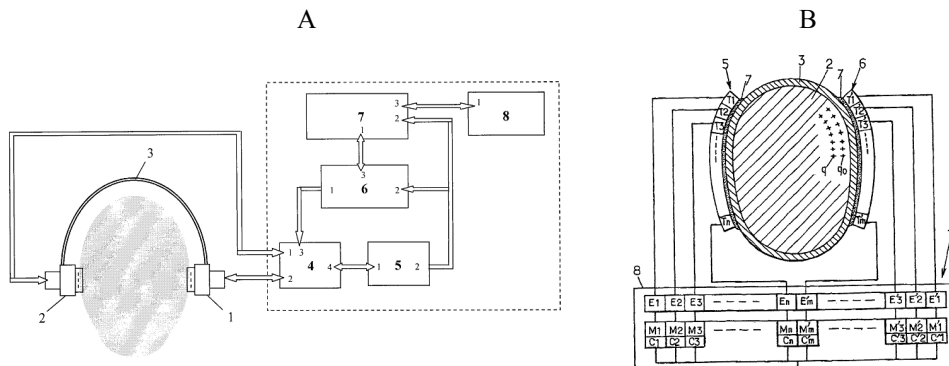


**Fig. 1.12** The schemes of patented transcranial imaging devices: (A) invented by Červiakov et al (adopted from Červiakov et al., 2008) and (B) invented by Aubry et al. (1 – imaging device, 2 – brain, 3 – the skull, 5, 6 – target and imaging arrays, 7 – layer of gel, 8 – block of electronics) (adopted from Aubry et al., 2006)

Recently, a research group in Munich (Plate et al., 2012) performed a pilot study with the aim to evaluate the potential of 3D sonography in the diagnostics of PD. The authors used a 3D freehand ultrasonic system for the transcranial scanning. A conventional ultrasound system equipped with phased array probe was supplemented with an optical position tracker (NDI Polaris Spectra, Northern Digital Inc.) for probe pose estimation. The experimental setup of a system proposed by authors is presented in Figure 1.13 A. In total, 23 subjects (11 PD affected and 12 healthy, 1 healthy subject excluded due to ITB) were examined during this study. All the subjects were scanned bilaterally. All B-scans were used for the volumetric reconstruction (the obtained size of the voxel is 0.45 mm). Surprisingly, THI mode having a substantially higher spatial resolution was used during the data collection; meanwhile, in personal experience, the application of THI is very limited due to ITB. Two observers performed manual segmentation of the midbrain and SN volumes of the right and left hemispheres in 3D datasets (more specifically in 12 reconstructed slices) using ITK Snap free software. The authors aimed to test the discrimination power of various volumetric parameters in separation of PD affected subjects and healthy controls. At first, the classification was performed using single-dimensional features such as:

- larger volume of SN,

- sum of SN volume in both hemispheres,
- normalized SN volume (volume of midbrain was used as a normalization factor),
- largest SN area in 2D cross-sectional slice.

ROC analysis revealed that 90.9% sensitivity and 63.6% specificity could be achieved then the threshold of larger SN volume is used as an indicator for the PD recognition. In the second stage, the combinations of various volumetric features were tested using supervised support vector machine classifier.

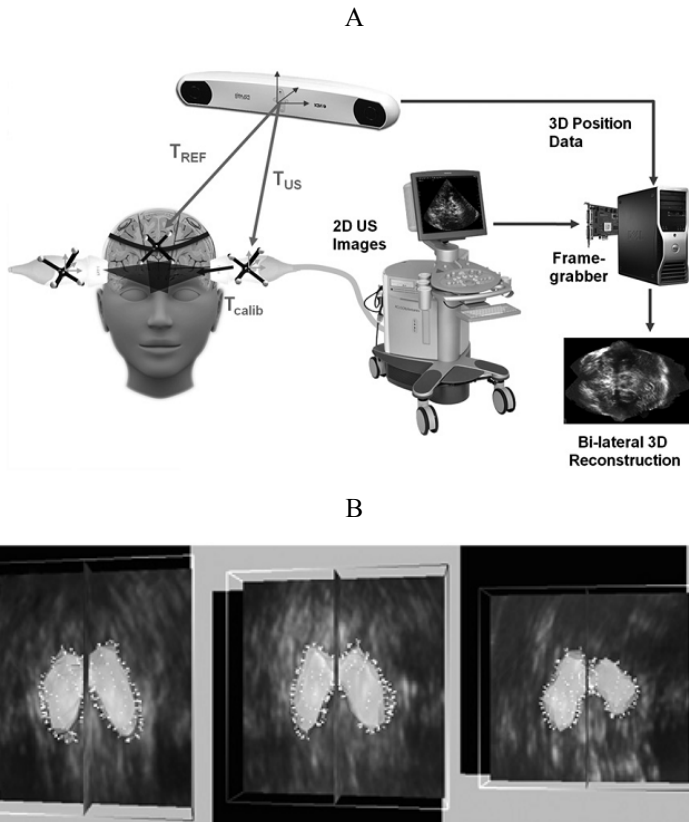


**Fig. 1.13** 3D freehand TCS: (A) the experimental setup of a system used for 3D TCS scanning (B) volumetric image acquired by TCS together with a reconstructed 3D surface image of the midbrain (adopted from Plate et al., 2012)

The best classification results were 90.9% sensitivity and 72.7% specificity when the volumes of both SN sides and volume of midbrain were used as features. The obtained classification results are relatively low. Similar or even better results were reported by the other authors (e.g. Mehnert et al., 2010) who used SN area threshold in conventional B-scans for the PD recognition, but in this study, the 3D features had a stronger discrimination power to compare with the SN area in a 2D slice. It is *per se* clear that the volumetric assessment increases the objectivity, since it is not

necessary to select the optimal scanning plane, and it is more informative to compare with the conventional 2D images. Furthermore, the bilateral data acquisition potentially reduces the dependency on acoustic window quality. It should be mentioned that the cut-off value of the larger SN volume was remarkably different for the two observers who performed segmentations of 3D datasets (first – 89.4 mm<sup>3</sup>, second – 76.4 mm<sup>3</sup>); moreover, the DICE coefficient (closely related to the spatial overlap) of the extracted SN volumes between the two observers was below 0.6. These results prove the existing inter-observer variability in the manual segmentations. The number of participants was the limitation of this pilot study. The representable sample should be examined in order to determine the reliable threshold values.

A survey of the developments in TCS equipment showed that there are some improvements proposed. The adaptive focusing techniques are finding the place in medical practice, especially in HIFU applications, such as thermal ablation of brain tumours (Coluccia D., et al., 2014) or sonotrombolysis in case of ischemic stroke (Eggers J., 2012). The aberration correction techniques are especially important for the targeted ultrasonic applications; meanwhile, the application of these methods for visualisation of brain parenchyma is in the very early development stage. Vignon (Vignon et al., 2013) demonstrated that the phase aberration correction marginally improves the image quality, and the additional value of diagnostics is debatable. Moreover, it has certain limitations concerned with the dynamics of scanning. Huge amount of delays has to be estimated and applied keeping the probe in a fixed pose, and slight movement of a probe or involuntary movements (PD tremor, blood flow pulsatility) of a subject requires refocusing. Furthermore, in the patented systems (Aubry et al., 2006; Červiakov et al., 2008), the second transducer array is necessary for the acquisition of signals transmitted through the skull. Reengineering makes the systems into less comfortable, since it is difficult to keep the probe in a satisfactory contact with the surface of the head. The efficiency and applicability of such systems in clinical practice are still inconclusive. 3D sonographic approach (Plate et al., 2012) is very promising, since the volumetric assessment of brain structures reduces the subjective component of the TCS. The concept of 3D ultrasound was proposed long ago (Howry et al., 1956), and the first system (Combison 330 Voluson, Kretztechnik AG, Austria) was developed in 1989. Unfortunately, 3D ultrasonic imaging is still finding the place as a routine tool in the clinical practice, and the transcranial applications are in the early beginning.

### **1.6.2. Related works in the TCS image processing**

There are few image processing and analysis approaches developed for the automated segmentation and quantitative image-based evaluation of the brain tissue. The main purpose of the segmentation techniques is the reduction of subjectivity (intra- and inter-observer variability) of the neurosonographic approach. The pursuance of TCS image features carrying supplementary diagnostic information has a potential to automate the detection of the pathology or even estimate the degree of it.

### 1.6.2.1. TCS image segmentation algorithms

A comprehensive review of the methods proposed for the segmentation of ultrasound images was presented by J. Alison Noble and D. Boukerroui. The authors overviewed segmentation techniques developed for the processing of echocardiographic, breast, prostate and intravascular B-mode ultrasound images. It could be summarized that the principle of deformable contour (active contours (AC) (Petroudi et al., 2012; Belaid et al., 2011b), statistical shape models (Yan et al., 2011; He and Zheng 2001) and level sets (Lin et al., 2003, Belaid et al., 2011b) are the most frequently applied for the fuzzy boundary detection in the ultrasound due to its robustness and adaptability.

A semi-automatic approach for the SN segmentation in 2D TCS images was proposed by Kier (Kier et al., 2007). The multi-step algorithm based on the morphological operators was applied for the extraction of the SN area in the ROI – ipsilateral to the scanning probe side of the midbrain, as it is performed during the manual assessment. The SN area extraction processing sequence is presented in Fig. 1.14. Firstly, the ROI was manually segmented by a physician; afterwards, the attenuating mask (constructed low-pass filtering a binary segmentation mask) was applied for the suppression of pixels outside the ROI and close to the ROI boundary (a-b); then, (c) the ROI image was converted into binary by a thresholding; the largest object was extracted applying morphological dilation and closing (d-i). The authors did not provide quantitative results or some proofs illustrating the algorithm's efficiency in the publication.

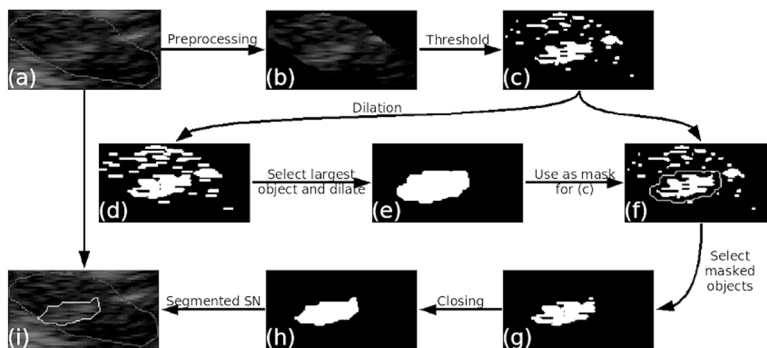


**Fig. 1.14** The scheme for SN segmentation algorithm proposed by Kier et al.: (a) manual delineation of the upper half of midbrain, (b) an attenuating mask is applied for the suppression of pixels which are away from the anatomical prior, (c) ROI thresholded into binary, (d) (h) morphological processing of binary image, (i) extracted contour of the SN area (adopted from Kier et al., 2007)

The proposed segmentation algorithm suffers from a few shortages: 1) the manual ROI selection could influence the accuracy of the segmentation, because the amplitudes of echoes from the midbrain surrounding *basal cisterns* (Berg et al., 2008) are of the same order as in the SN region; 2) the image conversion into binary is associated with certain information loss, and it is indicated that the threshold value

is determined heuristically, but it is well known that the echogenicity increases in the case of PD; meanwhile, in normal cases, the contrast is noticeably lower.

Engel and Toennies (Engel and Toennies, 2009) proposed computationally complex two-component deformable model for the midbrain and SN segmentation. The authors used learning-based strategy in order to determine characteristic geometric shape model and to model acoustic boundary using the local texture features. The finite element mesh (FEM) was used for the midbrain anatomy model construction from the discrete shapes. The FEM based strategy allows to simulate the deformations of the shape taking into account the elasticity properties. The model consisted of  $\tau^{(2)}$ , a global model of the midbrain, local models of bilateral SN  $\tau_i^{(1)}$ ,  $i = 1, 2$  (an example is given in Fig. 1.15 (A)). The components are connected in the virtual nodes  $\{\mathbf{x}_w^{(1)}, \mathbf{x}_v^{(2)}\}$ . The model was used for the dynamic search and fitting of the shape in the image frame. The search was performed via the optimization finding optimal pose (position, orientation and scale) and shape parameters of the global model nodes (midbrain). The pose of the local SN models is adjusted after the optimization of the global shape.

The authors applied learning-based method for the computation of the model evolution controlling the external image forces instead of the conventional edge map based on the gradient magnitude. The acoustic boundaries in TCS images are fuzzy, and there is no abrupt amplitude alteration at the borders due to the TCS limitations listed in the subsection 1.4. Engel and Toennies approached the noise-resistant and contrast-invariant external image force. The scheme used for the external image-based force computation is presented in Fig 1.15 (B).

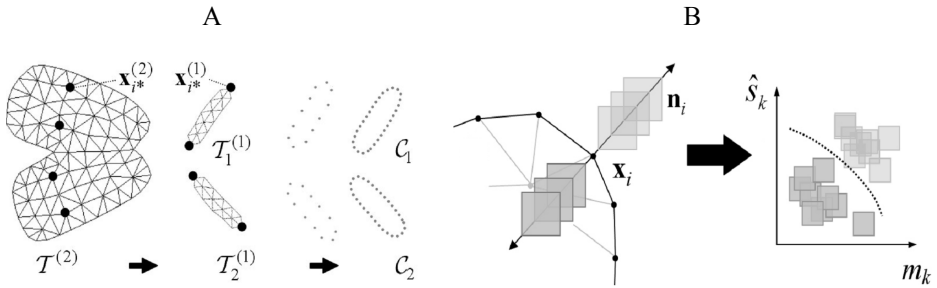


**Fig. 1.15** The two-component deformable model based segmentation of brainstem structures (adopted from Engel and Toennies, 2009): (A) two-component discrete shape model used for the initial shape search:  $\tau^{(2)}$  – global model of the midbrain,  $\tau_i^{(1)}$ ,  $i = 1, 2$  – local models of bilateral SN;  $c_1, c_2$  – contours used for the ACM segmentation of the SN bilaterally; (B) the principle of contour-attracting external force computation (where  $\mathbf{x}_i$  is  $i$ -th boundary node,  $i = 1 \dots k$ , normal to the contour –  $\mathbf{n}_i$ , gray rectangular windows mark the regions used for the estimation of local mean –  $m_k$  and variance –  $\hat{s}_k$ )

The researchers proposed to utilise the local image statistics (mean and variance) of the overlapping windows normal to the boundary nodes of the finite element model for the classification between the object/background categories. In the final stage of the algorithm, the refined SN segmentation is obtained by using an active contour model (ACM). The initial contours  $c_1, c_2$  (see Fig. 1.15 (A)) for ACM segmentation

are found assuming the boundary nodes of the previously adjusted local models of SN.

The proposed method was validated using images (pixel spacing between 0.13 mm and 0.27 mm) of 10 subjects (9 PD, and 1 healthy control). The manual delineations made by one sonographer served as a reference for quantitative evaluation of segmentation. The spatial overlap between the segmented regions and reference was comparatively high, taking into account the TCS image quality:  $90 \pm 3.1\%$  for the midbrain area and  $82.1 \pm 3.4\%$  for the SN, demonstrating that the proposed technique could be used for the TCS image segmentation. The drawback of the proposed technique is complexity. It is difficult to reproduce algorithm and the results on the basis of the paper published by Engel and Toennies (2009). The proposed algorithm is computationally expensive. The authors reported that the average time for the global midbrain area segmentation was 2733 s (by using average PC). It was indicated that the main load is caused by the external image forces map computation. The robustness to noise was expected if using the learning-based external energy computation method, but it should be mentioned that the TCS image properties, such as range of intensities, are sensitive to the user-predefined ultrasound machine settings and the quality of acoustic window. According to the personal comprehension, the learning-based boundary detection strategy is especially sensitive to such variation. However, the superiority of texture based on the external force to compare with the conventional low-pass filtered (Gaussian filter) amplitude derivative based on detector was demonstrated. The results of segmentation using Gaussian external forces were moderate for the midbrain:  $78.4 \pm 4.89\%$  and SN:  $71.5 \pm 6.76\%$ . The generalized efficiency of the method should be evaluated applying it to the data set obtained by at least two neurosonographers or by using data collected by few ultrasound machines. Furthermore, it was trained and validated using only 10 cases outlined by a single expert, and 90% of used images belonging to PD affected subjects. The SN segment is larger in the case of PD and is more in contrast with the surroundings to compare with the SN of the healthy controls. It is always easier to extract the SN in case of PD.

Ahmadi and Pauly (Ahmadi et al., 2011; Pauly et al., 2012) extended study performed by Plate et al. (see subsection 1.6.1.) and proposed algorithms for the segmentation of ROI in 3D sonographic data. Ahmadi aimed to exploit anatomical shape prior to the mesencephalon as it was done by Engel. The shape model of midbrain was constructed using the manual segmentations made by one sonographer and combined with a localized version of AC without edges (Chan and Vese, 2001). The model was controlled by minimizing the classical active surface energy functional consisting of two components:

$$E(S) = \int_{int S} f_i dx + \int_{ext S} f_e dx, \quad (6)$$

where  $S$  is the surface to fit,  $intS$ ,  $extS$  is the regions covered by  $S$  and outside  $S$ , respectively. The internal and external components in Chan and Vese model are generally expressed as (Ahmadi et al., 2011):

$$\left\{ \begin{array}{l} f_i = (I - v_{\text{int}}(x))^2, \text{ where } v_{\text{int}}(x) = \frac{\int_{\text{int}S} B(x) \cdot I(x) dx}{\int_{\text{int}S} B(x) dx} \\ f_e = (I - v_{\text{ext}}(x))^2, \text{ where } v_{\text{ext}}(x) = \frac{\int_{\text{ext}S} B(x) \cdot I(x) dx}{\int_{\text{ext}S} B(x) dx} \end{array} \right. , \quad (7)$$

where  $B(x)$  is the initial ball of predefined radius (6.75 mm was used by Ahmadi et al., 2011) having the centre at  $x=[x_0, y_0, z_0]$ . The authors compared the segmentation results and manual segmentations, which were assumed as a reference. The median DICE coefficient for the same 22 cases presented by Plate was 0.83 showing a moderate overlap between the manual and automated segmentations. It has been shown that only 0.55 median overlap is achieved when the un-localized model (Chan and Vese, 2001) is used, demonstrating that the global features are highly variable due to the specifics of the ultrasonic images. Figure 1.16 (A) presents the results of the midbrain segmentation (3 cases).

Pauly and collaborators (Pauly et al., 2012) developed and validated the 3D SN volume segmentation by the use of the dataset described above. The volumetric approach based on the random forests (Breiman, 2001) was proposed. The researchers formulated the SN voxels recognition problem as the joint probability of independent variables:

$$p(\varepsilon, V | \mathbf{x}, \mathbf{I}) = p(\varepsilon | \mathbf{x}, \mathbf{I})p(V | \mathbf{x}), \quad (8)$$

where  $p(\varepsilon | \mathbf{x}, \mathbf{I})$  is a data term, probability to observe the echogenicity  $\varepsilon$  at the voxel's spatial position  $\mathbf{x} = [x, y, z]$ , where  $\mathbf{I}$  is spatial intensity function,  $p(V | \mathbf{x})$  – anatomical prior (not dependant on the ultrasonic data),  $V$  – observation belonging to the SN volume. The averaged intensity values in overlapping cuboidal regions of different sizes were used as features for the training data term and anatomical prior taking into account the manually labelled midbrain and SN volumes. The unseen examples (voxels) are assigned as belonging to the SN volume, or vice versa setting the threshold of the estimated joint probability for each voxel in the previously segmented midbrain volume.

The authors reported comparatively high SN voxel recognition specificity and sensitivity, which was close to 83%. However, the averaged  $F$  measure of segmentations was only moderate (close to 0.5).  $F$  measure is expressed by:

$$F = \frac{2 \cdot TP}{2 \cdot TP + FP + FN}, \quad (9)$$

where  $TP$  – true positive (voxel correctly assigned to the SN),  $FP$  – false positive,  $FN$  – false negative. It is well known that the number of positive SN voxels is much lower to compare with the number of voxels in the midbrain volume (5 – 7 times). The 0.5 value of the  $F$  measure reveals that the SN volume is overestimated approximately twice as frequently. The authors did not use any post-processing in

order to filter single or relatively small connected sets of voxels which could be obtained due to the classifier based segmentation specifics. The Fig. 1.16 (B) presents an example of joint probability map obtained by the proposed algorithm. It could be noticed that there are regions with comparatively high probability at the midbrain boundary, which are clearly the result of echoes from the *basal cisterns*.

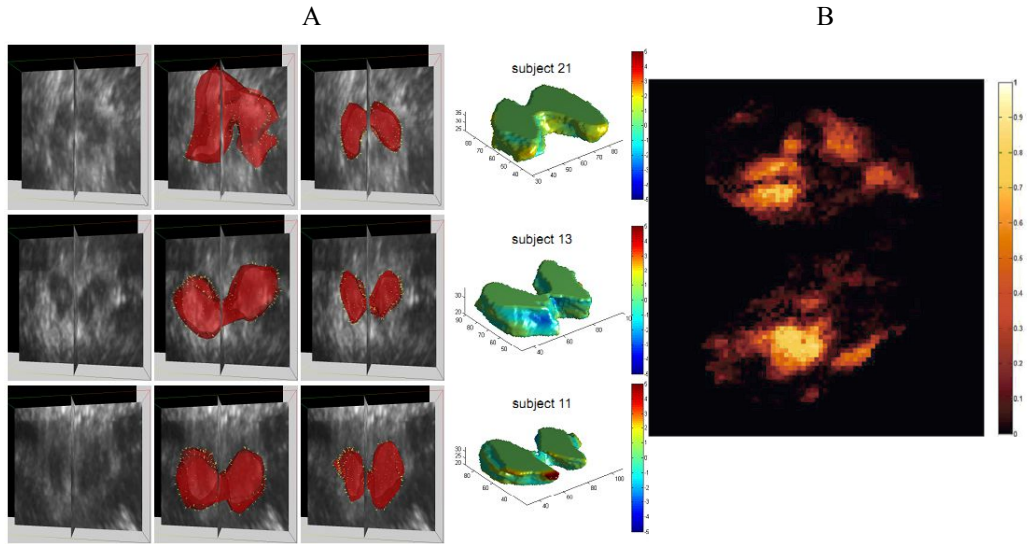


**Fig. 1.16** 3D sonographic approach: (A) an illustration of 3D midbrain segmentation (3 cases): midbrain meshes together with 2D TCS planes (left), reconstructed 3D surface images (right) of the midbrain (adopted from Ahmadi et al., 2011); (B) the joint probability map (in 2D cross-section) for the SN segmentation (adopted from Pauly et al., 2012)

### 1.6.2.2. Automated TCS image analysis approaches

The ultrasonic tissue characterization (UTC) becomes a leading area in the developments of medical ultrasonics in the recent years. The supplementary diagnostic information could be extracted by means of digital image processing or analysis of image forming radio frequency (RF) signals. RF data analysis was successfully applied for the intraocular tissue characterization (Jurkonis et al., 2012) and differentiation of tumours (Trumpaitis et al., 2014); moreover, the UTC was applied for the diagnostics of arteries (Takiuchi et al., 2000), liver (Audière et al., 2011) or hearth (Ciulla et al., 1997) etc. The RF analysis has superiority over the images, since the certain amount of data carrying potential diagnostic information is lost during the formation of B-scans. Unfortunately, the commercial ultrasound scanning machines do not allow utilizing RF data for the developments. However, the quantitative ultrasonic image analysis is not restricted and could be applied for the extraction of supplementary features for the automated recognition of the pathology or even for the estimation of the degree of the pathology. Few attempts to employ the image analysis for the recognition of PD related abnormalities and healthy subjects on the basis of TCS images could be found in the contemporary scientific literature. Kier et al. evaluated the potentiality of geometrical shift,

rotation and scale invariant moments for recognition of PD mutation carriers without the clinical PD symptoms. Authors manually segmented TCS images and defined the half of symmetric midbrain as ROI. An example of manually delineated ROI is presented in Fig. 1.17 (A). The seven Hu moments invariants (Hu, 1962) and moment of inertia of intensity values in ROI were evaluated expecting to identify the characteristic patterns for PD and healthy groups. The moment of inertia is expressed:

$$I = \sum_x \sum_y ((x - \bar{x})^2 + (y - \bar{y})^2) \cdot f(x, y), \quad (10)$$

where  $\bar{x}, \bar{y}$  are centroid coordinates of the ROI. The invariant Hu moments are derived from the central image moments (Kier et al., 2009):

$$\mu_{mn} = \sum_x \sum_y ((x - \bar{x})^m (y - \bar{y})^n) \cdot f(x, y), \quad (11)$$

where  $m, n = 0, 1, 2, \dots, N$ ,  $f(x, y)$  is an image of spatial intensity function. The central moments are shifted to the centroid of the image, thus obtaining invariance to shift. The invariance to scale is obtained by the following normalization (Kier et al., 2009):

$$\zeta_{mn} = \frac{\mu_{mn}}{\mu_{00}^\gamma}, \quad (12)$$

where  $\gamma = (m+n+2)/2$ ,  $m+n=2, 3, \dots, N$ . Hu (1962) derived seven moments invariants based on the normalized central moments.

Twenty-four subjects (14 healthy controls and 10 PD mutation carriers) were examined by TCS bilaterally during this study. The data set consisting of 39 images (9 images were excluded due to ITB) were used for the evaluation of the discrimination power of moment invariants. It has been found that the moment of Inertia and first Hu moment has a potential to be used for the recognition of PD mutation carriers. The differences of mean values of these features were statistically significant ( $p < 0.005$ ). The most informative first Hu moment is expressed as (Kier et al., 2009):

$$Hu_1 = \zeta_{20} + \zeta_{02}. \quad (13)$$

The scatter plot of the first Hu moment and moment of inertia values for both groups are presented in Fig. 1.17 (B).

ROC analysis revealed that close to 80% of sensitivity and specificity could be achieved by using these features. The weaknesses of this study were (1) comparatively small data set used for testing, (2) the knowing that one-sided hyperchogenicity is common for the PD patients, respectively careful selection of images used for testing should be performed, (3) the ROI area was outlined manually, thus leaving the method investigator dependent.

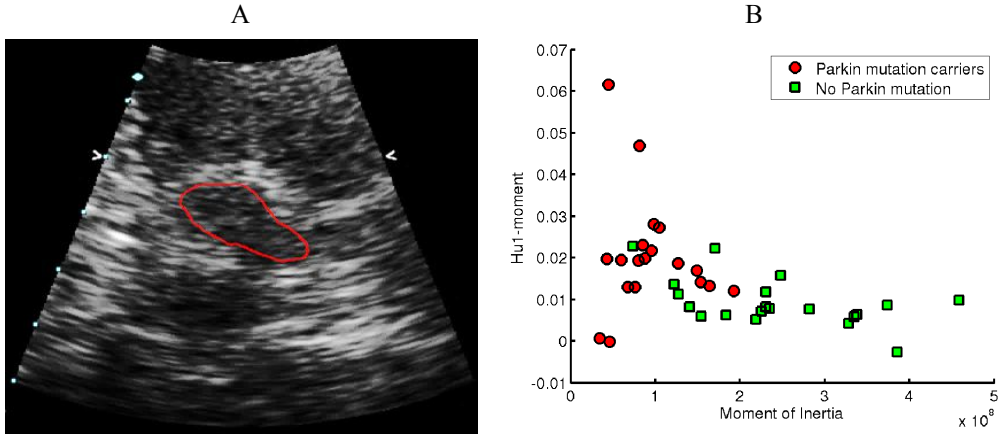


**Fig. 1.17** (A) TCS image together with the manually outlined ROI contour, (B) the relationship between the two most informative features (39 images) for both investigated groups: Hu1 moment and moment of inertia (adopted from Kier et al., 2009)

Recently Lei Chen proposed few strategies for feature extraction and recognition of PD affected subjects by using the transcranial images. Chen L. et al. extended the feature set proposed by Kier supplementing it by the features extracted applying a multiscale spatial frequency analysis of ROI (Chen et al., 2010). The directional Gabor filter bank was used for this purpose. The Gabor function in 2D could be defined as:

$$g(\tau, \eta) = \frac{1}{2\pi\sigma_\tau\sigma_\eta} \cdot \exp\left[-\frac{1}{2}\left(\frac{\tau^2}{\sigma_\tau^2} + \frac{\eta^2}{\sigma_\eta^2}\right)\right] \cdot \exp[2\pi i W\tau], \quad (14)$$

where  $W$  is the modulation frequency;  $\tau, \eta$  is the shift range of a filter. Mean and standard deviation of the filtered images served for ROI characterization, assuming that the enlarged hyperechogenic SN region affects homogeneity of intensities in ROI (Chen et al., 2010). The extracted features were combined into a vector and used for the classification applying linear support vector machines (SVM). In total, the feature vector consisting of 85 features was constructed: 15 statistical moments, geometrical moments proposed by Kier and 60 potential parameters extracted using Gabor filter bank (mean and standard deviation in 5 scales and 6 orientations). In total, 78 subjects participated in this study (36 healthy and 42 PD mutation carriers). The classification ratio of 76.92% (Se: 71.43%, Sp: 83.37%) was obtained by using the full feature vector. The authors applied feature selection strategy in order to obtain the optimal subset of features. Finally, an impressive classification ratio of 97.62% was achieved. An optimal subset of features consisted of the first Hu moment and 4 features extracted by the spatial frequency analysis. In the later study, Chen et al. (2011) supplemented the vector of texture features by gray-level co-occurrence matrix (GLCM) based on texture features. GLCM gives information about the relative positions of pixels having similar gray levels with respect to each

other. Four main features of GLCM: energy, contrast, correlation and homogeneity (Haralick et al., 1973), were used for the texture characterization in four directions  $\Theta = 0^\circ, 45^\circ, 90^\circ, 135^\circ$  (window size  $3 \times 3$ ). GLCM based features did not improve the results. The classification ratio using the full feature vector was only 65.45%; meanwhile, after the selection of optimal subset, it was 92.73% (the used dataset consisted of 36 healthy and 19 PD cases).

The research performed by Al-Zubaidi et al. observed that the proposed feature extraction strategies (Chen et al., 2010; Chen et al., 2011) are not invariant to the image acquisition circumstances. Firstly, the image properties, such as dynamic range, contrast, are dependent on the operator-predefined scanning settings (gain, TGC curve, focal depth, gray map curve etc.). These properties and quality of the used scanning system (electronic noise, the efficiency of the transducers) directly affects the features used for ROI characterization. Secondly, the orientation of the midbrain in a B - mode image depends on a relative probe-mesencephalon pose, and the features extracted by directional filtering are ambiguous between the cases. In order to overcome these barriers, Al-Zubaidi proposed robust strategy of feature extraction. The image equalization was used for the compensation of scanning parameters influence, and the rotation-invariant Gabor filter bank was applied for the feature extraction. Two approaches were proposed for the achievement of orientation-invariancy. Rotation invariant Gabor filter bank could be obtained summing up the filter responses from the different orientations at the scale  $m$ :

$$g_m(\tau, \eta) = \sum_{n=0}^{R-1} g_{m,n}(\tau, \eta), \quad (15)$$

where filtering scales  $m = 0, 1, \dots, s-1$ ,  $n$  is the filtering direction index ( $n = 0, 1, \dots, R-1$ ). In the second approach, the invariancy was obtained by sorting the features with respect to the total energy at predefined scale (starting from the component having the greatest energy). Three datasets acquired by different neurosonographers were used in the experiments. Altogether 38 healthy controls (71 images) and 39 PD patients (67 images) participated in this study. The 81.88% classification ratio was reached with an optimal feature subset. The feature set proposed by Chen (2011) was tested using this composite dataset, and only 69.56% classification ratio was achieved; meanwhile, the superior 97.62% accuracy was reported then testing was performed using the images acquired by a single operator. It has been proved that the feature extraction based on the analysis of spatial frequencies is strongly dependent on the image acquisition conditions, and it is problematic to achieve reliable and reproducible feature set for the echogenicity estimation via spatial frequency analysis.

Chen performed localized analysis and extracted suspicious echogenic segments (Chen et al., 2012) in the midbrain region. Scale invariant blob detector combined with the watershed segmentation was applied for the extraction. Scale-space representation was obtained applying the difference of Gaussians (DoG) operator. DoG function in 2D could be expressed as:

$$D_{\sigma,s\sigma}(x,y) = \left[ \frac{1}{2\pi\sigma^2} \exp\left[-\frac{(x^2+y^2)}{2\sigma^2}\right] - \frac{1}{2\pi s^2\sigma^2} \exp\left[-\frac{(x^2+y^2)}{2s\sigma^2}\right] \right], \quad (16)$$

where  $\sigma$  is the standard deviation of Gaussian;  $s$  is the scale coefficient. The blobs having a relatively stable centre over the scales are assumed as marking echogenic regions. Blobs outside the ROI are removed, and the watershed segmentation of hyperechogenic regions is initialized in the next stage. Figure 1.18 presents the results of the algorithm. Ellipse approximation of the manually extracted half of the midbrain served as ROI (see Fig. 1.18 (A)).

Nine local features (area and entropy of the extracted regions, area and entropy of blobs in the ROI, parameters of Weibull distribution approximation of the histogram of the regions etc.) were used for the PD recognition (Chen et al., 2012). The classification ratio was compared with the results obtained using global features proposed by Chen et al. (2010) and texture features (Chen et al., 2011). The 72.46% classification ratio was achieved using the local features; meanwhile, using global features, it was 76.71% and 48.55% when using texture features.

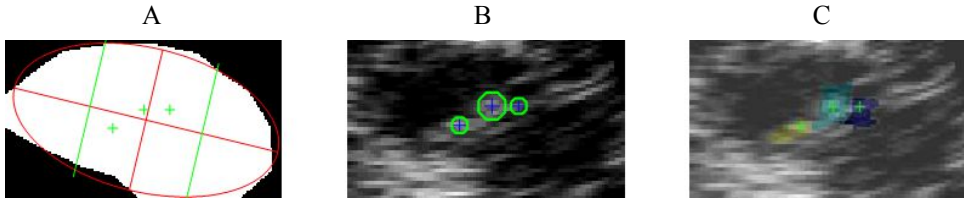


**Fig. 1.18** Scale-space blob detection based segmentation of the echogenic regions: (A) mask used for the ROI extraction (red ellipse), (B) blobs detected in the ROI, (C) regions segmented applying watershed method (adopted from Chen et al., 2012)

The authors applied image normalization in order to compensate the influence of user-predefined scanning settings in the next experiment. It has been found that the extracted local features are less sensitive to the image acquisition circumstances, since the amplitude normalization did not affect the recognition ratio. The experiments were performed using the dataset analysed by Al-Zubaidi et al.

There is a research group working in the Czech Republic (Školoudik et al., 2014; Blahuta et al., 2010). They proposed to use neural networks (Blahuta et al., 2011; Blahuta et al., 2011) and principal component analysis (Blahuta et al., 2010) for the brainstem recognition and semi-automatic evaluation in TCS images. The software for semi-automatic SN evaluation was developed (Školoudik et al., 2014). The SN echogenicity estimate was based on the binary threshold of ROI (ROI – manually placed ellipse surrounding SN). It was proposed to use the novel echogenicity index (EI), the area under the curve which is a relation between the intensity threshold value and the size of thresholded area. The results were found moderately correlated with the manually estimated SN (Spearman  $r$  in the 0.6 – 0.7 range). An example of curves used for EI estimation is presented in Fig. 1.19.

The main approaches for TCS image quantification were discussed in this subsection. There are no reliable and diagnostically acceptable quantitative

parameters supplementing SN area (the best classification ratio achieved for PD/control groups was 81.88%).

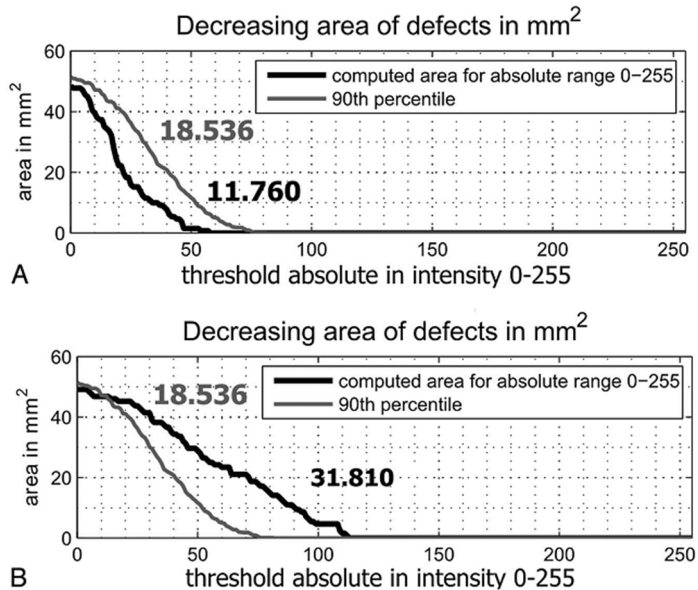


**Fig. 1.19** Curves for echogenicity index estimation (black line): (A) control group (EI=11.76), (B) PD (EI = 31.81) (adopted from Školoudik et al., 2014)

## 1.7. Conclusions of the 1<sup>st</sup> chapter and the tasks of the research

1. TCS is innovative and undoubtedly valuable tool for the assessment of the brain parenchyma. It could be used for screening elderly people, but relatively low specificity (up to 70-75%) limits the ability to apply TCS as a primary test for the diagnostics of neurodegenerative movement disorders, but it is supposed that the early stages of PD could be diagnosed by TCS.

2. The main disadvantage of TCS is poor image quality, and this makes the diagnostics more subjective. The TCS examination is strongly dependent on skills and experience of the scanning and evaluation performing neurosonologist; therefore, the automated tools for image segmentation and analysis are desirable.

3. The survey of the developments in TCS equipment showed that there are some improvements proposed: adaptive focusing, 3D transcranial ultrasonography. Unfortunately, these techniques are in the early development stage, and their applicability in clinical practice is still debatable.

4. There are some solutions proposed for the image segmentation and analysis in case of TCS, but there are no fully automated systems. Furthermore, there are no reliable quantitative image features established for the midbrain echogenicity evaluation.

The summary of findings in the literature turns into the **tasks for the research**: It is necessary (1) to evaluate the spatial resolution of the scanner used for the TCS image acquisition and to determine the potentiality of the transcranial imaging method taking into account the dimensions of the structures of interest in the brain. It is important as well to evaluate the main transcranial B-mode imaging technical (image quality affecting factors) and methodological (planimetry, observer's variability) limitations and their weight. The observer's variability is characteristic for the TCS due to comparatively low image quality. Aiming to reduce the variability, it is mandatory (2) to develop algorithms for the denoising and automated segmentation of the informative regions (the midbrain and substantia nigra) in the diagnostic B-mode TCS images. Furthermore, the automated image processing tools could serve for the training of inexperienced neurologists to outline SOI. The neurosonographic assessment of the brain structures could be automated, and therefore it is necessary (3) to propose a methodology for TCS image based on the quantitative estimation of echogenicity degree in the midbrain region and (4) investigate and evaluate the efficiency of the proposed image processing algorithms using diagnostic TCS images of the subjects having healthy and pathologically altered (hyperechogenic) midbrain.

## **2. THE EXPERIMENTAL INVESTIGATION OF TCS IMAGING LIMITATIONS**

Regarding the earlier studies discussed in chapter 1, it has been determined that the TCS scanning suffers from a certain technical and methodological limitations. The spatial resolution of the TCS images is much lower in comparison to the B-scan images obtained by scanning soft tissue, and only an experienced physician is capable to identify and interpret the brain structures appropriately. Furthermore, the single plane assessment is used for evaluation. Unfortunately, PD diagnostics using TCS is still very subjective and competence-dependent. There is no commercial ultrasonic scanner or even scanning preset focused on the transcranial applications so far. This chapter presents the results of experimental investigation made with the aim to familiarize with the main TCS imaging limitations and evaluate the characteristics, particularly spatial resolution, of equipment (ultrasonic scanner GE Voluson 730 Expert) used for the TCS data collection in the further study.

### **2.1. Evaluation of the spatial resolution of ultrasound scanner Voluson 730 Expert**

The system spatial resolution is defined as the ability to visualize and distinguish small objects. Low spatial resolution results in the blurred and enlarged edges of regions in images, thus directly affecting the accuracy of the measurements. It has been reported that the acoustic beam spread in about 2 mm results in 1 mm difference in length measurement (Hoskins et al., 2010). Furthermore, the acoustic properties of the temporal bone limit the repeatability of neurosonographic approach. The absorption of acoustic energy and phase aberrations are variable from case to case, and the evaluation of a relatively small SN region (SN area in the control group are within 0.05-0.15 cm<sup>2</sup>) is affected noticeably. The authors evaluated the spatial resolution of the equipment used with the aim to obtain intuition about the order of possible estimation errors and estimate how the presence of temporal bone in an acoustic path affects the resolution of images.

The experimental *in vitro* investigation of ultrasound system Voluson 730 Expert (General Electrics Healthcare, Austria) used for the transcranial imaging at LUHS Clinics of Neurology was performed. The scanner was equipped with a multifrequency PA2–5 phased array sector probe (footprint 20 × 14 mm, 128 acoustic elements). The experience obtained in clinical practise caused the selection of the scanning frequency range of a probe. Only the lower frequencies (1.4-4 MHz, fundamental frequency - 2.5 MHz) are suitable for the imaging of the brain structures. The main characteristics of the scanner used in the experiments disclosed by the manufacturer are as follows: selectable transmit focal depth (1 or 2 depths possible), digital multi-depth sub-pixel dynamic receive focusing (accuracy of focus ± 3 ns) is applied together with a receive apodization, TGC curve: 100 dB control range, possible to adjust in 8 depths by sliders, gain up to 30 dB, sample rate 60 MHz. The experiments presented in this chapter were performed preserving the scanning settings (parameters) close to the presets used in the routine clinical TCS

examination. The transmit focus is typically adjusted for the single depth: 8 cm or 11 cm subject to the SOI location. The gain and TGC are adjusted by scanning performing operator for the best performance subjectively. TGC was typically adjusted by increasing the amplification at the ROI depth. The digital TCS images were stored in the raster graphics 8BIT (256 gray values) bitmap image file format (BMP). The image is constructed applying the logarithmic compression of the RF signal envelope. The non-linear slightly convexed (suppressing lower amplitude echos) gray map curve was applied for the conversion from the ADC to the gray scale units (the B-scan formation procedures are briefly introduced in 1.3 subsection).

A phantom manufactured for the spatial resolution evaluation (Jurkonis et al., 2009) and the temporal bone sample (LUHS, Department of Anatomy) were used. The experimental setup is presented in Fig. 2.1 (B). The phantom was made of fishing line stretched on the screw threads at the equal distances ( $L = 3$  mm, see Fig. 2.1 (A)). The diameter of the line was  $d = 0.1$  mm. The cross-sectional B-mode images of fishing lines were used for the estimation of resolution at various depths assuming the fishing line as a point reflector. The sketch illustrating phantoms cross-section is presented in Fig. 2.1 (C). The probe transmitting focal depth was set to 8 cm taking into account the location of the structures, which are under evaluation during the transcranial scanning. The midbrain cross-section is normally situated at the depths from 6 up to 9 cm.

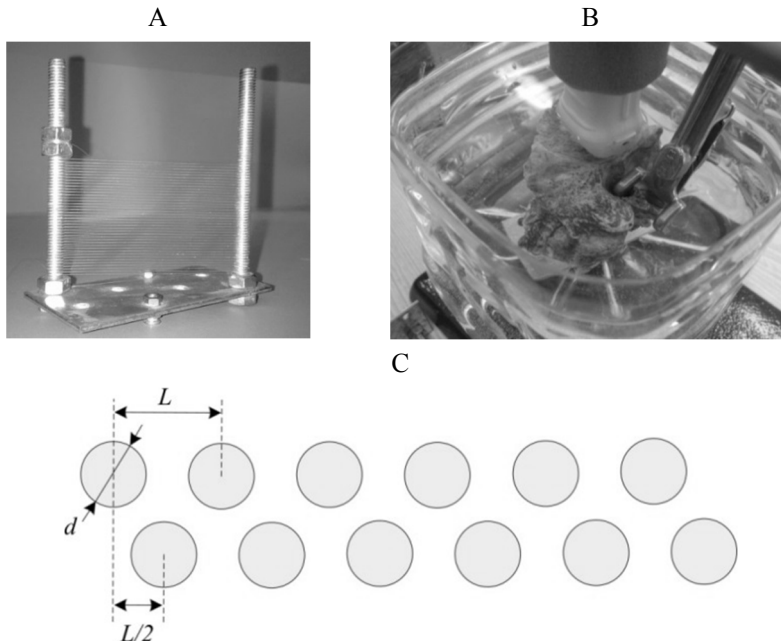


**Fig. 2.1** Spatial resolution estimation of Voluson730 Expert US system: (A) a fishing line based phantom, (B) the experimental setup, (C) a sketch of axial cross-section of the phantom (rotated horizontally)

The phantom was immersed into a degassed water tank. The investigation was performed in two stages. Firstly, only the phantom was scanned, and in the second stage, the temporal bone was inserted between the probe and the phantom in order to estimate the influence of the bone. The probe and the phantom were maintained in a fixed position. Figure 2.2 presents few images obtained during the investigation. Fig. 2.2 (A) picture represents an image obtained by scanning the phantom solely. Point targets are clearly visible and separable in the obtained B-scan image (isotropic pixel spacing 0.421 mm). Fig. 2.2 (B) shows an image obtained by scanning through the skull bone layer. Only the point reflectors, which are close to the focal spot, are identifiable and distinguishable. In order to improve the contrast of the image, the amplification of received echo-signals was applied. Fig. 2.2 (C) presents the image obtained applying 30 dB gain. The obtained image is even fuzzier, because the amplitude of echo-signals was relatively low, and the amplification increased the noise level.

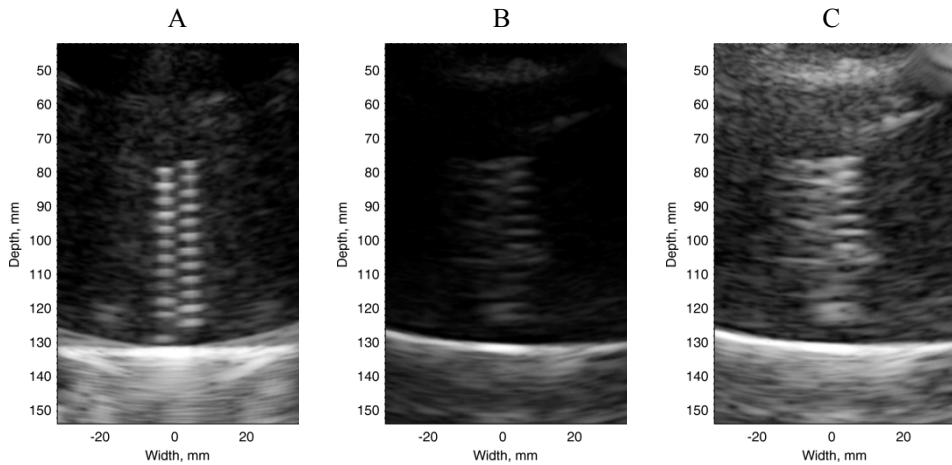


**Fig. 2.2** B-scan images of the phantom: (A) image before the insertion of bone (scanner gain setting: -15 dB), (B) image acquired after the insertion of temporal bone (scanner gain setting: -15 dB), (C) image acquired after the insertion of temporal bone after the amplification (scanner gain setting: 15 dB)

The spatial resolution was evaluated at full width at half maximum height (FWHM) of the point spread function (PSF). Fig. 2.3 presents the comparison of the PSFs before and after the insertion of the bone: (B) presents PSF obtained by scanning the phantom solely and (D) the case when the phantom was scanned through the bone (the image segments used for the evaluation are presented in (A) and (C)).

The investigation showed that the axial resolution did not suffer significantly (in both cases, the axial resolution was approximately 1.4 mm); meanwhile, the changes in lateral spread were considerable (lateral resolution before the insertion of the bone  $\sim 3.1$  mm, after it exceeded 5 mm). As it was mentioned before, only the point targets close to the focal zone are clearly identifiable; thus, it was impossible to estimate the spatial resolution in various scanning depths after the insertion of bone. A noticeable spatial resolution degradation was found by scanning deeper, and

the evaluation of both SN regions in the symmetric midbrain, in the unilaterally acquired plane, would be ambiguous. The estimated absolute resolution values of US images are noticeably lower to compare with the results presented by Walter and colleagues (Walter et al., 2008), even without the influence of temporal bone. It could be predicted that these differences arises due to the specific properties of the arrays and array controlling algorithms and the operations applied in the image formation chain.

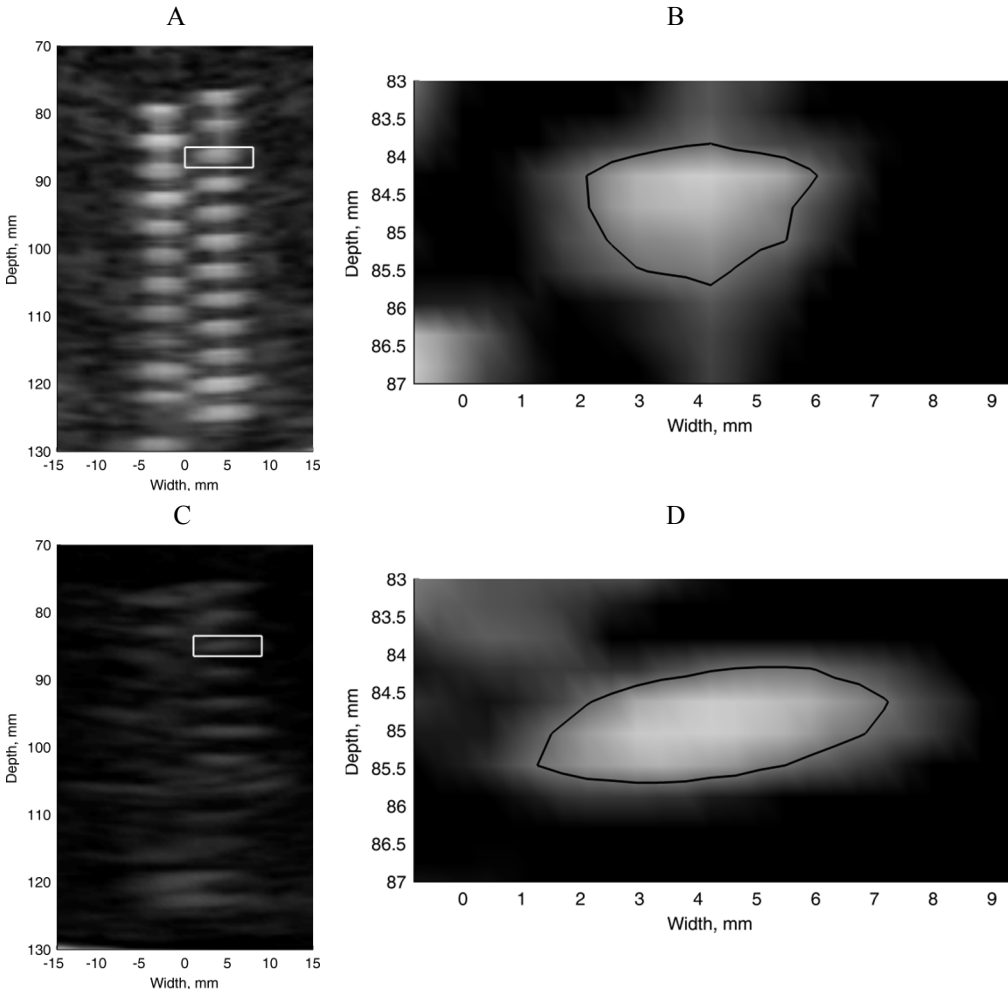


**Fig. 2.3** Investigation on how the temporal bone influences the spatial resolution: (A) a cropped B-scan image of the phantom, (B) PSF selected at focal depth with an outlined contour at -6 dB level (marked by rectangle in Fig. A), (C) a cropped B-scan image of a phantom performing an experiment after the temporal bone insertion, (D) PSF after the bone insertion selected at a focal depth together with an outlined contour at -6 dB level (marked by rectangle in Fig. C)

Unfortunately, such important properties like dimensions of acoustic elements, number of active transmit/receive elements, digital signal/image processing algorithms are not disclosed by the manufacturers.

The relatively low sampling period (size of the pixel is 0.5 mm) should be remarked. Such size of the pixel results in the theoretical limit of the resolution. Even if the point would be represented by a minimum of 3 pixels (low level/high level/low level), the resolution of 0.5 mm would be achieved. The fundamental limit of axial resolution related to the ultrasonic scanning frequency is 0.62 mm determined by the ratio  $c/2B$  (where  $c = 1540$  m/s and bandwidth  $B = 2.5$  MHz). The evaluation of the theoretical lateral resolution requires knowledge about the scanning (width of active aperture) and used focusing algorithms, which are not disclosed in detail by the manufacturer. It is possible to scan the acoustic pressure field of the probe, but even having such knowledge, it is not allowed to control (optimize) the scanning algorithm; therefore, this study is limited to the experimental assessment of the spatial resolution by analysing B-scan images. The modification of the equipment (scanner) related to the possible increment of acoustic exposure magnitude requires the recertification of medical device and reassessment of the permission from bioethics committee.

The acoustic properties (attenuation) of temporal bone used in experiments *in vitro* were determined by performing the ultrasonic scanning of the bone. Two single element ultrasonic transducers were used in the experiments. The transducers were matched coaxially; the distance between them was  $L = 6$  cm (both receiving and transmitting transducers spherically focused at 3 cm). Transmitter's bandwidth is 1-6 MHz, fundamental frequency 3 MHz. Wide-band (1-17 MHz) probe was used as a receiver (both Karl-Deutsch, Germany). The piezo-crystal was excited with 60 V rectangular pulse. The transducers were immersed into a tank filled with degassed water. The experimental setup is presented in Fig. 2.4 (A). The experiment was performed in two stages at room temperature. Firstly, the ultrasound pulse was transmitted through the water solely. SoS (1480 m/s) in water is close to the velocity in soft tissue; meanwhile, the attenuation coefficient is significantly lower, and the ultrasonic signals transmitted through the water could be used as a reference for the frequency dependent attenuation estimation assuming it as negligible.

Secondly, the temporal bone was inserted at the focal depth between the transducers (see Fig. 2.4 (A)). None special preparation of the bone was performed. The dry temporal bone specimen was immersed into the water. The picture of temporal bone used in the experiments is presented in Fig. 2.4 (B). A Fourier analysis of acquired ultrasonic signals was performed. Firstly, the transmitted pulses were gated applying the Hamming window. The attenuation and frequency relationship was determined by comparing magnitudes of spectra of signals transmitted through the water and temporal bone (Fig. 2.4 (D)). A comparison of normalized spectra is presented in Fig. 2.4 (C). The attenuation coefficient was estimated by the following equation:

$$\alpha(f) = -\frac{20}{l} \cdot \lg\left(\frac{A_{norm}(f)}{A_{norm0}(f)}\right), \quad (17)$$

where  $A_{norm}$  is the Fourier spectrum of pulse transmitted through the bone;  $A_{norm0}$  is the reference Fourier spectrum of pulse transmitted through the water (both normalized by the maximal value of  $A_0$  spectrum);  $l$  is the thickness of the temporal skull bone layer;  $f$  is the scanning frequency (Jurkonis et al., 2007).

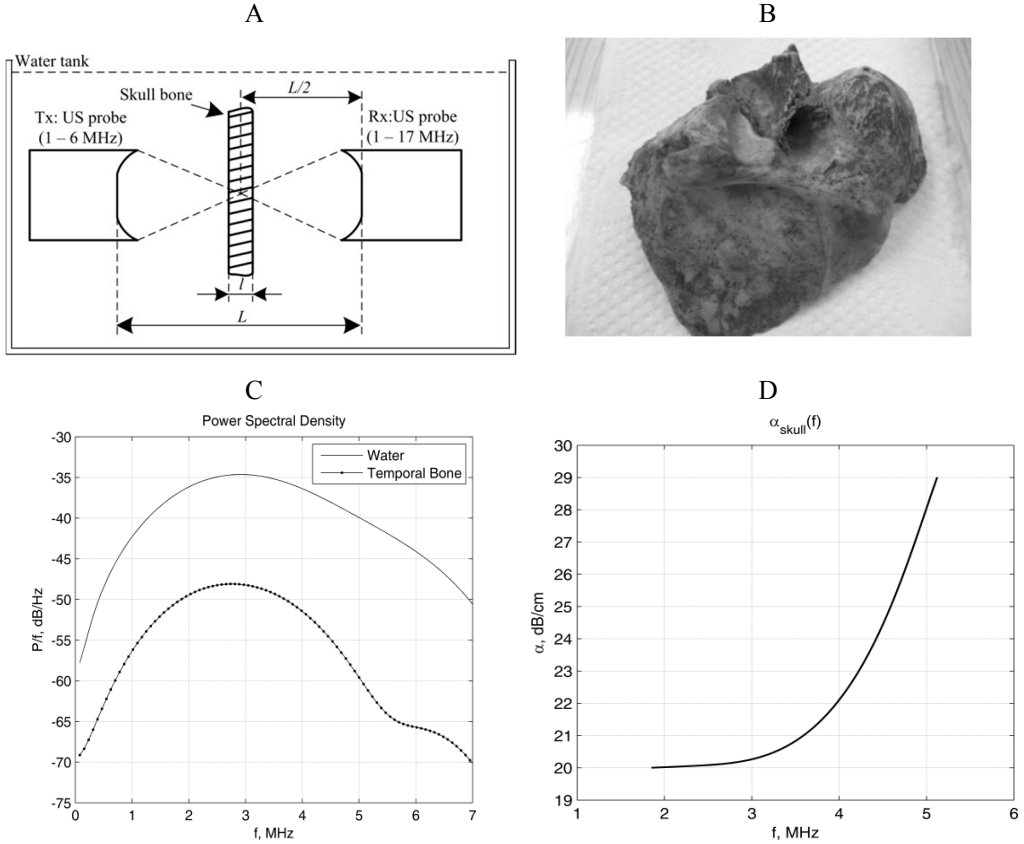


**Fig. 2.4** Investigation of the temporal bone *in vitro*: (A) experimental set-up, (B) the temporal bone used in experiments, (C) a comparison of normalized amplitude spectra of US pulses transmitted through water (solid line) and temporal bone layer (pointed line), (D) the relationship between the US frequency and attenuation in the temporal bone layer

$SoS$  in the bone ( $c_s = 3137.3$  m/s) was as well determined by using A-scan signals acquired in a reflection mode. The thickness of the bone  $l = 7$  mm was measured by a calliper and used for the  $SoS$  estimation. The comparison of normalized amplitude spectra of US pulses transmitted through the water and temporal bone showed that 85% of energy was lost in the skull bone layer. Moreover, the spectral peak was shifted to low frequencies by 0.15 MHz. The determined attenuation of order 10 dB/cm/MHz and  $SoS$  were slightly higher to compare with the values provided by

the other authors (see subsection 1.4). This could be explained by the fact that the dry temporal bone without any preparation was used in these experiments.

The spatial resolution evaluation experiments were revisited using the certified phantom manufactured for the evaluation of ultrasonic imaging systems (model 549, ATS Laboratories, USA). In this case, the experiment was performed without an insertion of the bone, because the point reflectors are even unidentifiable in the obtained images when the bone is present. The front panel of the phantom is presented in Fig. 2.5 (A). The base of a phantom is urethane rubber (attenuation coefficient is 0.501 dB/cm/MHz measured at 3.5 MHz, SoS = 1453 m/s).

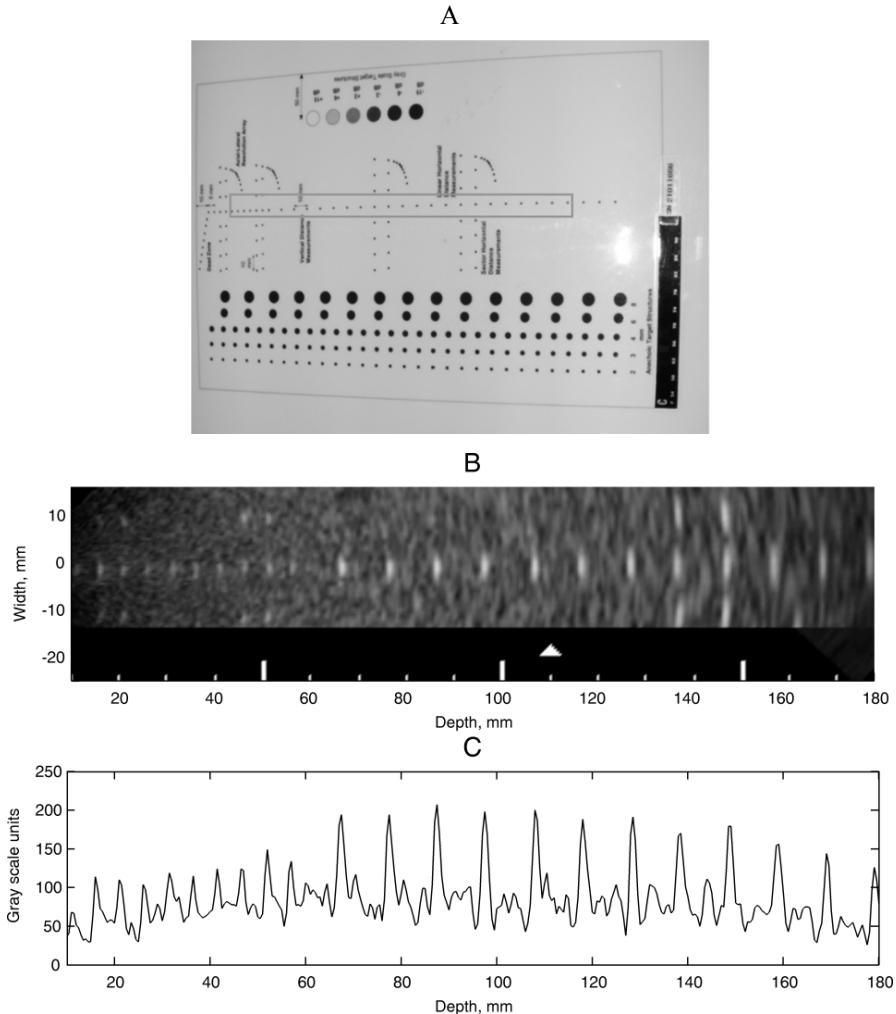


**Fig. 2.5** Spatial resolution evaluation using the certified ATS tissue mimicking phantom: (A) front panel of a phantom, (B) B-scan image of the point targets (scanned target group marked with a rectangle in (A), transmit focal depth marked by triangle), (C) single axial line of the B-scan image with a clearly seen point targets

The nylon threads of small diameter are mounted in the base material and serves as a point target reflectors. The diameter of the fibers is 0.05 mm; the distance between point targets is 0.5 cm (first 7 targets), 1 cm (last 11). The phantom was scanned maintaining the settings of the machine as it was set in the first experiment (except for the transmit focal depth that was moved to 11 cm). The acquired B-scan of the point target reflectors is presented in Fig. 2.5 (B), and the single line of the phantom image crossing point targets is axially provided in (C). Analysing Fig. 2.5 (B) and (C), it could be observed that it is almost impossible to identify the influence of transmitting focal spot (11 cm), this could be explained by the fact that the dynamic focusing, resulting in the pronged focal zone (seen in a depth range 7-16 cm), is used while the probe is working in a receiving mode. The axial and lateral resolution was estimated at FWHM of PSF's at various scanning depths. The results are presented in Table 2.1.

**Table 2.1** Spatial resolution of the scanner used for the TCS examination at various scanning depths

Scanning depth, mm	Axial resolution, mm	Lateral resolution, mm
57	1.82	3.07
67	1.85	3.10
77	1.97	3.74
87	1.72	3.85
97	1.90	4.42
107	1.54	4.55
117	1.84	5.23
127	1.72	6.26
137	2.00	6.10
147	2.19	7.68
157	2.22	8.73

It was determined that the changes in the axial resolution are only marginal (range 1.54 – 2.22 mm) increasing the penetration depth; meanwhile, the lateral resolution degrades drastically (range 4.07 – 8.73 mm). The experimental results coincided with the findings obtained by performing scanning of fishing line based phantom.

The estimated axial and lateral resolution values explain one of the causes of limited repeatability in the TCS assessment. It is known that the typical size of the main indicator SN area is in the range of 0.05 – 0.6 cm<sup>2</sup>. The typical dimensions of SN are 7 × 3 mm. These dimensions are comparable to the evaluated spatial resolution (1.5 × 4.36 mm) of the system used for the transcranial imaging. The area of PSF at FWHM (~ 0.05 cm<sup>2</sup>) is of the same order as the standard sizes of the SN and comparatively huge estimation errors should be expected. The simple coarse simulation was performed with the aim to familiarize with the order of errors which could be expected during the transcranial assessment. The digital images obtained by the certain imaging system could be defined via the convolution of the ideal object to be imaged and the PSF of the system. The PSF of the ultrasonic system was obtained in the experiments. The main biomarker SN is a stripe-shaped structure; therefore, the ellipse was selected as a model shape of SN. The digital

image of the ellipse having dimensions close to SN was synthesized. The binary input image was generated, where low level (0) represents the background and high level (1) the ellipse restricted SN. The relative ellipse orientation was determined by analysing the real TCS images evaluated by the expert. It was determined that the angle between the SN major axis and face of the scanning probe is close to  $45^\circ$ . The assumed ideal image with SN ellipse-shaped structure was convolved with the anisotropic 2D Gaussian function having the spread close to the evaluated spatial resolution of the system in the axial ( $\delta_{ax} = 1.4$  mm) and lateral directions ( $\delta_{lat} = 4.2$  mm) at the FWHM. The spatial resolution values were selected with respect to the brain structures, which are under evaluation in TCS experiments. The 2D Gaussian function supposed as PSF is expressed as:

$$f_{PSF}(x,y) = \frac{1}{2 \cdot \pi \cdot \sigma_x \cdot \sigma_y} \exp \left[ - \left( \frac{(x - \mu_x)^2}{2 \cdot \sigma_x^2} + \frac{(y - \mu_y)^2}{2 \cdot \sigma_y^2} \right) \right], \quad (18)$$

where  $\sigma_x, \sigma_y$  is the standard deviation (spread of the blob) in the axial and lateral directions, respectively;  $\mu_x, \mu_y$  is the centre (mean) coordinates of the blob. Figure 2.6 presents the results of the experiment. Fig. 2.6 (A) shows an example of the image of the ellipse-shape structure (size  $0.20 \text{ cm}^2$ ) after the convolution with  $f_{PSF}(x, y)$  and the established boundary contours at FWHM in the “ideal” and blurred images. Fig 2.6 (B) presents the relationship between the relative SN size estimation errors and the size of ideal ellipse shaped SN. The size of the ellipse was modified varying scale, thus keeping the relative dimensions the same.

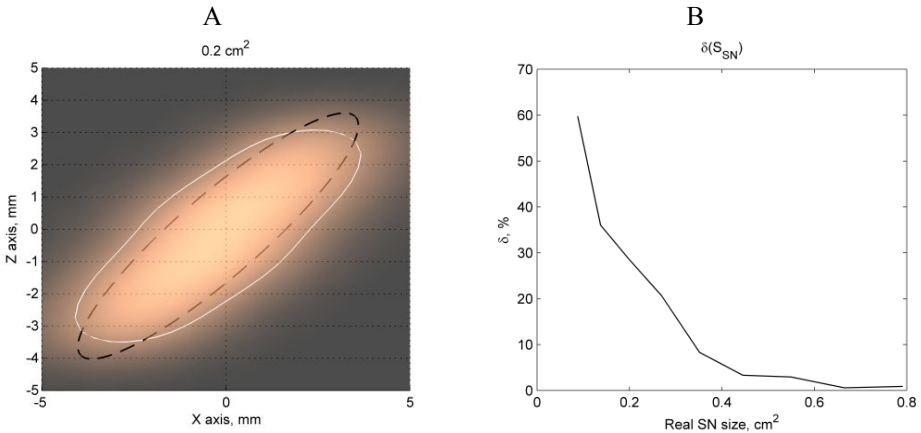


**Fig. 2.6** The results illustrating the approximate order of SN estimation errors: (A) an example of ellipse shaped object having dimensions close to the typical SN area in the TCS images (size –  $0.2 \text{ cm}^2$ ) together with the contour lines at FWHM level determined before (ideal, black dashed line) and after the convolution (blurred, white solid line) with anisotropic Gaussian function, (B) the relationship between the real size of ellipse shaped object and relative size estimation error, which could be expected if the spatial resolution of the system is  $\delta_{ax} = 1.4$  mm,  $\delta_{lat} = 4.2$  mm

The relative errors up to 60% could be expected for the sizes of SN which are typically (the SN size varies in the range of 0.05 – 0.6 cm<sup>2</sup>) evaluated during the clinical examination. It should be mentioned that such evaluation is relatively rough, since the model of the SN was simplified, and the noise component was assumed as negligible. However, it should be noticed that the dimensions of PSF were estimated without the insertion of the temporal bone sample; therefore, even more significant errors are possible. These findings demonstrate that the SN size measured by TCS rather have to be called ultrasonic size that corresponds to the real size of the measured object. TCS assessment is very close to the possible/impossible limit.

## **2.2. Investigation of the TCS intra-observers variability**

It is known that the intra-observer and inter-observer variability is noticeable in the manual sonographic evaluations. A study was performed in order to evaluate the test-retest reliability of one expert in the case of TCS. The SN area was manually outlined in 40 TCS images three times in one month period (approximately one week between the evaluations) by the same sonographer. Fleiss kappa  $\kappa$  (Fleiss, 1971) was calculated in order to evaluate the reliability of an expert (test-retest reliability). Interpretation of  $\kappa$  values could be defined as:

- $\kappa < 0$  - no agreement,
- 0-0.2 slight agreement,
- 0.21-0.4 fair agreement,
- 0.41-0.6 moderate agreement,
- 0.61-0.80 substantial agreement,
- 0.81-1 near perfect agreement.

Moreover, the spatial overlap of the outlined areas and Hausdorff distance (HD) between the outlined SN contours was evaluated. The detailed explanation of the metrics used for the expert evaluation reliability estimation and the results obtained comparing two raters are presented and discussed in chapter 4. The video material (sequence of TCS frames acquired during scanning) was reviewed by an expert before outlining the images for the second time. This influenced the results, and the variations appeared in certain conditions even in the evaluations of the same sonographer. Table 2.2 presents the results. A better agreement ( $\kappa = 0.85$ ) was obtained when marking the images off-line without the review of the video material. This shows that even the conditions can influence the result. Test-retest reliability of one expert (averaged overlap  $56.19 \pm 11.99\%$ ,  $\kappa = 0.485$ ) showed considerable variability of the expert evaluations. It could be concluded that the TCS is strongly dependent on the experience of the sonographer. The obtained results indicate that the automated image processing and segmentation tools are necessary for the assistance. The automated segmentation of SOI in TCS images could reduce the variability of the inter- and intra-observer, but there is no validated efficient technique for the segmentation of the brain structures in TCS images, which are of special interest in the clinical diagnostics of PD.

**Table 2.2** Expert evaluation reliability

No.	$\kappa$	$HD_{SN}$ Mean $\pm$ SD [mm]	$O_{SN}$ Mean $\pm$ SD [%]
1 - 2	0.43	2.83 $\pm$ 1.54	50.22 $\pm$ 17.55
1 - 3	0.85	2.32 $\pm$ 0.79	56.19 $\pm$ 11.99
2 - 3	0.31	2.43 $\pm$ 1.23	51.69 $\pm$ 16.09
1 - 2 - 3	0.49		

No. is the numbers of markings (times), which were compared,  $HD_{SN}$  = averaged Hausdorff distance between the contours of SN area,  $O_{SN}$  = averaged region overlap between the SN areas, SD = standard deviation.

### 2.3. Limitations due to the planimetry in TCS

Planimetry is a certain methodological limitation of TCS. Conventionally, the maximal evaluated SN area from a two bilateral scanning planes serves as a biomarker. Single-plane (which is selected by scanning performing physician) estimation limits the precision of the TCS, since it is not easy to reproduce the same scanning plane for the repetitive evaluation. Respectively, it is difficult to ensure that the maximal SN cross-sectional area is acquired. In order to demonstrate the ambiguity of TCS assessment, the cross-sectional midbrain scans obtained by the TCS and MRI were investigated. The sizes of SN area increases in the case of PD, and it is difficult to extract SN region in MRI scans. Therefore, a midbrain region was selected in order to demonstrate the existing variability within the neurosonographic estimations. The midbrain area was outlined manually in 1141 TCS scanning planes acquired during 2010 – 2014 period at LUHS Clinics of Neurology by the experienced neurosonologist. The average midbrain area (5.19 cm<sup>2</sup>) and its standard deviation (0.84 cm<sup>2</sup>) was estimated, the minimum measured area was 3.01 cm<sup>2</sup>, meanwhile, the maximum was 8.18 cm<sup>2</sup>. Fig. 2.7 (A) presents a histogram of the midbrain sizes evaluated by the TCS. The dataset containing head MRI images of 10 subjects were as well investigated. Each dataset consisted of 176 two-dimensional planes (image size 512  $\times$  512), isotropic pixel spacing 1 mm, the distance between the cross-sections 1 mm, data collected using TW1 mode. All the subjects were examined at the clinics of radiology at LUHS. The aim of this study was to evaluate the midbrain area at different MRI scanning planes moving through the brainstem and render a 3D image of the midbrain for the qualitative evaluation of 3D shape and uniformity in a craniocaudal direction. The midbrain area was manually segmented in 10 MRI two-dimensional planes in each dataset. The reference plane was MRI scan, which is closest to the back of a head, and it is still possible to identify and delineate the midbrain region, and 9 planes in a craniocaudal direction were selected. It was assumed that the brainstem is orthogonal to the cross-section planes in all the scans. The 3D surface images of the head and the segmented midbrain volume were reconstructed. The 3D model of head together with the midbrain is presented in Fig. 2.7 (B). The midbrain 3D surface image is presented in Fig. 2.7 (C). The 3D surface images were reconstructed applying the marching cubes algorithm (Lorenson et al., 1987) and visualized using MeshLab v. 1.3.1 free software (Visual Computing Lab–ISTI, Italia). It is clearly seen that the area of the

midbrain varies with the level of a brainstem (see Fig. 2.7 (C)  $z$  axis direction). The obtained averaged midbrain area in all 100 planes was  $6.07 \pm 0.78 \text{ cm}^2$ . The relationship between the mean midbrain area and relative level of the brainstem in a craniocaudal direction is presented in Fig. 2.7 (D). The measured deviation in case of TCS and MRI and distribution of the areas shows certain limitations of TCS methodology; the scanning planes used for the evaluation are hardly comparable between the cases. This makes the examination slightly subjective and competence-dependent. This error source could be eliminated or alleviated by the volumetric approach or multiplanar assessment of the brain structures. One of the possible options proposed by Huang et al. (2007) is to evaluate the size of the SN area relative to the size of the whole midbrain, but the anatomical shape and variability of SN volume of healthy and subjects with PD is still unexplored enough. It has been recently proposed to use few scanning planes for the SN assessment (Sanzaro E., et al., 2014). The authors used integral SN load estimate taking into account the SN evaluated bilaterally in two different levels of the brainstem (in total 4 planes).

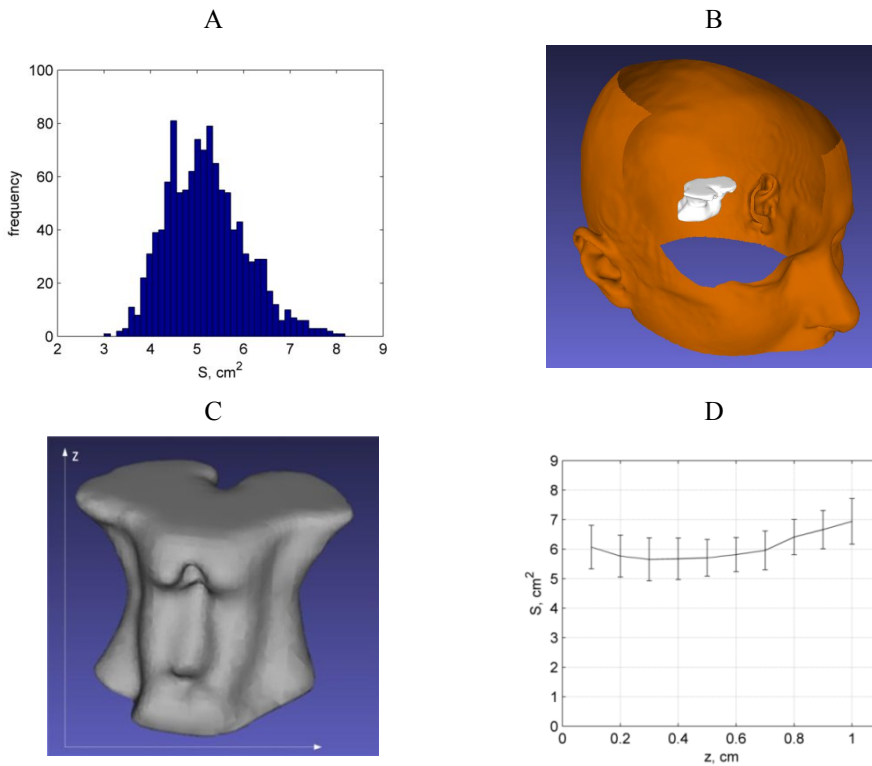


**Fig. 2.7** Results of MRI and TCS midbrain area measurements: (A) the distribution of midbrain areas evaluated by TCS, (B) 3D surface image of head and midbrain reconstructed from the MRI planes, (C) 3D surface image of the midbrain, (D) the relationship between the mean midbrain area and the level of the brainstem in a craniocaudal direction (the results of standard deviation are as well presented)

It has been demonstrated that the SN load significantly correlates with the stage (according to Hoehn and Yahr) of the disease. It was as well proposed (Canovas A.A., et al., 2014) to select the maximal SN area from three repetitive estimations as the main biomarker or to extend scanning into 3D and to evaluate SN volume (Plate et al., 2012) in order to increase the objectivity of the examination. The standardized scanning plane assessment or volumetric (3D TCS) approach could eliminate or at least mitigate these uncertainties. However, the size of the midbrain area carries supplementary information about the relative SN location respective to the brainstem level.

#### **2.4. Conclusions of the 2<sup>nd</sup> chapter**

1. The evaluation of spatial resolution of the ultrasound system used for the transcranial imaging demonstrated that the axial resolution did not suffer significantly due to the presence of the temporal bone; meanwhile, the changes of lateral spread were considerable (the resolution was lower than 30% at focal spot). The dimensions of the main biomarker SN are comparable to the evaluated spread, and the huge measurement errors could be expected (relative error up to 60%), thus confirming the statement that TCS is on the limit of the system capabilities.
2. The evaluated test-retest reliability of one expert showed considerable variability in the estimations made by single neurosonographer.
3. The investigation of the midbrain area distribution evaluated by the TCS and MRI showed a certain limitation of TCS methodology. The selection of the scanning plane for SN area assessment is subjective and competence-dependent, thus limiting the repeatability and accuracy of sonographic approach. The standardized scanning plane assessment or volumetric (3D TCS) approach from multiple planes could eliminate or at least mitigate these uncertainties.
4. The experimental investigation of TCS imaging limitations shows the existence of the subjective component in the neurosonographic assessment. The automated image segmentation and echogenicity estimation algorithms are desirable and could reduce intra- and inter-observer variability and ensure the repeatability of the sonographic approach.

### 3. THE PROPOSED TCS IMAGE PROCESSING SYSTEM

The analysis of literature and experimental investigation of TCS imaging limitations revealed the demand of image processing algorithms for the extraction of SOI and quantitative assessment of the echogenicity degree in the midbrain region. The images are quite confusing for the manual diagnostic evaluation, and the automated approaches could ensure the repeatability, reduce the variability of TCS evaluations, thus increasing the reliability of PD diagnostics. This chapter presents the concept of the proposed image processing system and its main components in the subsections: (1) algorithm for noise suppression in the TCS images (3.1. subsection), segmentation of SOI: mesencephalon (3.2. subsection) and intra-mesencephalic brain structures, particularly SN (3.3. subsection) and quantitative features used for the echogenicity evaluation of the extracted informative regions (3.4.) in the images. The scheme of the proposed image processing system is presented in Figure 3.1. The main components of the system are as follows:

1. The denoising algorithm based on the principle of the spatial compounding of the multiple scanning planes decorrelated in the sense of noise. The eligible images for averaging were extracted from the TCS image sequences acquired during the routine clinical exam. The eligibility criteria were established, and the method for frame-to-frame displacement estimation was proposed.
2. Novel, fast method developed for the semi-automated segmentation of the midbrain region (ROI). The combination of an experience-based statistical shape model (SSM) and amplitude invariant local phase congruence based edge detector was proposed for the statistical shape fitting.
3. SN extraction algorithm, a classifier based approach, was developed. It was assumed that the half of extracted symmetric midbrain region ( $\frac{1}{2}$  ROI) contains pixels belonging to the (1) SN class or (2) the class of surrounding tissue. The classifier was trained using the local variance of pixel intensities and distances from the reference points based on the typical anatomical relative midbrain/SN pose prior (in total 8 features).
4. The algorithm for the extraction of reduced intra-mesencephalic region (RROI) which covers SN region for further quantitative analysis. The method is based on the assumption that mainly two regions of different echogenicity are found in the  $\frac{1}{2}$  ROI in TCS image. The purpose of this research was to extract a region under a closed curve satisfying the inter-class variance criterion proposed by Otsu.
5. Echogenicity assessment. Various parameters proposed for the evaluation of echogenicity in automatically extracted segments ( $\frac{1}{2}$  ROI, SN and RROI) are presented in subsection 3.4.
6. Mahalanobis distance based classifier was used for the PD recognition. The optimal subset of potential quantitative features (extracted by means of image analysis) was determined and used for the classification. Moreover,

the data collected in clinical examinations (results of the manual ultrasonic evaluation of brain structures) were involved in the analysis.

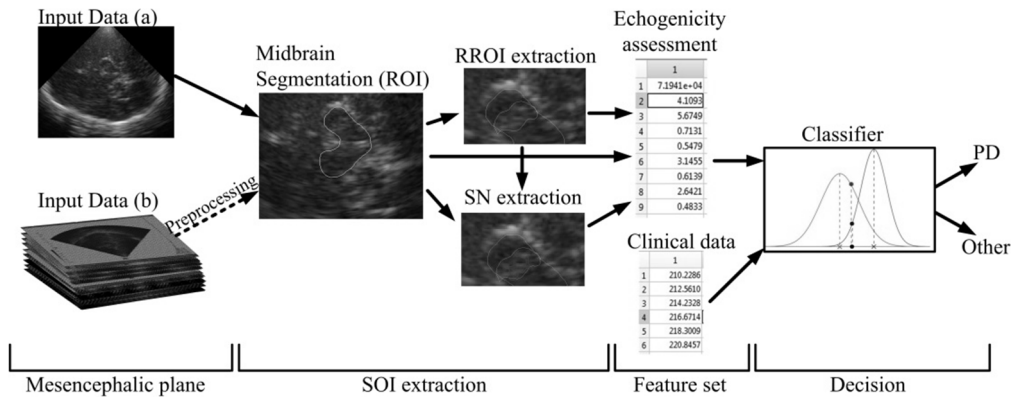


**Fig. 3.1** Scheme of developed TCS image processing system

**Experimental data.** This dissertation was prepared by analysing the data collected by the LUHS Department of Neurology during 2011 – 2014. The study was approved (05-11-2010, permission No. BE-2-70) by the Regional Ethical Committee of Biomedical Studies (Kaunas, Lithuania) ensuring accordance with the guidelines of the Helsinki Declaration. Every adult subject provided a written agreement and permission to participate in the study and use the obtained images confidentially. All the scans were performed on-line by Kristina Laučkaitė who is a neurologist trained in vascular and transcranial ultrasound and has an international certificate in TCS application in Movement Disorders.

The collected dataset consisted of a TCS image database (from 2 up to 30 images/per case, the number of the images directly depends on the quality of the acoustic window) and TCS image video sequences (collected not in all the examined cases), the database of accompanying clinical data (demographic data, the results of the manual TCS evaluation, the results of clinimetric scales etc.) of each subject (the main attributes of the database are presented in Table 4.5). Moreover, the manual annotations made by experts (40 images evaluated by two experts and 90 by more experienced expert Kristina Laučkaitė) were obtained.

All the B-scan images analysed in this study were gathered and stored in BMP format. Possible to control scanning parameters (gain, TGC, transmit focal depth) were adjusted by the scanning performing operator. The subjective tunnning criterion was the most clearly seen SOI as possible. The explicit description of the equipment used for data acquisition and the main B-scan image formation stages are presented in the subsections 1.3 and 2.1. The video sequences were stored in Audio Video Interleaved (AVI) format. Video memory size  $800 \times 600 \times 32$  BIT.

In total, 341 cases from the examined 704 cases were assigned as appropriate for the further analysis after careful preselection (the preselection criteria are motivated in 4.4. subsection). Two input data types were analysed: (a) single plane TCS images and (b) video sequences collected during the routine examination of the

brain. The image denoising algorithm based on the multiplanar data processing was developed, but only a limited number of cases having appropriate sequences of the images were gathered. Respectively, it is presented as an option in the proposed image processing chain. The denoising efficiency was demonstrated by significant SNR and CNR improvement. Meanwhile, other algorithms for SOI segmentation and echogenicity analysis were developed by working with 2D static TCS images.

### **3.1. Multiplanar suppression of noise in TCS images**

There are two sources of noise in ultrasonic imaging: acoustic and electronic (see 1.4. subsection). A suppression of the speckle noise is a priority task concerning the denoising of the ultrasonic images. It has been noticed (Boyce, 1992) that if an object is scanned from different spatial positions preserving the same scanning plane and the transducer is translated at about a half of its width, the acoustic noise in different frames in a sequence could be concerned as random, since then, the interference conditions are altered. In such case, the speckle noise in the images becomes uncorrelated and could be suppressed by a simple frame averaging. It should be pointed out that the frame averaging as well reduces the electronic noise, which is random in all the frames. Authors frequently indicate that a multiplicative model of noise free image and speckle noise in the ultrasound images is more adequate, but because of the application of logarithmical transformation during the processing of radio frequency signals, it could be interpreted as additive (Michailovich and Tannenbaum, 2006). Several semi real-time approaches of spatial compounding were introduced by the authors in the recent decade. The multi-planar scans can be achieved by applying specific electronic beam steering algorithms (Entrekin et al., 2001) using a system of the transducer arrays located at different spatial positions (Behar et al., 2003) or tracking the position of the probe with a position sensor (Rohling et al., 1998). However, it should be mentioned that such processing procedures reduce the frame rate; moreover, the supplementary equipment is needed. The modified spatial compounding approach for off-line processing of ultrasonic image sequences acquired during the routine procedure was proposed. The pose of the probe is influenced by the involuntary movements (blood pulse, the slight movements of the patient and hand of the scanning performing physician) and voluntary movements made by a neurosonographer who is searching for most informative planes for the diagnostics during the dynamic TCS exam. These movements cause random instability of the scanning plane. The idea of the pre-processing is to employ these voluntary and involuntary movements of the probe for the acquisition of image sequence, which are uncorrelated in the sense of the speckle noise. Figure 3.2 presents the block scheme of the proposed algorithm applied for the denoising of TCS images.

A randomization of the noise in an image sequence is achieved due to the movements of a probe, but at the same time, the determined structural component is a bit displaced in the frames of a sequence. The brain structures are misplaced, and it was proposed to supplement an averaging algorithm by motion compensation unit (correction of a spatial discrepancy between the frames in a sequence), because

otherwise the ROI structures could be lost during the averaging procedure; moreover, the edges of regions may become blurred. The method for mismatch compensation was proposed. At first, the initial reference image for the displacement estimation was established. Each frame in a sequence was tested in a role of a template. The high reflectivity region (containing structural information) in the potential reference image was compared with the corresponding regions in a whole sequence via normalized correlation coefficient  $r$  (see formula 22). The frame which was found most similar to all the rest in a sequence was used as a reference. The evaluation of relative frame to reference (FtR) displacement of the determined components (brain structures under evaluation) was estimated by using preselected region in an image. The contralateral to the scanning probe skull bone region served for this purpose. The bone has a stable structure, clearly seen in each image of a sequence, and in the most cases, it is the brightest area, due to the large differences of acoustic impedance between the bone and soft tissue (see Fig. 3.3 A). In order to avoid outliers, firstly, all the images were cropped. The cropping dimensions were determined via prior anatomical knowledge about the depth where contralateral skull bone is found (typically, the bone is found in a depth range 14-16 cm). In the second stage, the skull bone was extracted. The images were converted into binary by applying the global threshold, assuming that the amplitude level is approximately constant in a sequence (experimentally established threshold 85% from a maximum amplitude level in the analysed region). The extracted binary region was handled as an ellipse, and the angle between the major axis of the ellipse and x axis was assumed as the orientation of the images in a sequence. The orientation angle is found as (Haralick, Shapiro, 1992):

$$\theta = \begin{cases} \tan^{-1} \left( \frac{T - Q + \sqrt{(T - Q)^2 + 4R^2}}{2R} \right) & \text{if } T > Q \\ \tan^{-1} \left( \frac{2R}{Q - T + \sqrt{(Q - T)^2 + 4R^2}} \right) & \text{if } T \leq Q, \end{cases} \quad (19)$$

where  $R$ ,  $Q$ ,  $T$  are the coefficients determining the lengths of the major, minor axis and the orientation of the ellipse (equation of ellipse expressed in quadratic form:  $Qx^2 + 2Rxy + Ty^2 = U$ ). Second order spatial moments of the extracted region served for the estimation of the coefficients. It is assumed that the ellipse has the same second-moments as the region (Haralick, Shapiro, 1992). The coefficients are found from the normalized spatial moments and for the unit length pixel could be defined as:

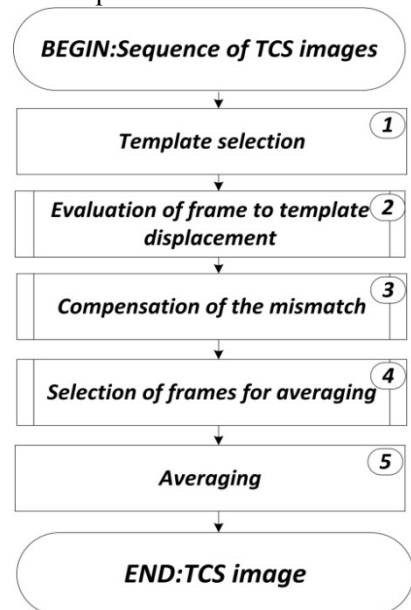


**Fig. 3.2** The block diagram of the algorithm used for the suppression of noise in TCS images

$$Q = \frac{1}{N} \cdot \sum_{i=1}^N (x_i - \bar{x})^2 + \frac{1}{12}, \quad (20a)$$

$$T = \frac{1}{N} \cdot \sum_{i=1}^N (y_i - \bar{y})^2 + \frac{1}{12}, \quad (20b)$$

$$R = \frac{1}{N} \cdot \sum_{i=1}^N (x_i - \bar{x})(y_i - \bar{y}), \quad (20c)$$

where  $\bar{x}, \bar{y}$  are the coordinates of the mass centre of the extracted region;  $N$  is the number of pixels in the extracted bone region. The mass centre is found by taking the mean of rows and columns indices in an image. The coordinates of the mass centre served for a relative FtR shift ( $\delta x, \delta y$ ) estimation. The mismatch between the frames was estimated by finding the difference between the orientation and the shift of the reference frame and consecutive frames (2). Since the mismatch (shift and orientation) of frames becomes known, the misaligning of frames due to the transducer movements could be compensated. The displacement correction was made by applying the affine transformation of the whole sequence of raw frames. Equation 21 represents an affine transformation of a single pixel in a single TCS frame:

$$\begin{bmatrix} x_c \\ y_c \end{bmatrix} = \begin{bmatrix} s_x \cdot \cos \Theta_{FtR} & -s_x \cdot \sin \Theta_{FtR} \\ s_y \cdot \sin \Theta_{FtR} & s_y \cdot \cos \Theta_{FtR} \end{bmatrix} \cdot \begin{bmatrix} x \\ y \end{bmatrix} + \begin{bmatrix} \delta x \\ \delta y \end{bmatrix}, \quad (21)$$

where  $x_c, y_c$  are position of image pixel after the displacement compensation;  $s_x, s_y$  are scale parameters (in this case, the scale parameter was constant in the sequence [ $s_x, s_y$ ] = 1). When the transform coordinates of each frame were found, all the frames were rearranged into the regular grid via cubic interpolation (3). It was assumed that there are few main sources of errors having influence on the averaging efficiency. At first, some of the B-scans might be acquired by tilting the probe from the major scanning plane, and the cross-sections are not the same. Secondly, the inaccurate estimation of mismatch between the frames is as well possible. Thirdly, the movements of a probe might be too slow with respect to the frame acquisition rate, and the interference conditions are not altered in the sequence. These factors were taken into account and supplementary procedure for preselection of eligible frames was included into the processing chain (4). The spatial match of the scanned brain structures between the frames was estimated by using the 2D normalized correlation coefficient. The coefficient between the two matrixes  $\mathbf{X}$  and  $\mathbf{Y}$  is defined as:

$$r = \frac{\sum_{i=1}^M \sum_{j=1}^N (\mathbf{X}_{i,j} - \bar{\mathbf{X}})(\mathbf{Y}_{i,j} - \bar{\mathbf{Y}})}{\sqrt{\left( \sum_{i=1}^M \sum_{j=1}^N (\mathbf{X}_{i,j} - \bar{\mathbf{X}})^2 \right) \cdot \left( \sum_{i=1}^M \sum_{j=1}^N (\mathbf{Y}_{i,j} - \bar{\mathbf{Y}})^2 \right)}}, \quad (22)$$

where  $M, N$  – dimensions of a matrices,  $\bar{\mathbf{X}}$  – mean value of a matrix  $\mathbf{X}$ . This parameter was calculated by comparing the same region in each frame of a sequence with the region in the reference frame. The high reflectivity region representing *basal cisterns* was selected for the estimation expecting high correlation within this region. The frames were discarded from the sequence as inappropriate if  $r < 0.75$  (thus avoiding first and second type errors). The frame decorrelation ratio was estimated by comparing the low echogenicity regions which were expected to be homogeneous (region of CSF served for this purpose). The correlation coefficient between all the frames in a sequence frame to frame (FtF) was calculated. The regions were selected manually by outlining the rectangle in a reference frame. An example of the TCS image with preselected regions is presented in Fig. 3.3 (A). FtF correlation was analysed via correlation matrix:

$$\mathbf{R} = \begin{bmatrix} r_{1,1} & \dots & r_{1,K} \\ \dots & \dots & \dots \\ r_{K,1} & \dots & r_{K,K} \end{bmatrix}, \quad (23)$$

where  $K$  is the number of frames in a sequence. All the frames having at least 15 correlated “colleagues” ( $r > 0.7$ ) were removed from a sequence. The thresholds for the frames preselection were set experimentally by observing the outcome of the algorithm. An example of the correlation matrix is presented in Fig. 3.3 B.

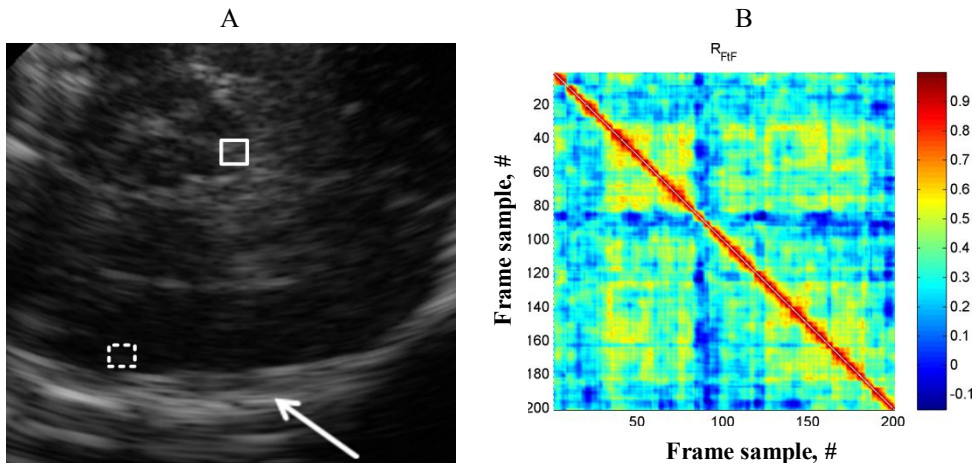


**Fig. 3.3** (A) An illustration of ROI selection for FtF correlation (echo-poor region, dashed line rectangle ) and structural misplacement (high reflectivity region, solid line rectangle) estimation, white arrow indicates the contralateral to the probe skull bone used for the FtR mismatch estimation, (B) an example of FtF correlation matrix estimated in a low echogenicity region

Finally, the “drafted” frames were averaged. The results illustrating the efficiency of the proposed algorithm are presented in subsection 4.1. The averaging of the frames deccorelated in the sense of speckle preserves the texture of the images; meanwhile,

most of the despeckling algorithms proposed by the other authors (based on the multiresolutional analysis and anisotropic diffusion, Lee filter etc.) use a simple image smoothing by skipping the edges detected using certain criteria.

### 3.2. Automated algorithms for the midbrain segmentation

Segmentation of the SOI is strongly under the influence of the quality of data in the ultrasonic imaging. Limited, variable spatial resolution and contrast, speckle noise are the barriers constraining the possibilities to detect the boundaries of the ROI in the images by accurately making the segmentation of ultrasound images to a challenging and non-trivial task. This subsection presents two algorithms developed for the midbrain region segmentation in the TCS images. At first, the latest superior technique based on the statistical shape model and amplitude-invariant local phase-based acoustic boundary detector is presented. Secondly, the active contour (AC) based algorithm proposed in the earlier research is briefly introduced.

#### 3.2.1. Shape modelling based approach

The area of interest in the transcranial ultrasound images has a characteristic shape feature. Frequently, the expression “butterfly-shaped midbrain” (see Figure 3.4 (A)) is used. Taking into account this feature and the experience of the professional neurosonographer, the statistical shape model (SSM) of the midbrain contour was constructed and fitted with the use of an amplitude invariant local phase based on the step edge detector.

##### 3.2.1.1. Statistical shape model

The principle of statistical (active) shape model (SSM) was employed for the semi-automatic segmentation of the midbrain. The principle is applicable when the desired region has a characteristic shape feature, and only comparably soft shape variation occurs from case to case. A comprehensive tutorial for constructing statistical shapes could be found in Coote’s papers (Cootes, 2000; Cootes et al., 1995). The goal of statistical shape modelling is to create the parameterized model of the form  $\mathbf{x} = \mathbf{M}(\mathbf{b})$ , which is used to generate new shapes similar to the examples in the original training set. The SSM is constructed having  $M$  training shapes  $\mathbf{x}_i$  aligned in a common coordinate frame. Any shape in a training set could be defined as a sum of mean shape  $\bar{\mathbf{x}}$  and a plausible deviation of shape controlled by the vector  $\mathbf{b}$ :

$$\mathbf{x} \approx \bar{\mathbf{x}} + \mathbf{P}\mathbf{b} \quad , \quad (24)$$

where  $\mathbf{x} = (x_1, \dots, x_n, y_1, \dots, y_n)^T$  the  $2n$  length vector of shape points’ coordinates (midbrain contour),  $n$  – number of contour points,  $\bar{\mathbf{x}}$  – mean shape obtained by averaging  $M$  aligned training shapes.  $\mathbf{P}$  is a matrix of the eigenvectors obtained by performing the principal component analysis of the training shapes set. The shapes were aligned by the means of Procrustes Analysis (Goodall, 1991). The alignment procedure could be explained by the following stages:

1. each shape of a training set is translated that its centre of gravity is at the origin;
2. the initial mean shape is selected  $\bar{\mathbf{x}}$  and scaled to  $|\bar{\mathbf{x}}|=1$ ;
3. all the other shapes are aligned respectively to the mean shape;
4. the mean shape is re-estimated;
5. reiteration from step 3) while the mean shape converges.

The variation modes of shape points are represented by unit eigenvectors  $\mathbf{p}_i$  of the covariance matrix  $\mathbf{C}$ :

$$\mathbf{C}\mathbf{P} = \Lambda_i\mathbf{P}, \quad (25)$$

where the covariance matrix  $\mathbf{C}$  could be expressed as:

$$\mathbf{C} = \frac{1}{M} \sum_{i=1}^M (\mathbf{x}_i - \bar{\mathbf{x}})(\mathbf{x}_i - \bar{\mathbf{x}})^T, \quad (26)$$

$\Lambda_i$  – the  $i$ -th eigenvalue of  $\mathbf{C}$ . The majority of the total shape variation can be defined by the first few modes. Therefore, the shape model was constructed by using the reduced matrix  $\mathbf{P} = (\mathbf{p}_1|\mathbf{p}_2|\mathbf{p}_3|\dots|\mathbf{p}_K)$ , and  $K$  is the predefined number of meaningful eigenvalues. New realistic shapes could be generated by varying parameters  $b_i$  with respect to the present amount of variance in a model determined by eigenvalues  $\Lambda_i$ .

Having constructed SSM, it is possible to search and segment the structure in an image by matching the model to the plausible midbrain boundary points. The model points in an image frame are defined by the equation:

$$\mathbf{x} = T(\bar{\mathbf{x}} + \mathbf{P}\mathbf{b}), \quad (27)$$

where  $T$  is a transform of scale ( $s_x, s_y$ ), rotation ( $\theta$ ) and shift ( $x_t, y_t$ ). For one point  $(x_i, y_i)$ ,  $T$  could be defined by an affine transform (see 21 expression). The procedure of the SSM fitting could be explained in three steps. At first, the initialization of SSM based segmentation is performed. The mean contour of midbrain  $\bar{\mathbf{x}}$  obtained during the development of SSM is used as a seed shape.

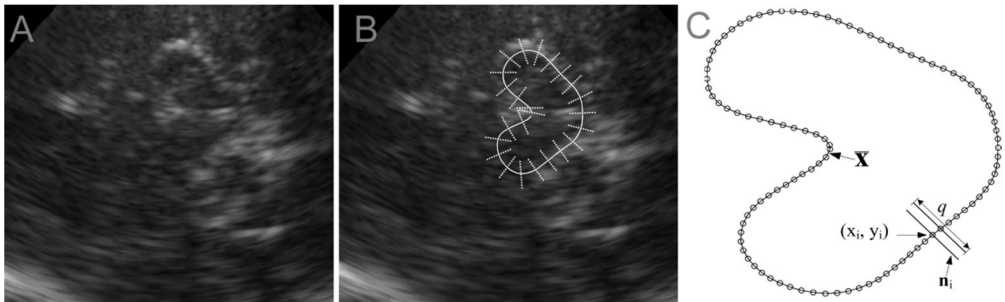


**Fig. 3.4** (A) An example of TCS image, (B) an illustration of TCS image together with manually placed seed shape of the midbrain (solid line) and several orthogonal intensity lines (pointed lines), (C) the sketch illustrating the procedure of intensity projections computation

The seed shape is manually placed in the image frame (see Fig. 3.4 (B)) adjusting the scale and orientation. A convenient graphical user interface was developed for this purpose (see chapter 5). Secondly, the plausible midbrain boundary points in the image frame are detected. A detailed explanation of the plausible points detection procedure is given in the subsection 3.2.1.2. Finally, the midbrain boundary in an image is extracted by solving constrained optimization problem. The optimal contour controlling parameters (shape, scale, shift and orientation) is found by minimizing the squared sum of distances between the model and plausible boundary points:

$$\min_{\substack{x_t, y_t, s_x, \\ s_y, \theta, \mathbf{b}}} \left\{ \sum [\mathbf{y} - T(\bar{\mathbf{x}} + \mathbf{P}\mathbf{b})]^2 \right\}, \quad (28)$$

where  $\mathbf{y}$  is the vector of plausible midbrain boundary points coordinates. Finally, the segmented midbrain boundary points vector  $\mathbf{g} = (x_1, \dots, x_n, y_1, \dots, y_n)^T$  is found by using the determined optimal transformation parameters. The shape optimization constraints ensure the generation of realistic shape. The pattern search optimization (Audet and Dennis, 2003) was applied for solving the constrained optimization problem. The scheme of proposed algorithm is presented in Figure 3.5.

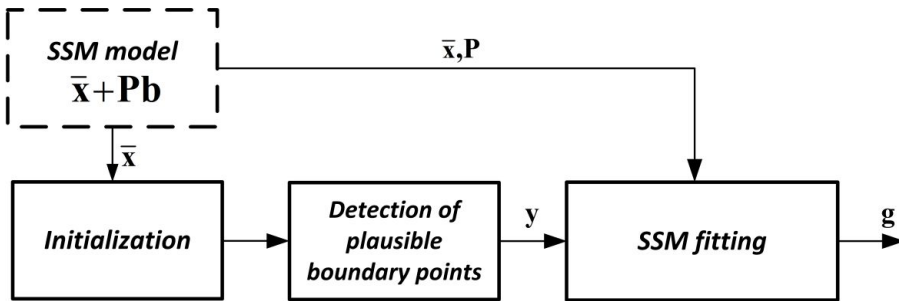


Fig. 3.5 The scheme of the proposed algorithm

### 3.2.1.2. Detection of midbrain boundary points based on the local phase congruency

It has been demonstrated that the image features, such as step edges and intensity ridges, could be detected by analysing the local phase congruency at different scales of image (Kovesi, 1996). Mulet-Parada and Noble were the first who had pioneered a successful approach for the boundary detection exploiting the local phase congruency at different scales of image in the echocardiography (Mulet-Parada and Noble, 2000). The key advantage of phase based method is the invariance to amplitude; thus, the boundary can be detected even if the contrast at the boundary is very low and spatially variable due to the depth-dependent signal level degradation.

Local phase congruency based strategy was proposed for the determination of plausible midbrain boundary points. It was expected that the local phase based detector will be more robust to the user predefined scanning settings contrary to the

learning based approach proposed by Engel and Toennies (2009). The ideal boundary in ultrasound image can be modelled as a step edge function between the two structures having different acoustic impedance. In case of step edge, all the Fourier components are in phase and equal to 0 at positive edge,  $\pi$  at negative and  $\pi/2$  at intensity ridges; meanwhile, the phase deviates otherwise. Respectively, these structures can be recognized by analysing the local phase in different frequency subbands. An illustration of ideal positive step edge function together with forming Fourier components is shown in Figure 3.6. The multiresolutional analysis of local image intensity lines (latter

intensity projections)  $I(\mathbf{n}_i)$  orthogonal to the seed shape was performed in this approach. The projection lines of predefined length  $d$  (see Figure 3.4 C) were computed for  $n$  points of seed shape. All the projections were organized efferently, thus preserving the crossing of the midbrain boundary (darker area in an image) surrounding the tissue (more echogenic area) in the same manner. An illustration of intensity projections is presented in Figure 3.4 (B) and (C). The intensity projections were decomposed into a frequency subbands by convolving them with a bank of wavelet filters (Kovesi, 1996). The filters are designed that the frequency responses would slightly overlap to ensure the uniform representation of spectrum across the scales. The local frequency information was obtained by applying the quadrature log-Gabor filter. The frequency domain log-Gabor quadrature filter is defined as (Kovesi, 1996):

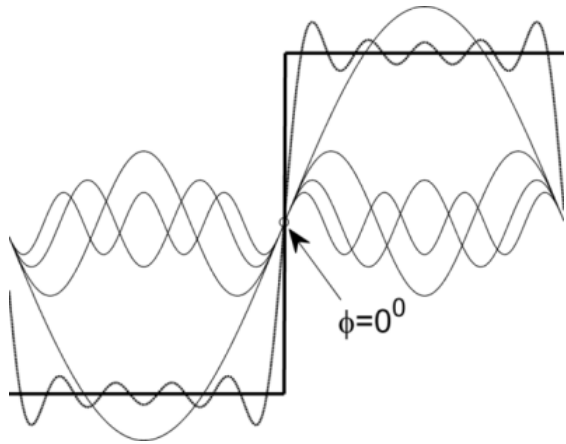


**Fig. 3.6** Positive step edge function together with the forming Fourier components

The filters are designed that the frequency responses would slightly overlap to ensure the uniform representation of spectrum across the scales. The local frequency information was obtained by applying the quadrature log-Gabor filter. The frequency domain log-Gabor quadrature filter is defined as (Kovesi, 1996):

$$G(\omega) = \exp\left(-\frac{\log(\omega/\omega_0)^2}{2(\log(\kappa/\omega_0))}\right), \quad (29)$$

where  $\kappa$  – parameter of the bandwidth of a filter,  $\omega_0$  – centre spatial frequency of a filter. The set of the filtering scales is obtained by decreasing the centre frequency of a filter  $\omega_0$  by predefined decrement step. The proportion  $\kappa/\omega_0$  preserves a constant shape-bandwidth ratio. A Hamming window was applied to the intensity projections before performing log-Gabor filtering in order to avoid spectral leakage. The local phase angle estimate at the predefined scale  $j$  of  $i$ -th intensity projection is obtained from an expression:

$$\phi_j(\mathbf{n}_i) = \tan^{-1}\left[F^{-1}(I_i(\omega) \cdot G_j(\omega))\right], \quad (30)$$

where  $I_i(\omega)$  –  $i$ -th intensity projection in the Fourier domain,  $j = 1 \dots s$ ,  $s$  – number of filtering scales,  $F^{-1}$  – inverse Fourier transform. The local phase scalogram of a single intensity projection is demonstrated in Figure 3.7 C. There each column of scalogram is assumed to be a local Fourier spectrum of corresponding intensity projection. It could be noticed that the phase remains quite stable between the scales where the waveform are closer to step edge function; otherwise, the phase deviates.

The global minimum of the averaged local phase scalogram served as an indicator of plausible boundary point, because the phase angle is close to 0 where the waveform is similar to the positive edge. The extrema is found at the location where the phase deviates least and are close to 0. It is assumed that the minimum corresponds to positive edge and indicates plausible midbrain boundary point. The plausible boundary point at  $i$ -th projection is found by:

$$y_i = \arg \min_{\mathbf{n}_i} \left\{ \frac{1}{s} \sum_{j=1}^s \phi_j(\mathbf{n}_i) \right\}, \quad (31)$$

where the phase varies between 0 and  $2\pi$ . An illustration of the plausible boundary point detection procedure is presented in Figure 3.7. The algorithm parameters (number of scales  $s$ , the number of contour points  $n$ , length of intensity projection  $d$  etc.) are presented and motivated in a subsection 4.2.

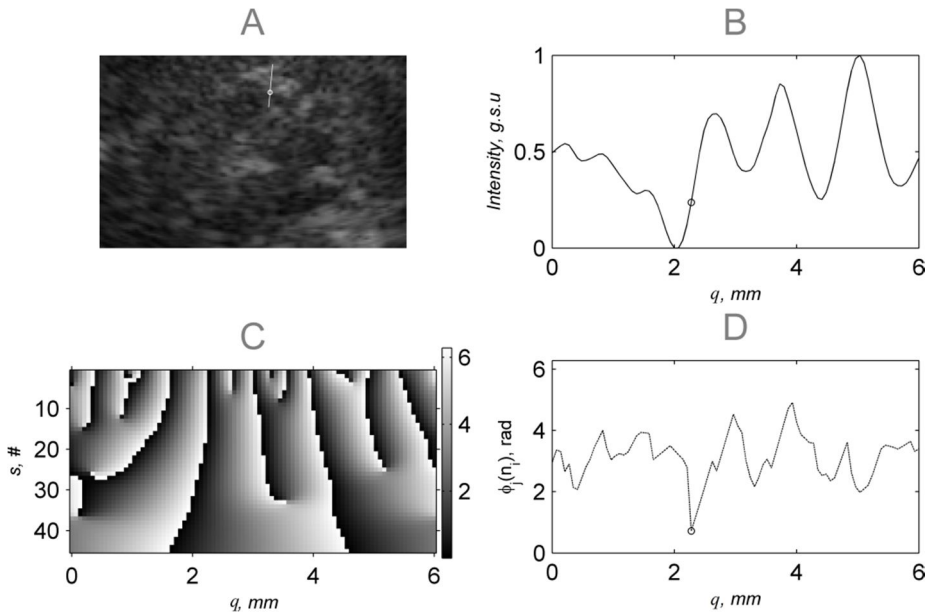


**Fig. 3.7** Plausible boundary point detection procedure: (A) TCS image together with one intensity line and detected plausible boundary point (marked as a circle), when  $q = 6$  mm, (B) normalized intensity projection shown in (A), (C) local phase scalogram ( $s = 50$ ), (D) averaged local phase characteristics together with the detected extrema indicating plausible midbrain boundary point

### 3.2.2. Active contour based approach

The first approach proposed for the midbrain segmentation was based on AC. The AC is a superior choice if the task is to fit a closed curve to the object boundary in an image even if the part of it is missing or diffusive. The ability to approximate respectively to set constraints makes AC into an attractive image segmentation tool gaining popularity in the ultrasonic image processing. The AC is a parametric curve  $\chi_m = (x_m, y_m)$  defined by a finite number of control points  $m = 1 \dots M$ . AC is based on the energy functional (see expression 32) which is minimized, thus fitting the initial curve to the desired boundaries of regions in the image frame. The energy functional is produced by two terms  $E_{int}(\chi_m)$ ,  $E_{ext}(\chi_m)$  that are the internal and external energies of a contour:

$$E_{Contour} = \int E_{int}(\chi_m) + E_{ext}(\chi_m) dm. \quad (32)$$

The internal energy is as well frequently called the elastic energy, since it preserves the contours continuity and smoothness. The  $E_{int}$  is a summation of forces applied along the curve, and it is defined as:

$$E_{int}(\chi_m) = (\alpha_{int} \left| \chi_m' \right|^2 + \beta_{int} \left| \chi_m'' \right|^2) / 2, \quad (33)$$

where the user predefined constants  $\alpha_{int}$ ,  $\beta_{int}$  sets the relative weight of tension (“length”) and degree of the curvature of the contour,  $\chi_m'$ ,  $\chi_m''$  which are first and second order derivatives of the contour. The  $E_{int}$  term ensures constant velocity and acceleration of the contour. Larger weight of the continuity term limits the changes of distances between the points. The large smoothness weight constrains the ability to adapt to the narrow concave boundaries, but too low  $\beta_{int}$  could result in the “noisy” contour.

The external (potential) energy  $E_{ext}$  is the image dependant and exploits the information of it, thus attracting the initial shape to the boundaries of the object (in this case, the midbrain). In the original version of AC (Kass et al., 1988), it was proposed to combine three weighted components in order to define  $E_{ext}$  line energy, edge energy and termination energy:

$$E_{ext} = w_{line} E_{line} + w_{edge} E_{edge} + w_{term} E_{term}. \quad (34)$$

The first term is based on the absolute intensity of the image (the sign of the weighting coefficient determines whether a brighter or darker region is an attractor);  $E_{term}$  helps to drive the curve in the sharp corners and approximate the missing boundaries, and  $E_{edge}$  attracts the contour to the image edges.  $E_{term}$  component is rarely used, since the shapes in the medical images are relatively smooth. Furthermore, it is possible to ensure the closed approximating contour via  $E_{int}$ , and this is more convenient. The line energy could be efficiently employed when the initial contour is situated clearly inside or outside of the object, and the intensity is relatively homogeneous within. This condition is hardly fulfilled in the case of the ultrasonic midbrain image; therefore, only the edge energy term was used in the

proposed approach. The intensity gradient of the low-pass filtered image version served as an external image force:

$$E_{ext} = -\left| \nabla [G_{\sigma}(x,y) * I(x,y)] \right|^2, \quad (35)$$

where  $G_{\sigma}(x,y)$  is the 2D Gaussian function with standard deviation  $\sigma$ ;  $I(x,y)$  is the grayscale image. The low-pass filtering reduces the influence of small and possibly false edges caused by the high frequency noise. The minimum of energy functional is obtained when the external and internal forces are in balance. The external force computation based on the gradient vector flow (GVF) field defined by Chenyang Xu (Xu and Prince, 1998) was used. GVF is convenient to express via Euler equations:

$$\gamma \nabla^2 u - (u - f_x) \cdot (f_x^2 + f_y^2) = 0, \quad (36a)$$

$$\gamma \nabla^2 v - (v - f_y) \cdot (f_x^2 + f_y^2) = 0, \quad (36b)$$

where  $\gamma$  – regularization term (in this case, 0.2),  $\nabla$  – Laplace operator (second order derivative),  $f_{x,y} = \partial E_{ext} / \partial(x,y)$ ,  $u, v$  – components of the vector field. GVF based external force makes the AC to work well even if it is initialized far from the boundaries of the object, and it is capable to adapt to the concave regions. The GVF is organized in such manner that the regions without intensity gradient are filled with the information obtained in the closest edge-rich regions. The minimization of an energy function (32) could be realized via the gradient descent or adjusting the number of iterations needed for the converge. In the presented case, the fixed number of iterations was 100. The comprehensive tutorials on constructing AC could be found in El-Baz (2011), Xu and Prince (1998), Kass et al. (1988).

The block diagram of the proposed midbrain segmentation algorithm is presented in Fig. 3.8

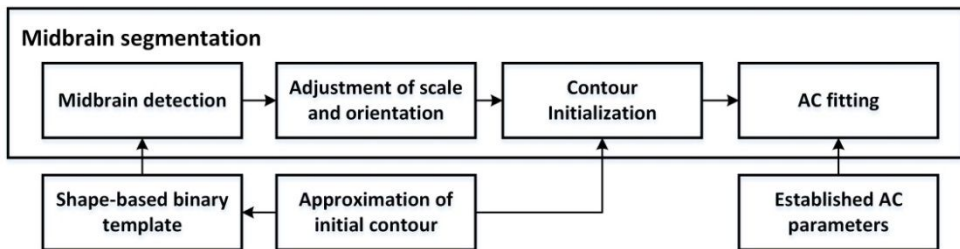


Fig. 3.8 Block diagram of the AC based midbrain segmentation algorithm

**Initial contour.** The initial contour (shape)  $\chi_m(x_m, y_m)$  for the AC segmentation was established with an assistance of the expert. The physician manually delineated an area of the midbrain in a few TCS images. The contours were aligned, and the average shape was established. It is known that the geometry of the objects appears a bit distorted in the ultrasonic images, and the degree of distortion increases together with a scanning depth. Therefore, only the half of averaged contour closer to the scanning probe was used assuming that the other half has to be symmetric. The initial shape is presented in Fig. 3.9 together with the TCS image.

**Midbrain detection.** The contour has to be initialized near to the echogenic boundary of the midbrain, because the convergence of the AC contour is dependent on the image gradient information, and this makes the AC method sensitive to the speckle noise, which causes comparatively strong gradients in the ROI; moreover, the contour could be attracted to the other echogenic brain structures (e.g. *aqueduct of sylvius*). In the first stage of the algorithm, the approximate midbrain location was detected by the means of template matching. A rectangular binary template image was produced by converting the shape-based initial contour  $\chi_m(x_m, y_m)$  of the midbrain to a binary mask. The normalized 2D cross-correlation (see formula 22) served as a match criterion. It should be mentioned that such approach is relatively robust, since the potential information is lost during the binary conversion. In further attempts, it was substituted by the manual initialization, since the better outcome is achieved then.

**Adjustment of scale and orientation.** The scale and orientation of the midbrain are slightly variable between the cases; therefore, the stage for the scale and orientation adjustment was incorporated. The scale and orientation of the template were adjusted when the coarse location was determined. The search was performed in the predefined range ( $s: \pm 30\%$ ,  $\Theta = \pm 15^\circ$ ).

**AC parameters.** The parameters for appropriate control of the AC were determined after the iterative search. An initial contour of the midbrain was aligned to one of the contours, previously manually marked by a physician neurologist, changing the values in the set of parameters of the AC until the desired correspondence between these contours was achieved. HD (for HD definition, see 4.2 subsection) was selected as a measure of adequacy. The iterative search was stopped when lower than half the pixel size HD value was reached. The main AC parameters are:  $\alpha_{int} = 1.08$ ,  $\beta_{int} = 0.27$ ,  $\sigma = 3$ , number of iterations 100. These parameters were used in all the later attempts to segment the midbrain. The shortage of AC is the number of adjustable parameters. From personal experience, it is really brittle to determine the set of parameters which makes AC to perform well with all the tested cases.

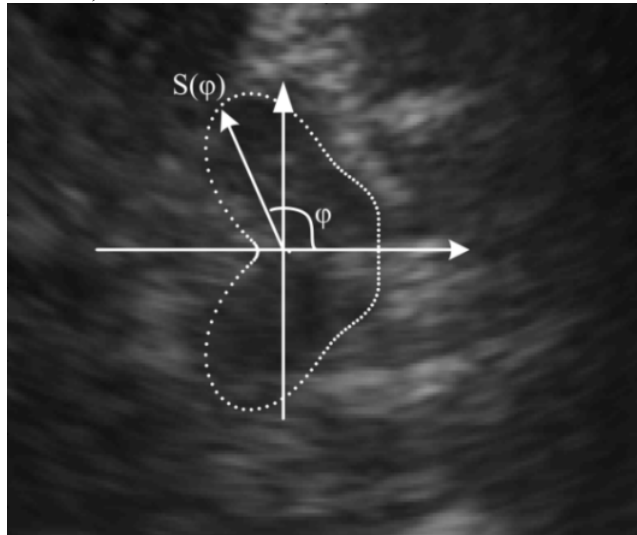


**Fig. 3.9** An approximation, manufactured averaging few manual delineations, used as an initial AC together with a TCS image of the midbrain

### 3.3. Segmentation of intra-mesencephalic brain structures

Two algorithms were developed for the extraction of intra-mesencephalic brain regions: the first assumes that the SN area could be fragmented in the ultrasonic image, and it is supposed that the exact SN region is extracted then (3.3.1. subsection). In the second approach (3.3.2. subsection), it is handled as a continuous region. The localized intra-mesencephalic region containing SN area inside is outlined and used for the echogenicity estimation.

#### 3.3.1. SN region extraction algorithm

In the conventional TCS examination, the neurosonologist is trying to assess the mesencephalon bilaterally but estimates only the SN area of symmetric midbrain which is closer to the scanning probe due to the causes discussed in 1.3. subsection. Such field of search reduction was incorporated in the SN extraction algorithm. Only the proximal half of the midbrain ( $\frac{1}{2}$  ROI) extracted by the PSSM was analysed. Fig. 3.11 (A) presents an example of  $\frac{1}{2}$  ROI segmented by PSSM. The pixel-level classifier based segmentation strategy was applied for the extraction of SN region. Each pixel in  $\frac{1}{2}$  ROI was defined by a specific set of features carrying information about the relative location with respect to the extracted midbrain boundaries, relative intensity and intensity variability in the neighbourhood. Pixels in  $\frac{1}{2}$  ROI were expected to be assigned into two classes,  $\Omega$  (sub-regions): (1) SN surrounding tissue (tegmentum), (2) substantia nigra region, respective to the weight of the features of the training set. Such approach was selected aiming to employ:

- anatomical prior knowledge about the location of SN in the mesencephalic frame;
- experience of the sonographer (empirical data);
- knowledge about the existing intensity gradient between the SN and surroundings in the ultrasonic images.

Engel (Engel et al., 2009) used a shape prior for the SN segmentation, but the review of manually outlined TCS images and findings of histologists (Damier et al., 1999b; Blazejewska et al., 2013) demonstrate that the shape constraint could be relatively robust, especially in the case of degeneration. Few examples of SN outlined by a neurosonologist (SN region marked as 2) are presented in Fig. 3.10: (A) and (B) are PD affected patients, (C) and (D) subjects from a control group. The examples demonstrate that not all the outlined SN pixels have a relatively larger intensities, and the intensity gradient at the boundary are frequently obscure. It is obvious that the neurosonologist implies an anatomical knowledge about the shape and location of SN. Moreover, the ultrasonic imaging is quite unique due to certain dynamics. The evaluation performing operator can take into account the adjacent cross-sections of the SN and predict the region boundary even if it is not expressed in an image. The prior knowledge about the location, shape and contrast frequently advices to use a parametric region based segmentation algorithms (e.g. AC), but the SN region typically consists of 50-200 pixels, and frequently the intensity gradient is relatively weak at the boundary; thus, it was expected that the pixel-level technique will be more efficient to compare with the region based methods.

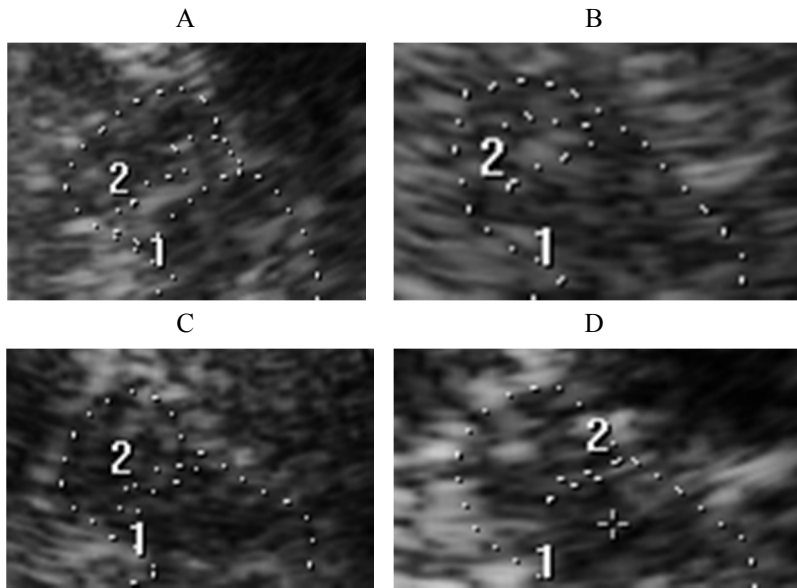


**Fig. 3.10** Few examples of SN and  $\frac{1}{2}$  of the midbrain (no. 1) outlined by a neurosonologist (SN region marked by no. 2): (A) and (B) PD affected patients, (C) and (D) control group subjects

Fifteen potential features candidates were tested for the characterization of pixels in  $\frac{1}{2}$  ROI, such as intensity gradient, distances between the pixels and various reference points, the ratio between the low pass filtered and high pass filtered versions of the images etc. Finally, a set containing 8 most informative features (only these features are presented in detail in the dissertation) was established. The informative features were determined by observing the outcome of the algorithm (the efficiency evaluation results are presented in a subsection 4.3). The features mainly having relation with the intensity, its local spread (4 features) and relative location (4 features) of SN region was included in the final feature set. Figure 3.11 (B) presents the sketch of  $\frac{1}{2}$  ROI illustrating the selected features. Four Euclidean distances defining the relative range between the reference point and the centre of each pixel in  $\frac{1}{2}$  ROI were included in the feature vector. The midpoint (distance  $\zeta_3$ ) in the notch of the contour and left-right neighbours ( $\zeta_2$ ,  $\zeta_4$ ) were selected as the reference points. The geometric centre of the extracted  $\frac{1}{2}$  ROI contour served as the fourth reference point  $\zeta_1$  for the distance estimation. The amplitude values in  $\frac{1}{2}$  ROI were normalized before the estimation of grayscale based features.

Intensity values in  $\frac{1}{2}$  ROI were adjusted by shifting to the same mean intensity in ROI in all the cases (the established  $\frac{1}{2}$  ROI mean is 0.14, when the range is 0...1). This step was applied in order to reduce the relative amplitude differences arising due to the user predefined scanning settings. The intensity based features were selected taking into account the fact that the SN region is in contrast with the surroundings even for the healthy subjects. Respectively, the aim was to evaluate the

local intensity variation expecting to achieve the indirect estimate of intensity in the neighbourhood.

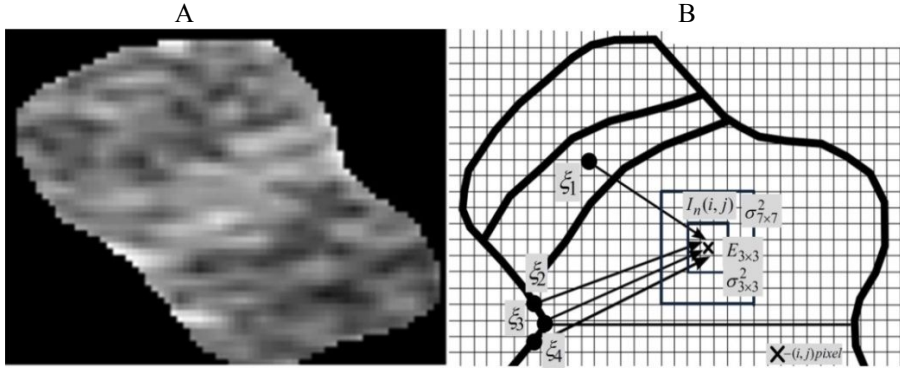


**Fig. 3.11** SN extraction algorithm: (A) an example of  $\frac{1}{2}$  ROI used for the SN area extraction, (B) the sketch illustrating the features used for the characterization of  $i$ -th pixel in  $\frac{1}{2}$  ROI (● – reference point, × –  $i$ -th pixel,  $E_{3 \times 3}$  – local entropy ( $3 \times 3$  window),  $\sigma_{3 \times 3}^2$ ,  $\sigma_{7 \times 7}^2$  – local variance,  $I_n(i, j)$  – normalized spatial intensity function)

Four amplitude based features were preselected: (1) the absolute value of normalized amplitude, the local intensity spread was estimated by the variance in two different windows  $3 \times 3$  (2) and  $7 \times 7$  (3). The local variance for  $i$ -th pixel estimated in  $N \times N$  window is as follows:

$$\sigma_{i, N \times N}^2 = \frac{1}{N^2} \cdot \sum_{j=1}^{N^2} (I_j - \bar{I})^2, \quad (37)$$

where  $\bar{I}$  is the mean intensity value in  $N \times N$  window. Local entropy (4) could be defined as:

$$E_{N \times N} = - \sum_{j=1}^{N^2} p_j \cdot \log_2(p_j), \quad (38)$$

$p_j$  – probability of gray level occurrence in a  $N \times N$  window,  $j = 1 \dots m$  number of gray levels in an image.

The used classifier was based on the Mahalanobis (Mahalanobis, 1936) distance. Mahalanobis measure is defined as the distance between the two feature vectors (sample and training)  $\mathbf{x} = (x_1, \dots, x_p)^T$  and  $\mathbf{y} = (y_1, \dots, y_p)^T$  in the  $p$ -dimensional space  $R^p$ :

$$D_{\Omega i}(\mathbf{x}, \mathbf{y}) = \sqrt{(\mathbf{x} - \boldsymbol{\mu}_y)^T \mathbf{S}^{-1} (\mathbf{x} - \boldsymbol{\mu}_y)}, \quad (39)$$

where  $\mathbf{S}$  – the covariance matrix of the training set,  $\boldsymbol{\mu}_y$  – mean training feature vector. Mahalanobis distance is an attractive tool, since it takes into account the natural spread and correlations between the features in a data set. The features

having higher spread receive lower weight. The  $i$ -th pixel is assigned to the class respectively to the lower Mahalanobis distance from the feature vectors (SN and surroundings groups) in a training set:

$$\Omega_i = \begin{cases} 1, & \text{if } D_{1,i} > D_{2,i} \\ 0, & \text{otherwise} \end{cases}. \quad (40)$$

The shortage of the classifier based approach is that in some cases the single non-connected pixels are assigned to the SN group or vice versa. Gentle median filtering was applied for the removal of these outliers. In the final processing stage, the contours of SN in a binary image were extracted by the means of boundary tracing (Gonzalez, 2004). The stages of the proposed algorithm are presented in the Table 3.1.

**Table 3.1** SN extraction algorithm

SN extraction algorithm	
<b>1. <math>\frac{1}{2}</math> ROI extraction</b>	Extraction of the $\frac{1}{2}$ of mesencephalon outlined by the PSSM closed by the curve: $\mathbf{g} = (x_1, \dots, x_{n/2}, y_1, \dots, y_{n/2})^T$ .
<b>2. Amplitude normalization</b>	Intensity values in $\frac{1}{2}$ ROI were adjusted by shifting to the same mean in all the cases.
<b>3. Feature extraction</b>	Euclidean distances $\zeta_{1-i, i}$ , $\sigma_{i, N \times N}^2$ , $E_{i, N \times N}$ , $I_n$ , see Fig. 3.11 (B) and formulas (37), (38).
<b>4. Classification</b>	Assignment of pixels to classes: SN ( $\Omega_2$ ) or surroundings ( $\Omega_1$ ). See formulas (39) and (40).
<b>5. Post-processing</b>	Removal of outliers (single non-connected pixels): median filtering ( $5 \times 5$ window).
<b>6. Contour-extraction</b>	The contours outlining the SN pixels were extracted by the means of boundary tracing (Gonzalez et al., 2004). The extraction of boundary was based on the 8-connectivity directional search.

### 3.3.2. The segmentation of reduced intra-mesencephalic region

The analysis of TCS methodology revealed that the scanning performed by the operator outlines the SN area by a single contour (examples in Fig. 3.10) in the majority of cases; meanwhile, the classification based segmentation does not take into account that the region should be continuous and extracts even small connected sets of pixels satisfying the predefined criteria. Respectively, two issues have to be addressed: (1) is the SN imaged by the ultrasound continuous region and (2) the delineation of the physician an appropriate reference for the evaluation of algorithm's accuracy? These considerations inspired the development of supplementary algorithm for the extraction of reduced region of interest (RROI) in

the midbrain cross-sectional images. The algorithm extracts a closed region containing SN. The method is based on the assumption that mainly two regions of different echogenicity (substantia nigra and tegmentum) having separable intensity distributions are found in the  $\frac{1}{2}$  ROI. The purpose was to extract a continuous region satisfying a certain separability criterion. This intention was implemented via search of optimal affine transform (see formula 21) of the initial shape. The inter-class variance proposed by Nobuyuki Otsu (Otsu, 1979) served as a separability criterion. The initial shape was established by using the empirical data. The mean SN shape of the healthy controls (20 cases) outlined by the experts served for this purpose. It is known that in case of degeneration, the SN region is expanding. Concerning that, the average contour of the control group was selected as an initial shape assuming that at least close to such size SN region is found in each subject. Conventionally, Otsu algorithm is applied for the determination of the optimal threshold intensity level for the image having bimodal distribution with an object and background within. It was demonstrated that the optimal threshold could be found by maximizing the inter-class variance criterion (Otsu, 1979):

$$\sigma^2(t) = \omega_1(t)\omega_2(t)[\mu_1(t) - \mu_2(t)], \quad (41)$$

where  $\sigma^2$  – inter-class variance,  $\omega$  – probability of class (1 – background, 2 – object),  $\mu$  – mean of the class separated by the threshold  $t$  (grayscale levels  $i = 0 \dots T$ ):

$$\omega_1(t) = \sum_{i=1}^t p_i, \quad \omega_2(t) = \sum_{i=t+1}^T p_i, \quad (42a)$$

$$\mu_1(t) = \sum_{i=1}^t i \cdot p_i / \omega_{1,i}, \quad \mu_2(t) = \sum_{i=t+1}^T i \cdot p_i / \omega_{2,i}. \quad (42b)$$

The optimal parameters of affine transform of the initial contour  $\mathbf{X}_{RROI} = [x_{RROI}, y_{RROI}]$  is found by maximizing Otsu criterion:

$$\max_{s_x, s_y, t_x, t_y, \theta} \left[ \sigma^2 \{ T(\mathbf{X}_{RROI}) \} \right], \quad (43)$$

where  $T$  – affine transform (see formula 21,  $s_{x,y}$  – scale parameters,  $t_{x,y}$  – shift parameter,  $\theta$  – orientation parameter,  $x_{RROI}, y_{RROI}$  – spatial coordinates of the contour. Such objective function was selected by analysing the empirical TCS data. The typical histogram of regions in  $\frac{1}{2}$  ROI and the sketch illustrating the proposed principle are presented in Fig. 3.12 (A). An example of the intensity distributions in real diagnostic TCS image (healthy control) is presented in Fig. 3.12 (B).

The empirical data were as well used for the determination of the plausible range of affine transform parameters and the location for the initial shape placement in the midbrain frame. Approximately four confidence intervals of shift and orientation, estimated analysing SN shapes of healthy controls, were set as boundary search values. Figure 3.12 (C) presents the scatter of geometric centres of manually

outlined SN shapes of healthy subjects together with the mean SN contour. The initial contour location was determined with respect to the mean shape used for the midbrain segmentation. The pose parameters obtained in a stage of PSSM segmentation was applied to the initial SN shape before fitting it.

Optimal shape, orientation and shift search was performed by applying a robust brute force type (mesh type) search strategy. All the possible combinations of the parameters were tested within the estimated bounds (shift  $\pm 3$  mm, orientation  $\pm 8^\circ$ , the scale constraints were set experimentally  $s_x = 0.3 - 1.5$ ,  $s_y = 0.4 - 4$ ). A shortage of the algorithm is that the fine deformation of the initial shape was assumed as non-essential.

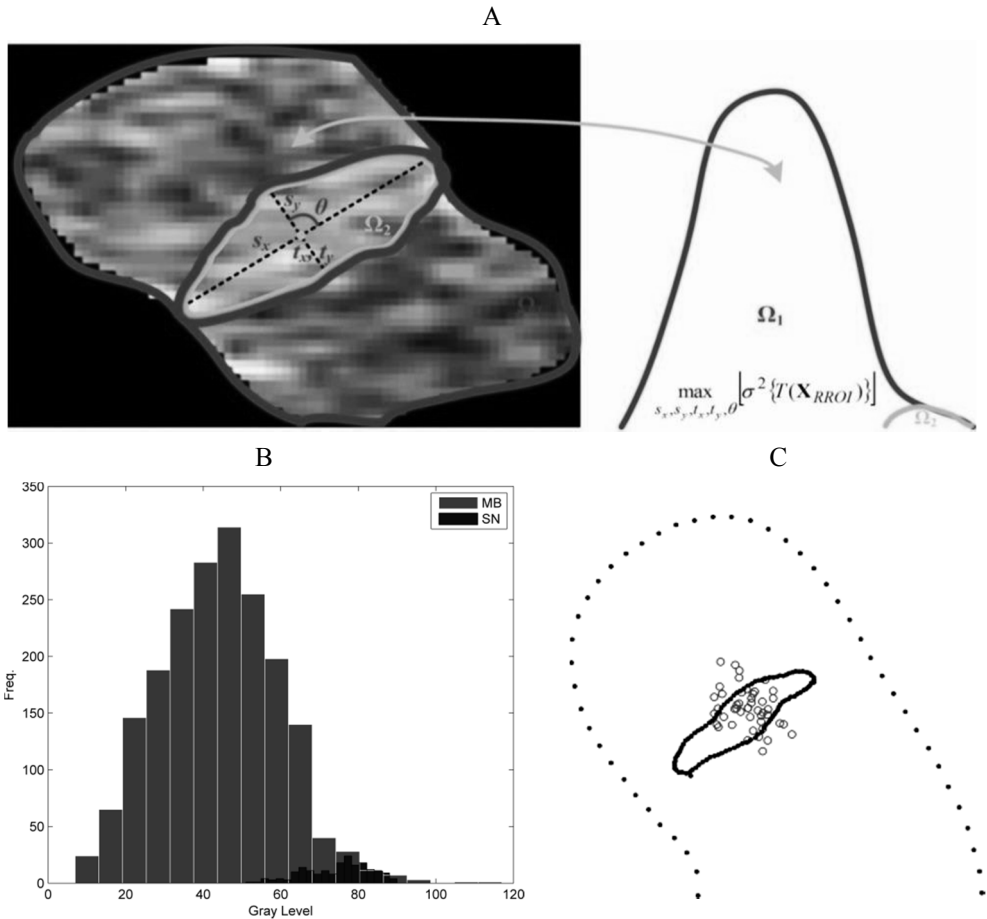


**Fig. 3.12** RROI segmentation: (A) a sketch illustrating RROI extraction algorithm: the optimal affine transform parameters (scale, shift, orientation) are determined by finding the best separation (maximizing Otsu criterion) of intensity distributions  $\Omega_1$  – background (surroundings) and  $\Omega_2$  – RROI, (B) example of typical gray level histogram of the healthy subject  $\frac{1}{2}$  ROI (black colour – SN, gray colour – all the rest in  $\frac{1}{2}$  ROI), (C) mean SN shape (solid line) together with the mean contour of the midbrain (pointed line), geometric centres of SN contours (40 cases), mean centre of the SN shapes

The algorithm extracts a bit overestimated SN region, and respectively, there is no reference to estimate its accuracy. The features of extracted RROI region were used for the midbrain echogenicity assessment.

### **3.4. Parameters and methodology for the midbrain echogenicity assessment**

Various parameters tested for the quantitative evaluation of echogenicity degree and recognition of PD related SN alteration in automatically extracted segments ( $\frac{1}{2}$  ROI, SN and RROI) are presented in the following subsection. There are several studies in this field which were discussed in the 1.6.2.2 subsection. The research group in Lübeck aimed to find observer independent image features which could help to evaluate and characterize the echogenicity in the midbrain (Kier et al., 2009; Chen et al., 2010, 2011, 2012). The research group of this study (Sakalauskas et al., 2011) aimed to reproduce the results reported by the author. The pilot study was carried out before the development of automated SOI segmentation algorithms. The manually outlined  $\frac{1}{2}$  ROI region ( $2.5 \text{ cm}^2$ , approximately 1500 pixels) served for the echogenicity analysis. The features proposed by the other authors (Kier et al., 2009; Chen et al., 2010, 2011) were combined with the features extracted using free digital image texture analysis software MaZda (Szczyplinski et al., 2007, 2009) in the pilot study. In total, 110 TCS images (61 PD affected and 49 control group) were involved in this study. Four hundred thirteen potential features of  $\frac{1}{2}$  ROI were calculated (the list of the tested feature groups is presented in Table 3.2). The achieved classification ratio was below 80% for the best tested feature subset (the detailed results are presented in 4.4. subsection), and it was substantially lower to compare with the results demonstrated by Chen et al., even using the established subset of the most informative features. It was assumed that these differences could be caused due to the image quality, which is directly dependent on the ultrasound scanning machine (more specifically user predefined scanning settings, digital filters used during the image formation procedure, level of acoustic output) used for the acquisition. Moreover, the spatial frequency analysis has few tunable parameters, such as number of scales and orientations, and therefore, it is difficult to reproduce the results. In the later researches, Al-Zubaidi et al. (2013) observed that  $\frac{1}{2}$  ROI texture analysis is dependent on the image acquisition circumstances. Furthermore, the orientation of the midbrain in B-scans depends on a relative probe-mesencephalon pose, and this could affect the repeatability of features extracted by the means of spatial frequencies and concurrence matrix (Haralick et al., 1973). These findings and results reported by Chen et al. (2012) had demonstrated that half of mesencephalon is a relatively coarse region for the abnormal SN recognition.  $\frac{1}{2}$  ROI could hardly be called a region having the texture of regular homogeneity. Nevertheless, it is a region having at least two objects having different echogenicity: SN and tegmentum; in some cases, the red nuclei appears as a third object in the B-scan images, and respectively, such integral estimation of the echogenicity, such as spatial frequencies or GLCM analysis, could be treated as methodologically wrong. Typically, SN is represented by only up to  $\sim 10\%$  of the pixels (40 – 200 pixels to compare with  $\sim 1500 - 2000$  pixels in  $\frac{1}{2}$  ROI), and this information is buried deeply.

More localized analysis is needed for the assessment of SN echogenicity and recognition of PD. With that respect, the procedure was supplemented by RROI and SN extraction algorithms and tested using the full dataset collected in LUHS during the period of 2011 – 2014. Clinical data used in the experiments are presented in the subchapter 4.4 (Tables 4.5 and 4.6). The expanded block diagram of the system part used for the research of informative features is presented in Fig. 3.14.

**Table 3.2** List of the image features used for the texture analysis in the pilot study

No.	Feature group	Main parameters	#	Reference
1.	Cocurrence matrix	Homogeneity, Correlation, Autocorrelation, Entropy etc.	22	(Chen et al., 2011)
2.	Gabor texture features	Mean and standard deviation of the magnitude of Gabor filtered image (at different scales and orientations).	60	(Chen et al., 2010)
3.	MaZda texture features	Histogram features (variance, skewness, kurtosis etc.), gradient features (absolute gradient mean, absolute gradient variance etc.), Haar wavelet features (wavelet energy at 5 different scales), Run length matrix (run length nonuniformity) etc.	352	(Szczyplinski et al., 2007; Szczyplinski et al., 2009)
4.	Moments Invariants	7 Hu moments, moment of inertia.	8	(Kier et al., 2009)
5.	Manually evaluated SN area	Size of the manually outlined SN.	1	*

\* the evaluation of SN area was performed by a professional neurosonographer.

**Potential features.** Various potential quantitative features of the automatically extracted regions ( $\frac{1}{2}$  ROI, RROI and SN) separately and the mixed relative features of the regions were used for the evaluation of echogenicity in the brain images. Fig. 3.13 presents an example of the TCS image and automatically extracted midbrain regions used for the echogenicity evaluation. A list of the tested features is presented in Table 3.3 (detailed explanation of the features and motivation is given in the Appendix 1.). The parameters for particular region are presented in separate columns of the Table 3.3. The parameters of  $\frac{1}{2}$  ROI (skewness, kurtosis, entropy, Moment of Inertia,  $1^{Hu}$  moment) were selected with respect to the pilot study (Sakalauskas et al., 2011) and the later study (Vailionytė et al., 2014) as having the highest discrimination power among the tested. The feature set proposed by Kier et al. (2009), Chen et al. (2010, 2011), Al-Zubaidi et al. (2013) and the SN indicator (echogenicity index) proposed by Školoudik et al. (2014) was as well tested and compared with this approach.

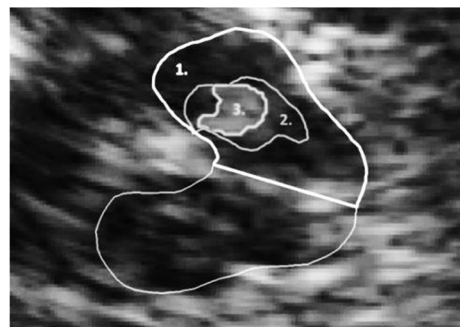


**Fig. 3.13** An illustration of regions used for the quantitative estimation of echogenicity: 1. the extracted  $\frac{1}{2}$  ROI (subsection 3.2.1), 2. the RROI region (see subsection 3.3.2), 3. the extracted SN region (see subsection 3.3.1)

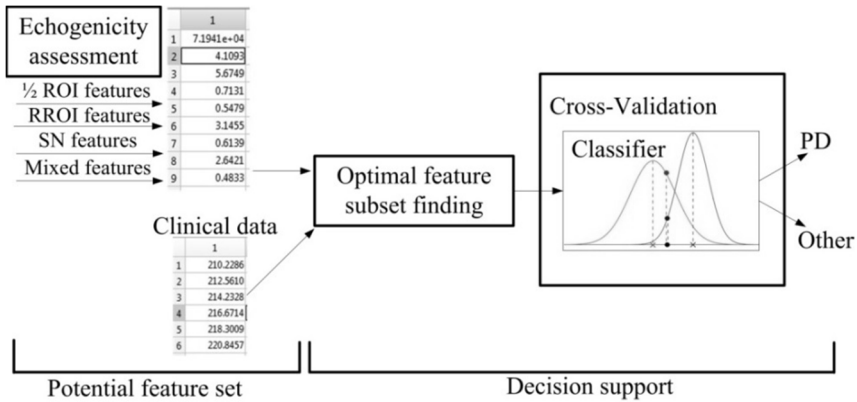


**Fig. 3.14** The expanded block diagram of the system part used for the echogenicity assessment

The SN and RROI features (Otsu criterion, Aspect ratio, Circularity, entropy etc. see Table 3.3 and Appendix 1.) were estimated expecting to improve the hyperechogenicity recognition accuracy by using the extracted local TCS image features.

**Finding the optimal feature subset.** The optimal subset of features giving the best separation was established by using a sequential feature selection method (SFS). The goal of SFS is to find such subset of features in the primary set that optimizes an objective function (Jain et al., 2000):

$$\begin{bmatrix} x_1 \\ x_2 \\ \dots \\ x_N \end{bmatrix} \xrightarrow{\text{Objective function}} \begin{bmatrix} x_1 \\ x_2 \\ \dots \\ x_M \end{bmatrix}, \quad (44)$$

where  $x$  – feature,  $N$  – number of features in primary set,  $M$  – number of selected features in a subset,  $M < N$ . In the particular case, the feature subset giving minimum misclassification error ( $MCE=1-CR$ ) was determined. SFS function is embedded in MATLAB Statistics and Machine Learning toolbox. Moreover, the feature selection procedure was carried out with an assistance of decision support system developed and investigated by Špečkauskienė (2011). The similar subsets of features were established.

**Cross-validation.** 10-fold cross-validation was applied for the estimation of the PD (hyperechogenicity) recognition performance. The cross-validation is used with an aim to estimate the non-biased performance of the classifier. In  $K$ -foold cross-validation, the full dataset (features and diagnoses) are splitted into  $K$  subsets. The train-test cycle is repeated  $K$  times using  $i$  and  $i-1$  subsets ( $i = 1 \dots K$ ) for training and testing, respectively (Refaeilzadeh et al., 2009). Each example in a primary set is used in testing once and  $K-1$  times in a training procedure. Then, the averaged results ( $Se$ ,  $Sp$  and  $CR$ ) are taken. The cross-validation helps to avoid the errors,

which occur if the training data set is non-representational and does not cover the model.

**Table 3.3** Quantitative features used for the echogenicity estimation\*

REGION	1. $\frac{1}{2}$ ROI	2. RROI	3. SN
FEATURES	<ol style="list-style-type: none"> <li>1. Area</li> <li>2. Skewness</li> <li>3. Kurtosis</li> <li>4. Entropy</li> <li>5. Moment of Inertia (MoI)</li> <li>6. 1<sup>st</sup> Hu moment invariant</li> <li>7. EI (Školoudik et al., 2014)</li> <li>8. Mean intensity</li> <li>9. Length of EI curve</li> </ol>	<ol style="list-style-type: none"> <li>1. Otsu criterion</li> <li>2. Aspect Ratio</li> <li>3. RROI entropy</li> <li>4. Area</li> <li>5. Circularity</li> <li>6. Perimeter</li> <li>7. EI</li> <li>8. Mean Intensity</li> <li>9. Length of EI curve</li> </ol>	<ol style="list-style-type: none"> <li>1. Area</li> <li>2. Circularity</li> <li>3. Perimeter</li> <li>4. Entropy</li> </ol>
	<b>Mixed features</b>		
	<ol style="list-style-type: none"> <li>1. Ratio of mean intensities in RROI / <math>\frac{1}{2}</math>ROI</li> <li>2. Contrast: mean intensities ROI/Surroundings</li> <li>3. Areas Ratio SN / RROI</li> <li>4. Areas Ratio SN / <math>\frac{1}{2}</math>ROI</li> <li>5. Areas Ratio RROI / <math>\frac{1}{2}</math>ROI</li> <li>6. Entropy Ratio RROI / <math>\frac{1}{2}</math>ROI</li> <li>7. SN area with a RROI constraint</li> </ol>		

\* – the features presented in the Table 3.3 are defined explicitly in the Appendix 1.

**Classifier.** The previously presented classifier, based on the Mahalanobis distance estimation (see formulas 39, 40 in section 3.3.1.) was used in the experiments.

### 3.5. Conclusions of the 3<sup>rd</sup> chapter.

1. The method for suppression of speckle noise was developed. The improvement is achieved by using the multiple scanning planes (additional information), thus avoiding the need of prior assumptions (tunable parameters) about the SNR. Furthermore, the averaging of the frames decorrelated with a sense of the speckle preserves texture of the images; meanwhile, most of the despeckling algorithms proposed by other authors use a simple image smoothing by skipping the edges, detected by applying certain criteria.
2. The automated segmentation algorithms for the midbrain region (ROI), SN region and localized intra-mesencephalic (RROI) regions were developed. In all the approaches, the empirical data were employed, thus combining the information provided by ultrasonic B-scan image and accumulated experience of the professional neurosonographer.
3. Pilot study and the findings in the literature had demonstrated that  $\frac{1}{2}$  ROI region is relatively a coarse for the estimation and recognition of abnormal/normal SN region. Respectively, the features for more localized evaluation of echogenicity were proposed by incorporating SN and RROI extraction algorithms.

## 4. EXPERIMENTAL INVESTIGATION AND RESULTS

This chapter presents the experimental results obtained by testing algorithms presented above. The clinical (empirical) data used for the efficiency evaluation in the most of the experiments are briefly introduced. The subsections presenting the results are arranged with respect to the third chapter.

### 4.1. Results of multiplanar noise suppression in TCS images

**Experimental data.** The video material was acquired using 2D cine scanning mode, which is available in all the ultrasound scanners of the current generation. The sequences of the TCS images of all subjects were obtained in AVI format. Each sequence consisted of approximately 200 frames ( $600 \times 800$  pixels). All the obtained images and the video material were stored, enabling further investigations off-line. The frame acquisition rate was 51 Hz; thus, approximately 4 s of scanning was recorded. In total, 40 TCS video sequences were selected for the analysis. All the video material was evaluated visually before the processing.

**Performance evaluation.** For the evaluation of the benefit caused by the averaging procedure, CNR ratio and the SNR were calculated (Finn et al., 2011). The CNR parameter shows the contrast level between the ROI and background:

$$CNR = \frac{|\mu_{ROI} - \mu_{BGR}|}{\sqrt{\sigma_{ROI}^2 + \sigma_{BGR}^2}}, \quad (45)$$

where  $\mu_{ROI}$  and  $\sigma_{ROI}^2$  are the mean and variance of pixel intensities in a region of interest, and  $\mu_{BGR}$  and  $\sigma_{BGR}^2$  are the mean and variance of pixel intensities in a region in the image background. SNR was calculated as:

$$SNR = \frac{\mu_{ROI}}{\sigma_{ROI}}, \quad (46)$$

where  $\sigma_{ROI}$  is the standard deviation of the pixel intensities in the ROI. ROI, a rectangular area, was manually selected outlining a high reflectivity region in the TCS image for the evaluation of SNR and CNR. As a reference, the background region of the lower echogenicity (the area of CSF near the skull bone) was chosen. The area of the manually outlined reference region was selected comparable with the size of the ROI. An example of the regions used for the SNR and CNR estimation is presented in subsection 3.1. (see Fig. 3.3 A).

**Results.** The pre-processing was applied on the TCS image sequences of 40 subjects. The averaged SNR and CNR parameters obtained by comparing raw images (UP) and averaging only preselected frames (SFA) are presented in Fig. 4.1 (A). In order to demonstrate the profit of frames selection (removal of correlated frames) procedure, the TCS image sequences containing all the frames were as well averaged (FA) after the mismatch compensation. It could be summarized that the quality of the TCS images was increased from the point of view of SNR and CNR. The increment of SNR and CNR was obtained in all 40 cases, even when all the

sequence was averaged, and this difference was statistically significant (FA: SNR:  $p = 0.017$ , CNR:  $p = 0.005$ ). The rejection of the correlated frames from the sequences marginally improved the results. However, it should be mentioned that it is complicated to demonstrate a relative profit, because in several sequences, few frames were removed; meanwhile, there were sequences where only  $\sim 15\%$  (range 20-40) frames left after the image preselection procedure. In general, the improvement level is directly dependent on the data acquisition circumstances, particularly related to the probe movement magnitude during the scanning. The data were collected during the routine clinical procedures (without any prior about further processing); therefore, the majority of the frames were highly correlated. A comparison of raw TCS image and the image after the pre-processing (FA) is presented in Fig. 4.1 (C and D). It could be noticed that the contrast inside the mesencephalon, especially SN/surroundings, was a bit increased.

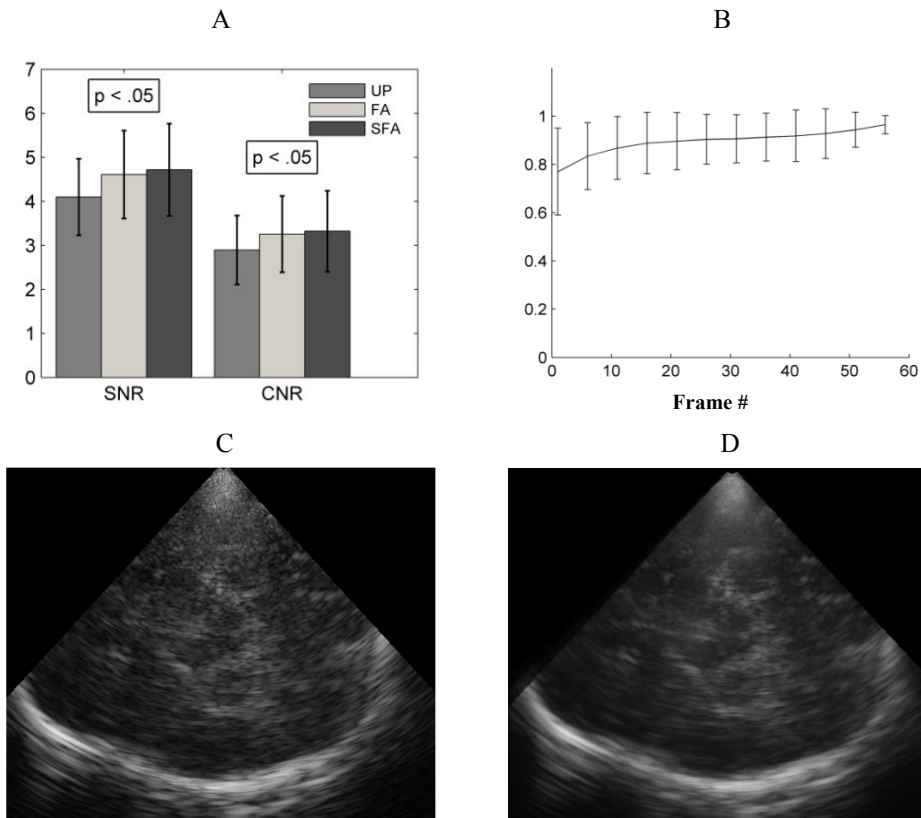


**Fig. 4.1** Results of the TCS image denoising using multiplanar B-scans: (A) a comparison of the averaged SNR and CNR values (40 cases) before processing (UP), applying frame averaging (FA), averaging only preselected frames (SFA); (B) the relationship between averaged normalized SNR together with a number of the averaged frames (mean  $\pm$  SD of 23 analysed sequences, having at least 60 frames); (C) an example of raw TCS image; (D) the same TCS image after FA

The progress (saturation) of averaging was investigated. The number of averaged frames for each case was different and varied from 25 up to 120 in this study. Only the sequences having at least 60 frames for averaging were chosen for the analysis (in total 23). The relation between the number of averaged frames and SNR was determined. Figure 4.1 demonstrates the averaged results of the relationship between the normalized SNR and the number of integrated frames. It should be noted that this dependence is non-linear and exponentially rising. The criterion to stop averaging could be determined by observing the changes of SNR if the computational costs are important (e.g. 30 frames ensures 15% SNR increment; meanwhile, the additional 30 gives only ~5% benefit), but in this approach, the aim was to improve the image quality as much as possible by averaging all the frames, which satisfied the selected frame quality criteria.

In the next research stage, the relations between FtF displacement magnitude, which is directly related to the movements of a scanning probe, and FtF correlation relations in a frame sequence were investigated. An analysis of one case is presented in Fig. 4.2. It was expected to find the answer what minimal FtF shift should be performed in order to achieve FtF decorrelation. Since in the most of the cases, the FtF orientation changes have been marginal, it was assumed as negligible, and only the shift estimated via Euclidean distance  $\|\delta\|$  was used for relative movement estimation. The relationship between the normalized correlation coefficient was obtained by comparing the reference with the rest frames in a sequence, and FtR shift of a single case is presented in Figure 4.2 (A and B). The reference frame used in averaging procedure for alignment is at 3.2 s time instance. Correlations were estimated by analysing the region of the lower echogenicity used for the CNR and SNR assessment. As it could be expected, the correlation coefficient is higher and closer to the reference frame (values between 2.8-3.5 s exceeds 0.8). These findings demonstrate that the interference conditions are not altered in the neighbouring frames of the echo-poor region. Observing the changes in Fig 4.2 (A) and (B), it could be noticed that (especially in a range 1-2 s)  $r_{FtR}$  and  $\|\delta_{FtR}\|$  are inversely related, and magnitude of the shift indicates that FtR decorrelation is achieved when  $\|\delta_{FtR}\| > 1.5$  mm. A relative change of  $r_{FtF}$  and  $\|\delta_{FtF}\|$  is presented in Fig 4.2 (C) and (D). These dependencies show that the frame decorrelation is achieved if  $\|\delta_{FtF}\| > 1.5$  mm ( $r_{FtF} < 0.6$ ). Moreover, it should be noticed that in most of the cases the correlation in a neighbourhood is very strong, and this indicates that the acquisition frame rate (51 Hz) is too high with respect to the slow continuous hand-hold probe movements, and the frames preselection procedure is desirable.

**Discussion.** In order to improve the TCS image quality, the modified frame averaging technique for the suppression of the noise was proposed. The calculated SNR and CNR parameters showed that the benefit by pre-processing was achieved in all the cases, and these changes were statistically significant. There is no doubt that the quality of diagnostic image was improved even evaluating visually. It was found that the majority of the frames in a sequence are strongly correlated, since the data acquisition rate is comparatively high to compare with a velocity of the hand during the scanning. The frame preselection criterion was defined. It was shown that

FtF shift of  $\|\delta_{FtF}\| > 1.5$  mm of the scanning plane distorts the coherence ( $r_{FtF} < 0.6$ ). Such threshold could be used as a criteria for suitable frame preselection, since the wavelength (frequency compound) or the aspect angle (spatial compound) are the scanning conditions that have to be altered in order to achieve the speckle decorrelation. The external position and orientation tracking sensor could be used for the FtF shift estimation and quasi real-time approach could be developed for the speckle suppression.

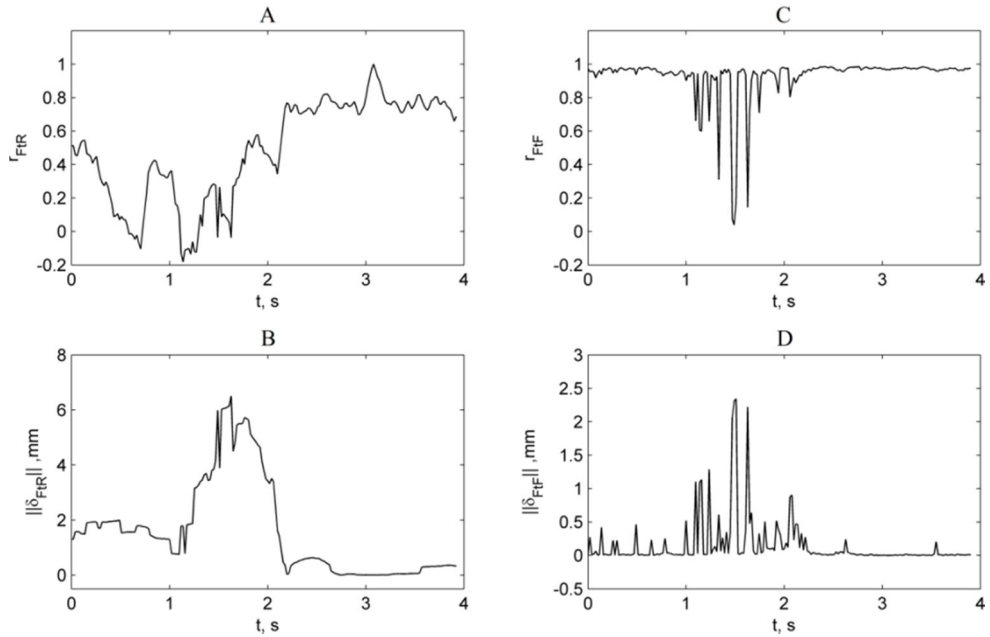


**Fig. 4.2** Frames sequence spatial intra-displacement (dependent on the movements of the probe) relationships with correlations (FtR and FtF) in the region of lower echogenicity (an example of single sequence): subfigures (A) and (C) presents the relationships between the frame acquisition time instances (or frame number, in total 201 frames acquired at 51 Hz) and (A) FtR correlation coefficient, (B) FtR shift, (C) FtF correlation coefficient, (D) FtF shift

It was investigated how the pre-processing influences the results of midbrain region segmentation, the main results are presented in the following subsection.

## 4.2. Experimental results of the midbrain segmentation

**Experimental data.** 130 TCS images were used in the development of PSSM based midbrain segmentation method. All the images were recorded and delineated by a professional neurosonographer, 40 of them were marked by a second expert radiologist off-line. Respectively, 90 midbrain contours were used for the statistical shape model construction, rest 40, evaluated by two experts, were used for the validation of the method. In total, 92 subjects were scanned (58 cases with single B-scan per subject, and 34 subjects had two scan planes acquired at the different levels of the brainstem). 53.26% of the subjects had a clinical PD diagnosis (49),

other (43) healthy controls. The Kolmogorov-Smirnov normality (K-S test) test was applied in order to estimate if the model accounts for the variability of anatomy and image quality. At first, the distribution of midbrain areas in the dataset was analysed. It was found that the sample comes from the standard normal distribution in both the training and test groups, thus demonstrating the sufficient variety in sizes. The huge number of eigenvalues demonstrates the variety of shapes (see below **Setting of the algorithm parameters**, 16 eigenvalues ensures 98% of total shape variation in the training set; meanwhile, the number of eigenvalues for the trivial shapes is from 4 up to 6 in personal experience).

**Performance evaluation.** The manual experts delineations served as the reference for the evaluation in this study. The features of transcranial image are strongly related to the properties (thickness and homogeneity) of the temporal bone. Respectively, it is complex to create adequate simulated images or to manufacture brain tissue mimicking ultrasonic phantoms. It is complex and very expensive to manufacture the adequate phantom having the skull bone mimicking the layer (aberrator) with variable and controllable acoustic properties. At first, the *SoS* and attenuation range in the temporal bone should be determined in a large scale study. The experience and findings in other published works show that comparatively huge differences are found between the measured *SoS* and attenuation. There is the possibility to simulate the TCS image, but the knowledge about the above mentioned acoustic properties is as well mandatory. It is believed that the using of empirical data (real diagnostic images) would be more efficient and reliable way for the development and testing of algorithm. The magnetic resonance imaging is rarely applied for the PD patients. Therefore, in this case, it was only an available reference for the assessment of segmentation quality. The quality was evaluated by using four different features. The contour obtained by proposed method was compared to the manual delineations by 1) root mean squared error (*RMSE*), 2) Hausdorff distance (*HD*), 3) *DICE* coefficient, and 4) Bland Altman plot. *RMSE* between the contours is defined as:

$$RMSE(\mathbf{g}, \mathbf{k}) = \sqrt{\frac{1}{n} \sum_{i=1}^n (g_i - k_i)^2}, \quad (47)$$

where  $\mathbf{g} = (x_1, \dots, x_n, y_1, \dots, y_n)^T$  coordinate vector of the contour obtained by using the proposed method,  $\mathbf{k} = (x_1, \dots, x_n, y_1, \dots, y_n)^T$  coordinate vector of contour outlined by an expert, both with  $n$  points. The Hausdorff distance between  $\mathbf{g}$  and  $\mathbf{k}$  is given as:

$$HD(\mathbf{g}, \mathbf{k}) = \max \{h(\mathbf{g}, \mathbf{k}), h(\mathbf{k}, \mathbf{g})\}, \quad (48)$$

where  $h(\mathbf{g}, \mathbf{k})$  directed Hausdorff distance:

$$h(\mathbf{g}, \mathbf{k}) = \max_{i \in \{1, \dots, n\}} \left\{ \min_{j \in \{1, \dots, n\}} \|g_i - k_j\| \right\}, \quad (49)$$

Dice coefficient shows spatial overlap between the areas extracted manually ( $\mathbf{k}$ ) and by PSSM based method ( $\mathbf{g}$ ):

$$DICE = \frac{2 \cdot |\mathbf{g} \cap \mathbf{k}|}{|\mathbf{g}| + |\mathbf{k}|}. \quad (50)$$

Bland-Altman analysis was applied with the aim to compare the evaluated sizes of the midbrain area. In order to demonstrate the superiority of local phase based detection strategy, the statistical shape model was as well combined with an amplitude-intensity based edge detector. First, the order derivatives of intensity projections were used as an edge detector assuming that the maximal value indicates a plausible midbrain boundary point. The first version of the midbrain segmentation algorithm on the basis of AC was as well investigated and analysed in the same fashion.

**Setting of the algorithm parameters.** Parameters of the method are presented and discussed in this subsection. The number of eigenvalues was selected introducing the constraint:  $\Sigma \Lambda_i \geq 0.98$ , where  $i = 1 \dots K$ . The limit ensures that 98% of variance (in this case  $K = 16$ ) is controlled by the model. Number of points in the model was as well selected experimentally  $n = 150$ . These values were adjusted visually by evaluating the results of segmentation. It was observed that the optimal balance between the contours rigidity and the ability to adapt to concave boundaries is obtained when  $\Sigma \Lambda_i \geq 0.98$  and  $n = 150$ . The optimization constraints for scale, shift, rotation and shape transform was adjusted as follows:  $s_x, s_y = 0.8 - 1.2$ ,  $\Theta = \pm \pi/8$ ,  $x_t, y_t = \pm 12.5$  mm,  $b_i < \pm 4\sqrt{\lambda_i}$ . Such ranges guarantee the generation of spatially variable realistic shape. The parameters of the log-Gabor filter were adjusted as follows: the bandwidth of a filter  $\kappa/\omega_0 = 0.75$  (1 octave), the fundamental frequency of a filter at first scale  $\omega_0 = 0.2$  1/pixel, decrement of  $\omega_0$  from scale up to scale 5%. Length of intensity projections and the number of log-Gabor filter scales were determined by using the empirical training data (contours used for the SSM construction). The relationship between the averaged *RMSE* vs number of filtering scales and length of intensity projections  $q$  were investigated. The relationship is presented in Figure 4.3. Summarizing the results, it was established that the optimal number of scales is 40, length of intensity projections  $q_{opt} = 7$  mm.

**Results.** The averaged quantitative results obtained by performing segmentation of testing data set (40 cases) are presented in Table 4.1. The extracted contours were compared to the delineations of both experts by using metrics presented above and estimating the mean difference of estimated areas of the midbrain. Moreover, the variability between the experts was estimated by using the same metrics. The comparison of experts' evaluations revealed that the accuracy of the semi-automated segmentation is in the same order to the variation seen across the manual segmentations demonstrating that the method is comparable to the manual evaluation. The model was constructed by using the delineations of the first expert who acquired the images. Therefore, the adequacy between the first expert and the

method was noticeably better. The proposed method is directly comparable to the method presented in the earlier study based on AC. PSSM method clearly outperforms the previously presented technique, since HD was close to 6 mm in that case (see Table 4.1 5-6 rows). The results obtained by comparing the plausible midbrain boundary point detector based on local phase (1 and 2 rows) and the method based on amplitude-intensity (3 and 4 rows) showed that the SSM segmentation based on local phase outperforms the based on the amplitude, because the variance between the experts evaluated midbrain areas and the areas extracted automatically was lower in case of PSSM. An illustration of the result of PSSM based segmentation is presented in Figure 4.4 B. The extracted contour compared to the manual delineation of neurosonologist is shown in Figure 4.4 C. A comparison of the contours obtained by PSSM and ASSM is presented in Figure 4.4 D.

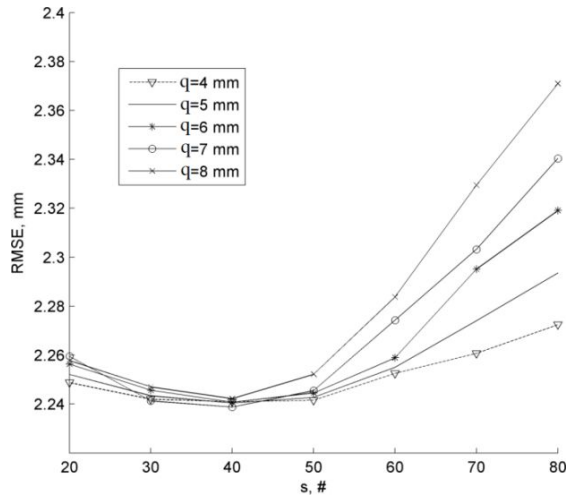


**Fig. 4.3** The relationship between the averaged RMSE and number of selected filter scales, when  $q = 4:8$  mm.

**Table 4.1** The quantitative averaged results of the midbrain segmentation

Measure \ VS	RMSE, mm		HD, mm		DICE, %		Area difference, cm <sup>2</sup>		
	Mean	SD	Mean	SD	Mean	SD	Mean	SD	<i>p</i>
PSSM vs. EX1	1.99	0.61	3.60	1.37	88.47	3.65	0.02	0.71	0.87
PSSM vs. EX2	2.29	0.73	3.82	1.24	87.63	3.59	0.06	0.52	0.66
ASSM vs. EX1	2.03	0.60	3.86	1.25	88.40	3.56	0.07	0.72	0.61
ASSM vs. EX2	2.29	0.73	3.92	1.28	88.28	3.28	0.14	0.53	0.32
AC vs. EX1	2.92	0.98	6.09	1.97	81.98	6.50	0.56	1.12	0.003
AC vs. EX2	2.84	0.81	5.74	2.00	82.05	5.46	0.97	1.06	0.001
EX1 vs. EX2	2.20	0.74	4.29	1.82	89.61	3.43	0.42	0.59	0.13

PSSM – shape model combined with target points detector based on the the phase congruence, ASSM – shape model combined with target points detector based on the amplitude (first order derivative), EX1 – manual delineation of the first expert (neurologist), EX2 – manual delineation of the second expert (radiologist), AC – method based on active contour (Sakalauskas et al., 2013), SD – standard deviation.

The results of the Bland-Altman analysis of the data are presented in Figure 4.5. The method was compared to the manual evaluations of the experts. The obtained mean

differences (vs. EX1: 0.02 cm<sup>2</sup>, vs. EX2: 0.06 cm<sup>2</sup>) indicates that the method is comparable to the manual expert evaluation and that there is no systematic error introduced by the method. The applied paired *t*-test showed that the differences between the manually evaluated midbrain areas and areas estimated by proposed method are insignificant (EX1: *p* = 0.87, EX2: *p* = 0.66). It is difficult to judge the achieved results from the point of view of clinical significance, because the extraction of the mesencephalon is only the step in the accurate and precise sonographic assessment, but the errors in each stage influences the final result. Therefore, the accuracy of mesencephalon segmentation is especially important, since each  $\mu\text{m}$  is very valuable for the further assessment and analysis of the intramesencephalic brain structures in the TCS images.

The obtained DICE coefficient values are slightly lower (DICE:  $\sim 90\%$ ) in the comparison to the results presented by the single existing 2D midbrain segmentation algorithm introduced by Engel and Toennies (2009), but it is considerably faster and has relatively low-complexity. Furthermore, the segmentation results are comparable to the results achievable when segmenting the left ventricle in the echocardiography (Belaid et al., 2011) or prostate region in the transrectal ultrasound images (Yan P., et al., 2011) by the methods presented in the contemporary scientific literature. DICE coefficient  $89.91 \pm 6.01\%$  and  $91.00 \pm 3.00\%$  were reported by the authors. The echocardiographic and transrectal images have a better spatial resolution, and the segmented objects are much larger.

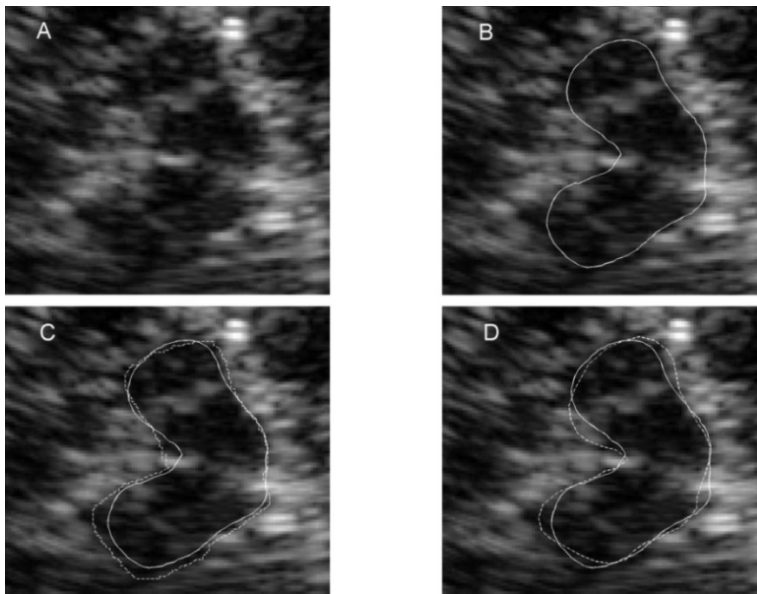


**Fig. 4.4** Results of segmentation of the midbrain (example): (A) TCS image example, (B) contour obtained by the proposed method (PSSM), (C) comparison of the extracted contour (solid line) and manual delineation (EX1, dashed line, quantitative results of the presented case: RMSE = 1.84 mm, HD = 3.43 mm, DICE = 89%), (D) comparison of contours obtained by PSSM (solid line) and ASSM (dashed line)

The approximate time of segmentation having a trained model is  $1.41 \pm 0.17$ s automatic part plus the duration of the experience dependent initialization 5-20 s. All the computation was conducted on an Intel(R) Core i7, 2.93 GHz PC by using MATLAB (Mathworks, USA) software.

It was observed how the multiplanar noise suppression affects the results of the midbrain segmentation. The evaluation was performed in two ways: subjective and objective. Firstly, the initialization of PSSM was performed separately in both groups (raw and averaged TCS images) expecting that it is easier to recognize the region and place the contour. In the second stage, the same initialization was used for the segmentation of the midbrain in raw and averaged images.

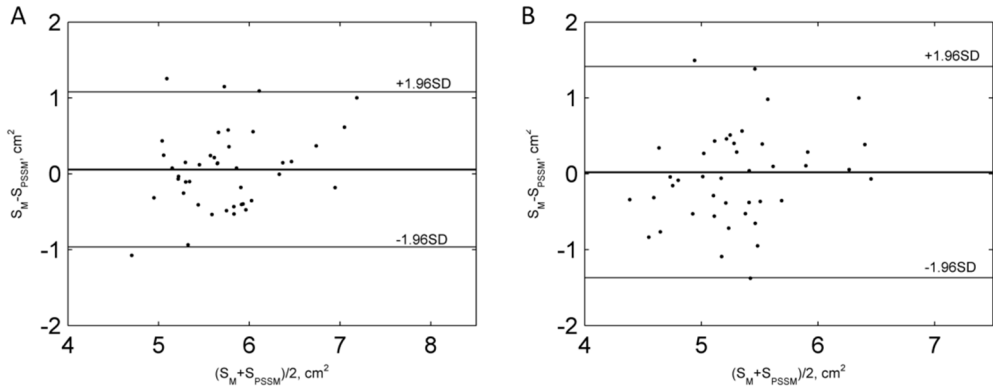


**Fig. 4.5** Bland-Altman plot of the differences of the midbrain areas: (A) EX1 vs. PSSM; (B) EX2 vs. PSSM

Table 4.2 presents the results of the investigation. The extracted contours were compared by using *RMSE*. *RMSE* was used, since it is sensitive comparing the subtle differences between the contours. It could be summarized that the averaging improved the results of segmentation in subjective cases. Meanwhile, in the objective case, the adequacy was close to the same. This indicates that the acoustic interference noise is not a decisive factor in identifying the boundaries of the midbrain in the images, but the quality of the image was improved from the point of view of SNR, and this helps to identify the midbrain visually. Furthermore, the noise suppression is especially important for the detection and analysis of inter-mesencephalic structures, since the amplitude values are substantially lower there.

**Table 4.2** Results of the midbrain segmentation using raw and averaged TCS images

		RMSE, mm			RMSE, mm
Subjective	1EX & R	$2.16 \pm 0.67$	Objective		$1.97 \pm 0.58$
	2EX & R	$2.36 \pm 0.71$			$2.18 \pm 0.58$
	1EX & A	$2.07 \pm 0.55$			$1.97 \pm 0.58$
	2EX & A	$2.34 \pm 0.69$			$2.17 \pm 0.59$

R – raw, A – averaged, EX1 – manual delineation of the first expert (neurologist), EX2 – manual delineation of the second expert (radiologist).

It was investigated how the initialization affects the segmentation results, since the initial shape for PSSM segmentation is placed manually. The same operator performed the initialization for 5 randomly selected TCS images 15 times (with 10 minute interval between each iteration). PSSM based segmentation was performed, and the adequacy between the segmentations and manual delineations of more experienced expert were determined. The relatively small spread of DICE coefficient ( $SD < \pm 2\%$  for all the cases) demonstrates that only a marginal error could be introduced. The results of the investigation are presented in Figure 4.6.

Moreover, one operator without any experience was involved in the segmentation of TCS images. First, the observer was briefly introduced with the anatomy of the brain, and few manually outlined ultrasonic images were demonstrated before the experiment. Ten TCS images were randomly preselected, and PSSM segmentation was performed by the experienced operator and the novice. The obtained contours were compared to the manual delineations made by the two experts. The averaged results are presented in Table 4.3. The results revealed that the proposed segmentation algorithm is experience-undemanding. The differences of segmented regions were comparable between the experienced operator and beginner and even slightly better compared to the contours outlined by one of the experts. Furthermore, the SD values are lower comparing the segmentations of the two operators to compare with the two experts (see Table 4.1):  $DICE \pm 3.43\%$ ,  $HD \pm 1.82$  mm for the experts; meanwhile, the spread between the operators  $\pm 2.32\%$  and  $\pm 0.89$  mm, respectively. This shows the possibility of lowered uncertainty (observer's variability) of the estimations.

**Discussion.** Novel and efficient technique for the midbrain segmentation in TCS images was developed. The combination of experience based on the shape model and intensity-amplitude invariant edge detector was applied for the extraction of fuzzy boundaries of the midbrain in TCS images.

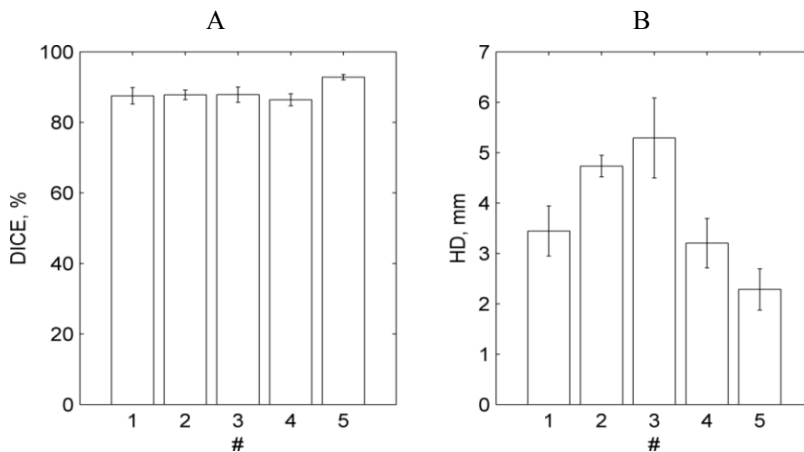


**Fig. 4.6** Investigation of the influence of manual initialization to the results of segmentation: average DICE and HD values together with the standard deviation (SD) in 5 randomly selected cases (#)

The applied shape constraints (robustness) of the model ensures that the contour will converge to the boundary even if part of the plausible midbrain boundary points will be detected inaccurately in cases when no positive edge is expressed in the analysed intensity projection.

**Table 4.3** Results of the investigation comparing the segmentations made by the two operators

VS \ Measure	HD, mm		DICE, %	
	Mean	SD	Mean	SD
1 vs. EX1	3.45	0.67	89.56	1.67
2 vs. EX1	3.44	1.14	90.33	3.39
1 vs. EX2	3.68	1.03	88.22	3.93
2 vs. EX2	3.74	0.90	87.78	3.56
1 vs. 2	3.15	0.89	91.11	2.32

1 – experienced operator, 2 – novice.

The phase based detection has an advantage when the signal amplitude level is low and comparable to the noise amplitude level regarding the invariance to the intensity and contrast changes, because the local phase based on the detector always finds the edge, which is formed at the location where the phase varies least. This feature makes the method less sensitive to the examiner-predefined gain and TGC curve parameters of the ultrasound scanner. The presented empirical scheme for selecting optimal local phase parameters could be used for the algorithm calibration by applying the method for processing of images obtained by the other ultrasound machines.

The visual evaluation of particular typical cases of the extracted contours showed that, in the worst cases, the image quality was extremely low. Figure 4.7 presents the example of discrepant segmentation. It could be summarized that it is difficult to outline the midbrain even manually in some cases. A part of the tested images could be admitted as unprocessable.

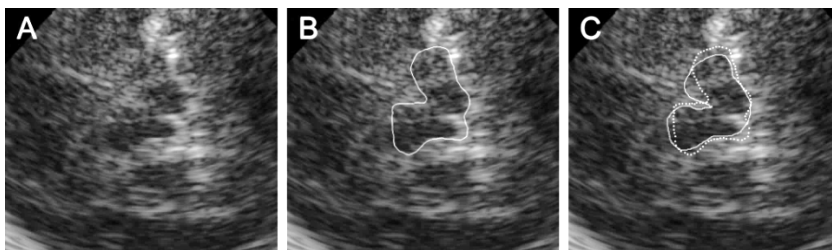


**Fig. 4.7** An illustration of discrepant segmentation: (A) fuzzy TCS image, (B) the results of segmentation by PSSM, (C) comparison EX2 vs. PSSM (PSSM – pointed line, EX2 – solid line, DICE = 84.25%, RMSE = 2.79 mm, HD = 4.92 mm)

An image quality criterion is needed to be ensured that the acquired images are suitable for the further computer assisted analysis. A considerable inter-observer and

intra-observer variability in case of TCS was found in the previous research (see subsection 2.2); hence, there is a lack of gold standard for the evaluation of segmentation quality. The main limitation of this study is that the method was trained by using the delineations by one neurosonographer. Indeed, the transcranial ultrasonic examination is a relatively new technique finding its place and value in a routine clinical diagnostics, and there are not many experienced neurosonographers. There is the only one experienced expert of TCS in Lithuania so far (Kristina Laučkaitė, since 2010). The transcranial ultrasonic examination was recently recognized as a valuable imaging tool for screening (Laučkaitė et al., 2012), diagnosis and differential diagnosis of PD. TCS was involved in the recommendations by the European Federation of Neurological Society as an approved diagnostics technique for the early diagnosis and differentiation for PD in 2013 (Berardelli et al., 2013). The shape model can be easily updated by including the delineations of other experts. Moreover, new cases having an irregular shape could be included, thus increasing the versatility of the model. There is an option to construct a statistical shape model by using the magnetic resonance data, since the midbrain segmentation in MRI is not so complicated, but the presentable data set is needed. The shape model will be updated by the delineations of other neurosonographers in further studies expecting to reduce the inter- and intra-observer variability and guarantee the accurate localized intra-mesencephalic midbrain echogenicity analysis and characterization by the means of digital image processing.

### 4.3. The performance of the SN extraction algorithm

**Experimental data.** In total, 75 manually annotated TCS images were used for the training of the SN extraction algorithm. At first, 15 cases were excluded from the study as clearly unrepresentable examples (75/90 left) after the visual evaluation. As it was mentioned before, there are plenty of cases where not all manually outlined SN pixels have a relatively larger intensity and intensity gradient at the boundary, and the most doubtful cases were excluded from the training data set. The images of PD affected subjects and healthy controls were mixed (proportion was 44/31, respectively). Meanwhile, 40 images outlined by two experts (the same cases used in 4.2 subsection) were used for the evaluation (20 subjects with a clinical PD diagnosis / 20 healthy controls).

**Performance evaluation.** The extracted areas were compared by using DICE coefficient. The  $Se$  and  $Sp$  estimates were as well used.  $Se$  is the ratio of correctly identified positives ( $TP$ ) from all the positive results:

$$Se = \frac{TP}{(TP + FN)} \cdot 100\%, \quad (51)$$

in the particular case, the  $TP$  – true positives, correctly identified SN area pixels ( $\Omega_2$  – class),  $FN$  – false negative, pixels incorrectly assigned to  $\Omega_1$  class. The specificity ( $Sp$ ) is the ratio of correctly identified negatives ( $TN$ ) from all the negative results:

$$Sp = \frac{TN}{(FP + TN)} \cdot 100\%, \quad (52)$$

where  $TN$  – number of pixels correctly assigned to  $\Omega_1$  class,  $FP$  – pixels incorrectly assigned to the SN class. In some cases, the classifier based approach extracts more than single one connected region, and none of the contour based estimates ( $RMSE$ ,  $HD$ ) was used for the segmentation quality assessment. Bland-Altman analysis was as well performed, and the Spearman correlation coefficient ( $r$ ) between the manually and automatically estimated areas was calculated.

**Results.** Quantitative results of all 40 analysed cases are presented in Table 4.4. The obtained correlation between the manual and automated approaches was moderate ( $r > 0.5$ , see 2 row) but statistically significant. High  $Se$  and relatively low  $Sp$  values indicates that the largest errors occur due to the false pixels assigned to the SN class (FP). It has to be noticed that typical  $\frac{1}{2}$  ROI region have from 800 up to 1200 pixels candidates, and only from 60 up to 200 of them belong to the SN class.

**Table 4.4** Results of the SN area extraction

	1 expert	2 expert
DICE (mean $\pm$ SD), %	64.11 $\pm$ 8.97	65.46 $\pm$ 8.94
$r$ ( $p$ -value)	0.51 ( $p < 0.05$ )	0.53 ( $p < 0.05$ )
$Se$ (mean $\pm$ SD), %	95.05 $\pm$ 2.23	94.25 $\pm$ 2.76
$Sp$ (mean $\pm$ SD), %	63.41 $\pm$ 14.69	67.88 $\pm$ 13.92

SD – standard deviation,  $p$ -value – the measure of statistical significance obtained by  $t$ -test.

The results of Bland-Altman analysis are presented in Fig. 4.8 (A) and (B).

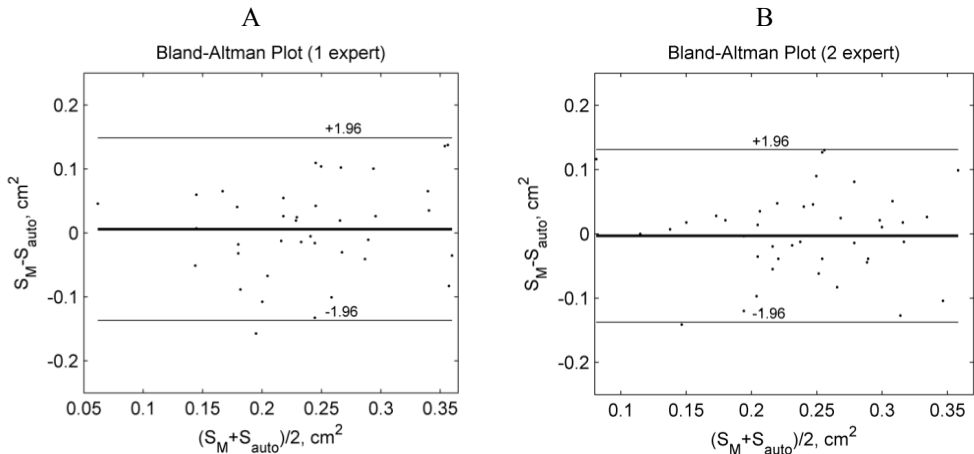


**Fig. 4.8** Bland-Altman analysis of automated SN area evaluation: (A) a comparison of automatically estimated SN area and measurements of the first expert, (B) a comparison of the measurements performed by the second expert

The obtained mean differences (A:  $0.0058 \text{ cm}^2$  and B:  $-0.003 \text{ cm}^2$ ) show that there is no systematic difference between the methods, but relatively considerable spread (A:  $-0.1367 - 0.1484 \text{ cm}^2$ ; B:  $-0.1372 - 0.1311 \text{ cm}^2$ ) indicates that the accuracy of the method is limited, since the limits of the agreement could not be called clinically insignificant to compare with the cut-off SN value  $-0.2 \text{ cm}^2$ . Surprisingly, the errors are a bit raising together with the size of SN. This could be explained by the fact that mixed (PD and control group) data was used for the training of the classifier, and the shift in the mean SN size could be expected.

**Discussion.** The adequacy between the SN area extracted by using the algorithm defined above and the manual delineations was inconclusive. The adequacy of reference was investigated. The evaluations of both experts, having different experiences in the evaluation of TCS images, were compared. The obtained Spearman correlation coefficient was comparable to the values obtained in case of the automated approach ( $r = 0.51$ ,  $p < 0.001$ ). Bland-Altman diagram is presented in Fig. 4.9.

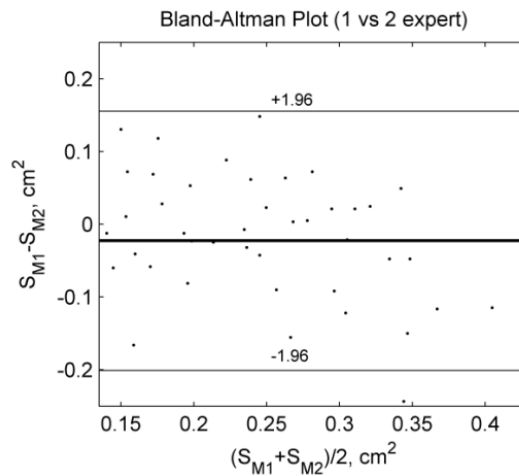


**Fig. 4.9** Bland-Altman analysis of the SN area assessment performed by 2 experts

The differences and spread (mean difference  $-0.0227$ , limits of agreement:  $-0.2009 - 0.1554 \text{ cm}^2$ ) demonstrates the existent variability within the manual evaluations. The higher spread is found in the control group ( $S_{SN} < 0.2 \text{ cm}^2$ ) confirming the fact that it is much more difficult to outline normal SN, since then, the size and contrast is lower. This investigation and the findings of other authors (Školoudik et al., 2007) have shown that considerable experience is mandatory in order to achieve reliable and precise TCS measurements. Figure 4.10 presents the comparison of the manual and automated SN segmentations. In all the cases, the extracted segments look proper enough, but the adequacy is low. The quality of automated segmentation is directly dependent on the accuracy of manual delineations made by the operator, since it is based on learning. The annotations outlined by few experts possibly could improve the results and would be valuable for the preselection of representable cases for the training data set (e.g. selection of

the cases having high adequacy between the evaluations performed by few operators or repetitive assessment of the same neurosonographer).

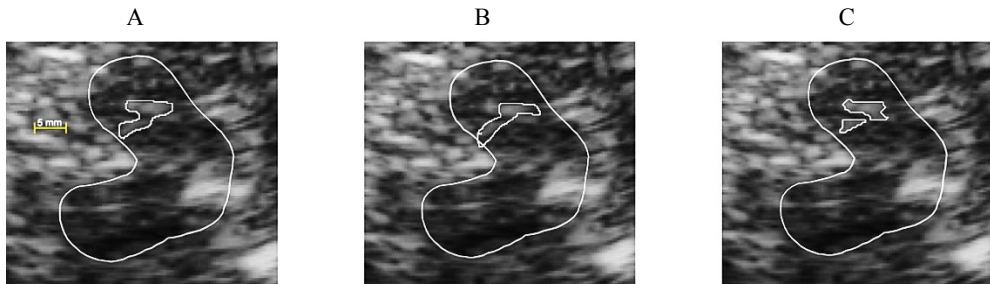


**Fig. 4.10** A comparison of SN contours extracted by: (A) the first expert, (B) the second expert, (C) the proposed algorithm

The proposed method clearly outperforms the technique proposed by Kier et al. (2007), since it is based on the binary conversion that is associated with certain loss of information. The method proposed by Engel and Toennies (2009) performs better; however, as it was mentioned, it is computationally expensive and mathematically complex. A similar probabilistic classifier based strategy was proposed by Pauly for 3D sonographic data. There is no direct comparison between the methods, since Pauly approach operates in 3D. The main differences are the features used for the SN characterization. After all the proposed approaches, is one of the first developed techniques for SN segmentation.

#### 4.4. The results of proposed automated TCS echogenicity analysis system

**Clinical Data.** All the data collected at the LUHS Department of Neurology during the 2011-2014 period was analysed in the final large-scale study. In total, the data of 704 subjects were registered in the collected database (MS Excel format). Table 4.5 presents the main attributes which were recorded. Only the attributes of subjects filled for at least 30% are presented. This filling percentage is directly dependent on the individual strategy of diagnostics.

The majority of subjects registered in the database had the accompanying set of TCS images. The number of scanning planes acquired for each subject varied from 2 to 30 depending on the acoustic permeability of the temporal bone (ITB). For the successful cases, all three planes (with repetitions) were collected bilaterally. Part of the images was stored with manual annotations; therefore, they were inappropriate for the automated analysis. The research was mainly focused on the mesencephalic B-san plane where the main biomarker of PD is found. Respectively, the images of each subject were carefully reviewed and preselected for the further automated analysis. In total, 80/704 subjects had both-sided ITB and 146/704 the appropriate acoustic window unilaterally. Respectively, 624 image sets were left for the further processing, and 146 of them had no choice for the scanning side preselection. Another very important fact is that the part of the PD affected subjects have one-sided hyperechogenicity property. In total, 86/478 bilaterally scanned had determined the unilateral hyperechogenicity. It is enough to have a

hyperechogenicity at least on one side to be PD diagnosed or to have other hyperechogenicity related diagnosis (e.g. ET+PD, or APS). These facts caused the selection of semi-blind methodology for the echogenicity analysis. It was decided to preselect a **single B-scan plane per subject** for the further analysis. The multiple scanning planes of the midbrain undoubtedly provide additional amounts of potential information. However, **the main goal of this work was to investigate the potential of various image features carrying information about size, shape and intensity of the diagnostic regions in the midbrain for the automated PD (hyperechogenicity) recognition purpose.** Therefore, the selection of appropriate sample for the training of the classifier is mandatory.

**Table 4.5** The main attributes recorded in the database

Class	Attributes	Type	Description
Demographic data	Age Gender Duration of the symptoms Lateralization of symptoms Predominant symptoms Stage of the PD	q b q g b g	Years 0-female, 1-male Expressed in years 1-right, 2-left, 3-both sides Tremor, slowness of movement According to Hoehn and Yahr (1967)
Results of clinical TCS examination (manual assessment)	Midbrain area SN area Width of 3 <sup>rd</sup> ventricle Width of lateral ventricles SN echogenicity grade Nucleus raphe grade Substantia grisea centralis grade	q q q q g g b	ROI, SN evaluated bilaterally in the mesencephalic plane (cm <sup>2</sup> ) Fig.1.4 (B,C) planes (cm) Fig.1.4 (B,C) plane (cm) Grade from (0 up to 5) 0-norm, 1-middle, 2-discontinuous 0-normal, 1-hyperintense
Other imaging modalities results	Rarely performed (< 10%) and were not involved in the final-study: <ul style="list-style-type: none"> <li>• SPEC (DaTscan) – 47 subjects;</li> <li>• MRI – 15 subjects;</li> <li>• CT – only quantitative description of the findings.</li> </ul>		
Established clinical diagnosis*	Served as a reference for the evaluation of PD (hyperechogenicity) recognition performance. The subjects were classified into 11 types (685/704 subjects had finally established diagnosis): <ol style="list-style-type: none"> <li>1. PD</li> <li>2. ET</li> <li>3. ET+PD – overlapping PD and ET</li> <li>4. APS – atypical Parkinsonian syndromes (MSA, SP)</li> <li>5. Control group</li> <li>6. SeP – secondary Parkinsonism</li> <li>7. MCI – mild cognitive impairment</li> <li>8. Dementia</li> <li>9. Dystonia</li> <li>10. HDP – hereditary Parkinsonism</li> <li>11. Other</li> </ol>		

\* – Final clinical diagnosis was established considering all the results of the examinations by a decision of the movement disorders expert, q – quantitative attribute, g – grade (rather qualitative), b – binary (0 or 1), Other – subjects with other clearly undefined movement disorders.

The blind testing methodology (using any mesencephalic B-scan plane) would be meaningful only if the valuable and stable features will be determined. The main criteria for plane preselection were (must satisfy as least one):

- *the scanning side (plane) where the operator manually estimated the larger SN size in the PD group (unilateral hyperechogenicity cases). There is no sense to search for hyperechogenicity which is absent;*
- *only the unilateral scans were available due to ITB;*
- *in some cases, it was almost impossible to identify the midbrain region visually. This is an obstacle to extract ROI region, since the semi-automatic approach was proposed. Respectively for these particular cases, the clearest B-scans were selected. Some cases (< 5%) were discarded because none of the collected B-scans were appropriate;*
- *in more than a half of the cases, the operator stored the images with manual annotations made on-line and the same B-scan without markings afterwards. Thus, the plane identified as the best by an operator was used for the further processing.*

A part of the clinical data (see Table 4.5) were as well included in the analysis to serve as a reference for the quality assessment (see Clinical data block in the scheme of the TCS image analysis system in the 3<sup>rd</sup> chapter). The quantitative manually evaluated SN, midbrain sizes (in the side having the maximal SN size), widths of the ventricular system (III and lateral ventricles) and the final clinical diagnoses were involved in the analysis. This caused the final criterion for the preselection of cases (subjects) for the analysis:

- *the subjects satisfying the criteria for the plane preselection, having the manually evaluated parameters (max SN, midbrain, width of the ventricles) and established final clinical diagnoses were appropriate.*

399/704 subjects that satisfied the criteria were found in the database. The content in accordance with the established clinical diagnoses is presented in Table 4.6.

**Table 4.6** Cases appropriate for the automated analysis, according to the clinical diagnosis

Diagnosis code	1	2	3*	4*	5	6	7	8*	9*	10*	11*
##	118	92	16	7	73	34	24	13	8	6	8

\* - the subjects having these diagnoses were removed from the further analysis due to the insufficient number of cases for training and evaluation of the classifier, \*\* - preselected cases having acquired at least one clear mesencephalic B-scan plane, # - number of cases.

Training and testing of the classifier require representable amount of data. Third, fourth and eight-eleventh diagnoses were discarded due to small amount of cases. Finally, the data of 341 subjects were left.

**Performance assessment.** *Se* and *Sp* estimates (see 4.3 formulas 51 and 52) were used for the evaluation. Moreover, the classification ratio was used for the assessment of the hyperchogenicity recognition accuracy:

$$CR = \frac{TP+TN}{TP+TN+FP+FN} \cdot 100\% \quad (53)$$

where *TP* – denotes the subject correctly assigned to the PD class, *TN* – the subject correctly assigned to the other “non-PD class”, *FP* – incorrectly assigned to the PD class, *FN* – incorrectly assigned to the non-PD class.

**Pilot study.** The first trial to classify TCS images into PD/control groups was performed in the year 2011 (Sakalauskas et al., 2011). The manually outlined ½ ROI region was analysed by using the features presented in the subsection 3.4 (Table 3.2). The images of 110 subjects were analysed. Sixty one of them had a clinical PD diagnosis, other 49 were healthy subjects. A single plane per subject was randomly preselected for the analysis ignoring the clinical findings. In order to reduce the dimensionality of the data, the non-informative features were filtered by using the estimate of statistical significance: *t*-test was applied to each feature separately as a measure of feature’s efficiency in separating groups of interest. The features were discarded according to the predefined threshold of *p*-value, which did not have strong power of discrimination (threshold value < 0.1).

**Results of the study.** The obtained classification ratio using only the automatically extracted ½ ROI features, in the best case (78.18%), was lower in comparison to the result which could be achieved by using the size of the SN area as a solely parameter for the classification (85.78%). A higher result (87.27%) was obtained when the manually evaluated size of the SN area was included in a primary set of features. The results of PD recognition are presented in the Table 4.7. The investigation showed that the moment of inertia could be a supplementing parameter and a combination of these two parameters (manually evaluated size of SN area and moment of inertia) could increase the classification rate. Comparatively, a small target group is a certain limitation of this study. Summarizing the results of the study, it should be mentioned that the results obtained with this approach were substantially lower to compare with the findings presented by the other authors (Chien et al., 2011).

**Table 4.7** The results of classification using different features of ½ ROI

No.	CR (%)	Se (%)	Sp (%)
1.	60.00	56.66	64.00
2.	70.37	62.50	76.66
3.	72.72	76.00	70.00
4.	69.09	76.00	63.33
SFSf (412 features)	<b>78.18</b>	<b>80.00</b>	<b>76.66</b>
SFSb (412 features)	74.45	72.00	76.66
SFS (412 + SN*)	<b>87.27</b>	<b>83.33</b>	<b>92.00</b>

\* - manually outlined SN area, f – forward, b – backward, No. – number of tested subset.

**Large-scale study.** Full TCS image processing system (see Fig. 3.1) was tested by using clinical data presented in Tables 4.5 and 4.6. The feature preselection and validation scheme are presented in Fig. 3.14. In total, 29 potential features were evaluated as candidates for the echogenicity grade assessment. The goal of research was to establish the subsets of parameters best separating PD:

- (1) vs ET,
- (2) vs control group,
- (3) vs SeP,
- (4) vs MCI.

**Results.** Table 4.8 presents the main results of PD (hyperechogenicity) recognition. The experiments were made in 3 categories. At first, only automatically extracted features were used. Secondly, the features were fused with the parameters evaluated manually in the routine clinical procedures, and finally, only the results of the manual SN area assessment were used for the separation of the groups using the threshold established at LUHS (thresholds  $0.20 \text{ cm}^2$ ).

**Table 4.8** The classification results obtained by testing the proposed system

DGN	Auto			Auto + Clinical Data			Clinical Data*, $0.20 \text{ cm}^2$		
	CR, %	Se, %	Sp, %	CR, %	Se, %	Sp, %	CR, %	Se, %	Sp, %
2	70.00	70.34	69.56	84.76	83.05	86.96	84.28	91.53	75.00
5	80.11	86.44	69.86	88.48	90.68	84.93	86.91	91.52	79.45
7	75.35	76.24	70.83	88.73	92.37	70.83	89.43	91.52	79.16
6	73.68	79.55	38.46	80.26	83.89	67.64	80.26	91.53	41.18

\* – diagnoses are arranged by using the same numbering as in Table 4.6, Auto – classification results obtained by using only the features extracted by the automated system, Auto+Clinical Data – the results obtained by using the combined data set, Clinical Data – the results obtained by using only the manual ultrasonic SN area evaluations (maximal SN plot was the main indicator dividing the subjects respectively to the established threshold values  $0.20 \text{ cm}^2$ ).

Table 4.9 presents the established subsets of the best separating features for all the tested groups (PD vs ...). The highest classification results were achieved when the complex of extracted features and clinical data were used. As it was expected, the control group was best separable (CR = 88.48%) from the PD affected subjects. SeP (34) and MCI (24) groups were relatively small, and the presented classification results are not very valuable and reliable. The cross-validation was substituted by 60%/40% (train/test) strategy for these two groups, since the huge drift of the results was noticed by using the cross-validation, due to the small sample size. However, the trends are the same for the automated and manual approaches; 5 and 7 groups are best separable from PD, since it is clear that the neurodegeneration is absent for these groups. Meanwhile, the ET and AP groups are certain movement disorders, and the hyperechogenicity property is a bit more frequent there, especially for SeP. SeP and PD are hardly separable even by the experienced experts of the movement disorders, taking into account all the results and clinical findings.

**Table 4.9.** The sets of the features giving the best separation between PD and other groups

PD vs	Auto	Auto + Clinical Data	Clinical Data
2	SN area with a RROI constraint Otsu criterion	SN area with a RROI constraint Otsu criterion Manually evaluated SN area	Manually evaluated SN area
5	SN area with a RROI constraint Midbrain area Otsu criterion	Areas Ratio SN/Midbrain SN area with a RROI constraint Manually evaluated SN area	
7	SN area with a RROI constraint Otsu criterion	Otsu criterion SN area with a RROI constraint Entropy ratio (RROI/MB) Manually evaluated SN area	
6	1 <sup>st</sup> Hu moment, RROI/MB regions ratio	1 <sup>st</sup> Hu moment RROI/MB regions ratio SN plot manual Width of 3 <sup>rd</sup> ventricle.	

The investigation had demonstrated that the proposed features are too weak to be used in the clinical practice for the automated assessment of the echogenicity grade, but are not hopeless. The obtained CR for the control group was 80.11% (Se = 86.44%, Sp = 69.86%), MCI – 75.35% (Se = 76.24%, Sp = 70.83%). The obtained specificity values (Sp ~ 70%) indicate that the SN region is frequently overestimated and confirms the findings presented in 4.3 subsection. The tested feature set was insufficient for the reliable and clinically acceptable fully automated estimation of the SN grade, but the results of the same order are achievable by the other authors developing algorithms for the ultrasonic image based tissue characterization in the other applications. The results of a few presented approaches: in carotid atherosclerotic plaques recognition (Christodoulou et al., 2003; Tsiaparas et al., 2011), 73.1% and 82% ratio were achieved respectively, CR of liver fibrosis recognition was 85.2% (Gautiao et al., 2005) or 83.05% for the breast lesions recognition in the ultrasonic images (Gomez et al., 2012).

Fortunately, the fused complex data set possibly could be meaningful for the decision support. The usage of complex features marginally improved the classification results (PD vs 5: + 1.57%; PD vs 2: + 0.49%) to compare with the routine methodology (SN area threshold 0.26 cm<sup>2</sup>) used in the clinical practice. The results of MCI and SeP are of limited statistical reliability and, therefore, are inconclusive. The larger dataset is needed in order to achieve the reliable results for all the groups.

The most informative and repeatable features from the tested set was the Otsu criterion obtained by extracting RROI region and the automatically evaluated SN area with a RROI constraint. Both features were found as informative for the PD vs 2, 5 and 7 diagnoses and seem to be stable. The Otsu variance criterion  $\sigma^2$  was a bit lower for the subjects without hyperechogenicity, since the histograms are better separable in the PD group due to the existing SN contrast. SN area with a RROI

constraint (later SN size) is a mixed feature obtained by combining the results of SN and RROI extraction algorithms. All the pixels outside the RROI region extracted in the SN segmentation stage were filtered out. The manually evaluated SN area was the parameter found informative for all the groups when the complex feature set was used. The Width of 3<sup>rd</sup> ventricle was as well found informative for the SeP group. The features for PD vs Control group were analysed in a greater detail. The distributions are presented in Fig. 4.11. The Fig. 4.11 (A) presents the scatter plot of Otsu criteria and SN plot separated linearly. It could be noticed that the number of classification errors are comparatively high. The distributions of Otsu criterion and the SN area for both groups are presented in Fig. 4.11 (B) and (C), respectively. The trend to distinguish could be seen in both cases, but the overlap between the groups is relatively huge and is demonstrating that these two features could not be used for the hyperechogenicity recognition solely, and only the complex feature set could be the solution. The distribution of manually evaluated SN regions is as well presented in Fig. 4.12 D. The presented chart shows a high distinction between the PD and control groups when manually evaluating SN.

The results were compared with the classification ratio which is achievable by using the features proposed by the other authors for the automated image based echogenicity assessment in case of TCS. Only the PD vs Control group was investigated. The features (mean, standard deviation and entropy) extracted by using the rotation invariant Gabor wavelet based multiscale filter bank proposed by Al-Zubaidi et al. (2013), the moment invariants proposed by Kier et al. (2009), novel EI parameter proposed by Skoludik et al. (2014) were tested. The features proposed by Chien were not analysed, since it was reported that the higher results are achievable by using Al-Zubaidi et al. (2013) approach. The results of PD recognition and the most informative features are presented in Table 4.10. The proposed approach was performed better in comparison to the other echogenicity assessment methods presented in the scientific literature. The forthcoming was the echogenicity parameter proposed by Školudik et al. (2014) with the CR = 71.16%.

Spatial frequency based analysis and the moment invariants suffer due to certain limitations. At first, the  $\frac{1}{2}$  ROI is relatively a coarse to be used for the integral estimation of the SN echogenicity. Moreover, such methodology is sensitive and not repetitive for the different scanning settings and machines. The obtained CR is relatively low to compare with the results presented by Al-Zubaidi et al. (2013) or Chien et al. (2010, 2011). This could be explained by the lower image SNR in the tested dataset. The proposed approach is automated in all the stages. Meanwhile, other authors used manually annotated TCS images.

**Discussion and conclusion.** The achieved results demonstrate that the automated echogenicity assessment needs further improvements. It is known that the hyperechogenicity is found in approximately 10% of the healthy subjects, thus lowering the limit of PD recognition accuracy that is possible to achieve. The detailed investigation of PD vs Control group features revealed that the automated SN evaluation accuracy was lower to compare with manual assessment performed by the experienced neurologist (see Fig. 4.11 (C) and (D)).

**Table 4.10** The results achievable by the methods proposed by the other authors

	<b>CR, %</b>	<b>Se, %</b>	<b>Sp, %</b>	<b>#</b>
Kier et al., 2009	64.19	65.15	62.65	8
Al-Zubaidi et al., 2013	68.37	77.27	54.22	90
Školudik et al., 2014	71.16	75.76	63.85	1
<b>Proposed approach</b>	80.11	86.44	69.86	29

However, the evaluation performing neurologist can imply all the gathered experience and as well observe the brain structures dynamically. Moreover, the manual assessment of the SN area could be called semi-blind, since the physician could visually evaluate the movements and behaviour of the subject who is under ultrasonic examination. The reliability of “gold standard” (Clinical diagnosis) is as well debatable, since PD is frequently not confirmed after the autopsy (WHO, 2008). The PD recognition accuracy could be improved by using few planes for the evaluation. Only single B-scan was preselected per case in this research. However, it is not so easy to deal with the huge amount of data. Transcranial images are specific due to the non-linear distortions induced by the skull bone and the image properties (intensity range, spatial resolution) that are variable between the cases, and the image quality criteria or the categorization of the input images could help to find the features of the particular group and increase the PD recognition accuracy.

TCS has the potential to become a powerful tool in the diagnostics of various neurological movement disorders. Deep brain structures such as the mesencephalic brainstem (substantia nigra, median midbrain raphe, red nucleus) as well as basal ganglia and ventricular system could be assessed and evaluated by TCS. Transcranial imaging contributes to identifying subjects having PD, depression, dementia and other neurologic diseases. The image quality is the limiting factor slowing down the TCS entrance in the routine clinical practice. All the investigated images were collected by the same neurosonographer. The earlier researches (Školoudik et al., 2007) revealed that the TCS examination is experience demanding. The expert who acquired and evaluated the images performed TCS twice (carried out on the same day) in 10 cases by using two ultrasound scanners (Voluson730 Expert and Philips *HD15*) by the end of 2014. The strong correlation (Spearman’s  $r \geq 0.72$ ) and substantial diagnostic agreement ( $\kappa \geq 0.64$ ) when evaluating SN area have been found. This study and previously presented findings (diagnostic agreement  $\kappa$  comparing three repetitive SN evaluations of the images collected at the same session varied in the range of 0.43-0.85, see subsection 2.2) demonstrate that the neurosonographer is capable to reproduce TCS examination, but the noticeable spread in case of TCS is observed. However, the heterogeneous data set has to be collected in order to confirm the stability and repeatability of the determined informative image features. It would be meaningful to involve a few observers having different experiences in TCS and to evaluate how this affects the quality of acquired data and efficiency of the proposed image processing algorithms.

In summary, the certain level of automatism was achieved. Automated algorithms for the extraction of informative regions were proposed. A graphical user

interface in MATLAB environment was developed, and it could be used for the extraction of informative regions (*midbrain* and *substantia nigra*) and quantitative evaluation of echogenicity in ROI, which is the main ultrasonic biomarker for the PD.

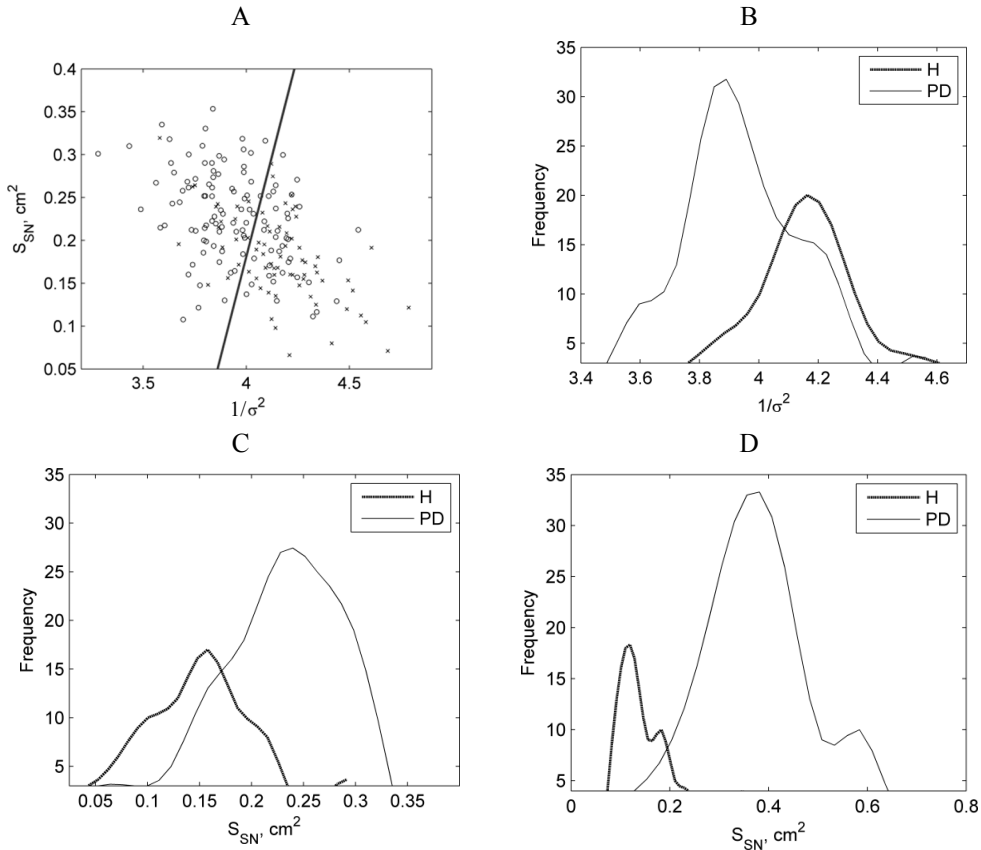


**Fig. 4.11** The distributions of the most informative features for PD and the control group (H): (A) the scatter plot of two automatically extracted features (SN area and inverse of Otsu criterion) having the best discrimination power separated linearly (o – PD group, × – control group), (B) the distributions of Otsu criterion inverse for both groups, (C) the distributions of automatically evaluated SN, (D) the distributions of manually evaluated SN areas

The front panel of the interface is presented in Fig. 4.12. The proposed system could serve not only as a tool for the assessment of supplementary features for echogenicity evaluation, but also for the training of the novice neurosonographers to outline the SOI, since TCS measurements are experience demanding. The automated algorithm for the midbrain extraction reduces the existing inter-observer and intra-observers variability. The proposed denoising algorithm significantly improves the SNR and CNR of the images, thus making them more convenient for the evaluation purpose. The proposed SN extraction and echogenicity evaluation strategy still

requires improvements, since the automated PD recognition accuracy is lower to compare with the obtained using routine clinical methodology. However, the system could be used as a supplementary tool.

**Future directions.** Ultrasonic B-scan images obtained by the conventional commercial scanning machines are formed from a set of ultrasonic signals as well called the radio frequency (RF) scanning lines. It is supposed that a part of the potential information is lost due to the operations applied during the image reconstruction (band-pass filtering, envelope detection, non-linear suppression). B-scan image covers information about the amplitude of reflections solely; meanwhile, all the info about instantaneous phases and primary frequency content of the pulses is lost. RF data analysis based tissue characterization is finding the place and superiority over the B-scan images.

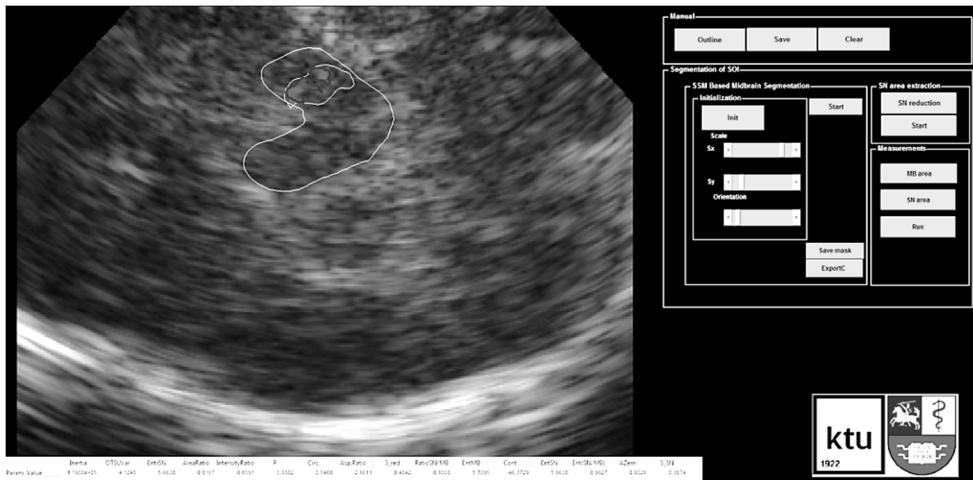


**Fig. 4.12** Front panel of the user interface developed for the automated TCS image segmentation and evaluation

Raw RF data analysis is a promising tool for the ultrasonic tissue characterization in the neurological applications. To our knowledge, there are no approaches where the raw ultrasonic signals of the brain were analysed up to date. It is aimed to collect the representable dataset of RF signals of the brain (for the PD and control groups) and to evaluate the potential to characterize the brain tissue in the further studies. The ultrasonic image features are sensitive to the user-predefined settings of the ultrasound scanner (gain, TGC etc.) and the algorithms used by the manufacturers for B-scan image formation (shape of the log-compression curve, gray mapping curve, denoising filters etc.). This causes difficulties to construct stable and reliable image processing algorithms. All the images were collected by a single ultrasound scanner Voluson730 Expert, and this is a limitation of the study. The lower algorithms efficiency could be expected if they were applied on the images obtained by the other equipment, due to the differences listed above. It is aimed to evaluate how each image formation stage affects the algorithm's behaviour by using raw RF data. The proposed algorithms could be adapted to work with raw RF signals, thus

mitigating the differences arising in the image formation stages. Unfortunately, almost all departments of radiology worldwide are equipped with the commercial scanners who do not allow to utilize RF signals for the further analysis; therefore, it is desirable to achieve algorithms invariancy to the equipment used for the data acquisition. It is possible to adjust the algorithm controlling parameters by using the empirical scheme (see subsection 4.2); this way is time consuming and requires representable sample for the tuning. There is a third way to adjust the parameters by using tissue mimicking phantoms or simulate the TCS images with respect to the used equipment. However, it is not so trivial to manufacture the phantoms having variable acoustic properties (the explanation is given in the 4.2 subsection). The B-scan images are constructed with an intention to find the optimal representation for the visual evaluation. For example, the log-compression is applied in order to arrange the different amplitude reflections in the range whereat the observer is able to identify these differences. Meanwhile, frequently, the differences in ROI are relatively small and could be displayed optimally if the log-compression curve would be ROI oriented. The optimization of imaging preset for the TCS is highly welcome, since up to date, it is absent in the most of the commercial ultrasonic machines.

#### **4.5. Conclusions of the 4<sup>th</sup> chapter**

1. It was demonstrated that the statistically significant ( $p < 0.05$ ) image quality improvement could be achieved from the point of view of SNR and CNR by applying the multiplanar processing. The improvements are clearly seen even by the visual evaluation. The determined FtF shift distance could serve as a preselection criterion for the decorrelated frames in a sequence or even in the development of quasi real-time approach by using external probe position tracking sensor.
2. Novel, fast and efficient PSSM based midbrain segmentation algorithm was developed. The differences between the automatically evaluated ROI region and reference evaluations performed by two experts were statistically insignificant ( $p \gg 0.05$ ). The empirical scheme for the selection of optimal algorithm parameters was proposed, and it could be used for the algorithm calibration by applying the method for processing of images obtained by the other ultrasound machines.
3. The size of automatically extracted SN area was moderately correlated with the manual evaluations performed by two experts (Spearman's  $r > 0.5$ ,  $p < 0.05$ ). The relatively wide limits of agreement indicate that the reliability of the proposed technique is limited. Low specificity values indicate that the biggest errors occur due to false pixels assigned to the SN class.
4. The best classification results were achieved when the complex of extracted features and clinical data was used. It was determined that the proposed approach outperforms the methods for the automated SN echogenicity evaluation proposed by the other authors. Low specificity values indicate that the main shortage is the overestimation of normal SN.

## 5. GENERAL CONCLUSIONS

1. TCS is innovative and undoubtedly valuable tool for the assessment of the brain parenchyma and could be used for screening of elderly people, but the examination is comparatively subjective and experience-demanding; therefore, the technical improvements towards reliability and repeatability are mandatory.

2. The novel algorithms for the denoising and automated segmentation of the informative brain structures in diagnostic B-mode TCS images were developed.

The experimental investigation demonstrated that:

(a) statistically significant ( $p < 0.05$ ) image quality improvement could be achieved from the point of view of SNR and CNR applying the multiplanar processing. The main benefit of averaging is reached adding the first 20-30 frames of a sequence, and this threshold could be used as a stoppage criterion.

(b) the differences between automatically evaluated midbrain regions extracted by PSSM based method and evaluations performed by two experts were statistically insignificant ( $p \gg 0.05$ ). It was determined that the proposed boundary detection based on phase congruency outperforms the classical amplitude based method. The semi-automatic algorithm is experience undemanding, since even a novice operator was capable to achieve the similar results to the experienced and familiar with the TCS person.

(c) The size of automatically extracted SN area was moderately correlated with the manual evaluation performed by two experts (Spearman's  $r > 0.5$ ,  $p < 0.05$ ). The relatively wide limits of agreement indicate that the reliability of the proposed technique is limited. The investigation of raters variability had shown that the correlation of the same order ( $r = 0.51$ ) is achieved comparing the manual segmentations performed by the two experts having different experiences. The improvements of the method could be achieved by collecting the more "colourful" dataset for algorithm training (delineations of the few sonographers, average of repetitive delineations of the same expert etc.).

3. The investigation of the proposed TCS image feature set showed that the proposed parameters are too weak to be used in the clinical practice for the echogenicity evaluation solely. The best classification results were achieved when the complex of extracted features and clinical data was used. The PD recognition accuracy possibly could be improved by using the proposed supplementary parameters by 1-2%. It was determined that the proposed approach outperforms the methods for the automated SN echogenicity assessment, which were found in the contemporary scientific literature (achieved results for PD vs Control groups CR=80.11%, Se=86.44%, Sp=69.86%).

4. The developed image processing system could serve as a tool for the acquisition of supplementary parameters for the midbrain echogenicity evaluation. An algorithm for midbrain segmentation reduces the observer's variability (the estimated DICE standard deviation between 2 observers

$\pm 2.32\%$ ; meanwhile, between the experts  $\pm 3.43\%$ ). Moreover, it could be used for the training of novice neurosonographers to outline the brain structures of interest (midbrain and substantia nigra).

## REFERENCES

1. AERTS, M. B., ESSELINK, R. A., POST, B., VAN DE WARRENBURG, B. P., BLOEM, B. R. Improving the Diagnostic Accuracy in Parkinsonism: A Three-Prolonged Approach. In *Practical Neurology*. 2012, 12, 77-87. ISSN 1474-7766.
2. AGAMANOLIS, D. P. *Neuropathology. An Illustrated Interactive Course for Medical Students and Residents*. 2014. Electronic course material available at: <http://neuropathology-web.org/chapter9/chapter9dPD.html>.
3. AHMADI, S. A., BAUST, M., KARAMALIS, A., PLATE, A., BOETZEL, K., KLEIN, T., NAVAB, N. Midbrain Segmentation in Transcranial 3D Ultrasound for Parkinson Diagnosis. In *Proc. International Conference on Medical Image Computing and Computer Assisted Intervention (MICCAI)*, Toronto (CA), September 18-22, 2011, 14. pp. 362-369.
4. AJA-FERNANDEZ, S., and C. ALBEROLA-LOPEZ. On the Estimation of the Coefficient of Variation for Anisotropic Diffusion Speckle Filtering. In *IEEE Transactions on Image Processing*. 2006, 15(9), 2694-2701. ISSN 1057-7149.
5. ALONSO-CANOVAS, A., LOPEZ-SENDON, J. L., BUISAN, J, DEFELIPE-MIMBRERA, A., GUILLAN, M., GARCIA-BARRAGAN, N., CORRAL, I., MATUTE-LOZANO, M. C., MASJUAN, J., MARTINEZ-CASTRILLO, J. C., WALTER, U. Sonography for Diagnosis of Parkinson Disease--From Theory to Practice: A Study on 300 Participants. In *Journal of Ultrasound in Medicine*. 2014, 33(12), 2069-2074. ISSN 0278-4297.
6. AL-ZUBAIDI, A., CHEN, L., HAGENAH, J., MERTINS, A. Robust Feature for Transcranial Sonography Image Classification Using Rotation-Invariant Gabor Filter. In *Bildverarbeitung für die Medizin*, 2013, 271-276.
7. AUBRY, J. F., CASSERAU, D., TANTER, M., PELLEGRINI, T., FINK, T. Skull Surface Algorithm to Optimize Time Reversal Focusing through a Human Skull. In *IEEE Ultrasonics Symposium*, October 8-11, 2002. pp. 1451-1454.
8. AUBRY, J. F., GERBER, J., TANTER, M., THOMAS, J. L. Towards Ultrasonic Brain Imaging. In *IEEE Ultrasonic Symposium*, October 22-25, 2000. pp. 1623-1627.
9. AUBRY, J. F., TANTER, M., PERNOT, M., THOMAS, J. L., FINK, M. Experimental Demonstration of Noninvasive Transskull Adaptive Focusing Based on Prior Computed Tomography Scans. In *The Journal of the Acoustical Society of America*. 2003, 113(1), 84-93. ISSN 0001-4966.
10. AUBRY, J. F., TANTER, M., THOMAS, J. L., FINK, M. Pulse Echo Imaging a Through Human Skull: In Vitro Experiments. In *IEEE Ultrasonic Symposium*, October 7-10, Atlanta, 2001. pp. 1499-1502.
11. AUDET, C., and J. E. DENNIS JR. Analysis of Generalized Pattern Searches. In *SIAM Journal on Optimization*. 2003, 13(3), 889-903. ISSN 1052-6234.
12. AUDIÈRE, S., ANGELINI, E. D., CHARBIT, M., MIETTE, V. Evaluation of In Vivo Liver Tissue Characterization with Spectral RF Analysis Versus Elasticity. In *International Conference on Medical Image Computing and Computer Assisted Intervention (MICCAI)*, Toronto (CA), September 18-22, 2011, 14(1). pp. 387-395.
13. BARTOVA, P., OTAKAR, K., BERNATEK, J., et al. Transcranial Sonography and 123I-FP-CIT Single Photon Emission Computed Tomography in Movement Disorders. In *Ultrasound in Medicine and Biology*. 2014, 40(10), 2365-2371. ISSN 0301-5629.

14. BAXTER, G. M., ALLAN, P. L. P., and P. MORLEY. Clinical Diagnostic Ultrasound. In *Blackwell Science*. 1999, 30 – 34. ISBN: 9780632037445.
15. BECKER, G., SEUFERT, J., BOGDHORN, U., REICHMANN, H., REINERS, K. Degeneration of Substantia Nigra in Chronic Parkinson's Disease Visualized by Transcranial Color-Coded Real-Time Sonography. In *Neurology*. 1995, 45, 182-184. ISSN 0028-3878.
16. BECKER, G., STRUCK, M., BOGDHORN, U., BECKER, T. Echogenicity of the Brainstem Raphe in Patients with Major Depression. In *Psychiatry Research*. 1994, 55, 75-84. ISSN 0165-1781.
17. BEHAR, V., ADAM, D., and Z. FRIEDMAN. A New Method of Spatial Compounding Imaging. In *Ultrasonics*. 2003, 41(5), 377-384. ISSN 0041-624X.
18. BEHNKE, S., RUNKEL, A., KASSAR, H. A., ORTMANN, M., GUIDEZ, D., DILLMANN, U., et al. Long-Term Course of Substantia Nigra Hyperechogenicity in Parkinson's Disease. In *Movements Disorders*. 2013, 28, 455-459. ISSN 1531-8257.
19. BEHNKE, S., SCHROEDER, U., DILLMANN, U., BUCHHOLZ, H. G., SCHRECKENBERGER, M., FUSS, G., REITH, W., BERG, D., KRICK, C. M. Hyperechogenicity of the Substantia Nigra in Healthy Controls Is Related to MRI Changes and to Neuronal Loss as Determined by F-Dopa PET. In *NeuroImage*. 2009, 47, 1237-1243. ISSN 1053-8119.
20. BELAID, A., BOUKERROUI, D., MAINGOURD, Y., LERALLUT, J. F. Phase-Based Level Set Segmentation of Ultrasound Images. In *IEEE Transactions on Information Technology in Biomedicine*, 2011, 15(1), 138-147. ISSN 1089-7771.
21. BELAID, A., BOUKERROUI, D., MAINGOURD, Y., LERALLUT, J. F. Implicit Active Contours for Ultrasound Images Segmentation Driven by Phase Information and Local Maximum Likelihood. In *IEEE International Symposium on Biomedical Imaging*, Chicago, March 30 – April 2, 2011. pp. 630-635.
22. BERARDELLI, A., WENNING, G. K., ANTONINI, A., BERG, D., BLOEM, B. R., BONIFATI, V., BROOKS, D., BURN, D. J., COLOSIMO, C., FANCIULLI, A., FERREIRA, J., GASSER, T., GRANDAS, F., KANOVSKY, P., KOSTIC, V., KULISEVSKY, J., OERTEL, W., POEWE, W., REESE, J-P., RELJA, M., RUZICKA, E., SCHRAG, A., SEPPI, K., TABA, P., VIDAILHET, M. EFNS/MDS-ES Recommendations for the Diagnosis of Parkinson's Disease. In *European Journal of Neurology*. 2013, 20, 16-34. ISSN 1468-1331.
23. BERG, D. Substantia Nigra Hyperechogenicity Is a Risk Marker of Parkinson's Disease: Yes. In *Journal of Neural Transmission*. 2011, 118, 613 – 619. ISSN 0300-9564.
24. BERG, D., and U. WALTER. Transcranial Sonography in Movement Disorders. In *International Review of Neurobiology*. 2010, 90, 8-59. ISBN: 978-0-12-381330-5.
25. BERG, D., GODAU, J., and U. WALTER. Transcranial Sonography in Movement Disorders. In *The Lancet Neurology*. 2008, 7(11), 1044-1055. ISSN 1474-4422.
26. BERG, D., GROTE, C., and W. D. RAUSCH. Iron Accumulation in the Substantia Nigra in Rats Visualized by Ultrasound. In *Ultrasound in Medicine and Biology*. 1999, 25, 901-904. ISSN 0301-5629.
27. BERG, D., MERZ, B., REINERS, K., NAUMANN, M., BECKER, G. Five-Year Follow-Up Study of Hyperechogenicity of the Substantia Nigra in Parkinson's Disease. In *Movement Disorders*. 2005, 20, 383-385. ISSN 1531-8257.
28. BERG, D., ROGGENDORF, W., and U. SCHROEDER. Echogenicity of the Substantia Nigra: Association with Increased Iron Content and Marker for

- Susceptibility to Nigrostriatal Injury. In *Archives of Neurology*. 2002, 56, 999-1005. ISSN 0003-9942.
29. BERG, D., SEPPI, K., BEHNKE, S., LIEPELT, I., SCHWEITZER, K., STOCKNER, H., WOLLENWEBER, F., GAENSLEN, A., MAHLKNECHT, P., SPIEGEL, J., GODAU, J., HUBER, H., SRULIJES, K., KIECHL, S., BENTELE, M., GASPERI, A., SCHUBERT, T., HIRY, T., PROBST, M., SCHNEIDER, V., KLENK, J., SAWIRES, M., WILLEIT, J., MAETZLER, W., FASSBENDER, K., GASSER, T., POEWE, W. Enlarged Substantia Nigra Hyperechogenicity and Risk for Parkinson Disease: A 37-Month 3-Center Study of 1847 Older Persons. In *Archives of Neurology*. 2011, 68, 932-937. ISSN 0003-9942.
  30. BERG, D., SIEFKER, C., and G. BECKER. Echogenicity of the Substantia Nigra in Parkinson's Disease and Its Relation to Clinical Findings. In *Journal Neurology*. 2001, 248, 684-689. ISSN 0340-5354.
  31. BLAHUTA, J., SOUKUP, T., and P. ČERMÁK. The Recognition of Substantia Nigra in Brain-Stem Ultrasound Images Based on Principal Component Analysis. In *Mathematical Models for Engineering Science, MMES*, Tenerife, November 30-December 2, 2010, 10. pp. 94-98.
  32. BLAHUTA, J., SOUKUP, T., ČERMÁK, P. The Image Recognition of Brain-Stem Ultrasound Images with Using a Neural Network Based on PCA. In *Proceedings of the 10<sup>th</sup> WSEAS International Conference on Communications, Electrical & Computer Engineering, and 9<sup>th</sup> WSEAS International Conference on Applied Electromagnetics, Wireless and Optical Communications*, 2011. pp. 134-142.
  33. BLAHUTA, J., SOUKUP, T., CERMAK, P., ROZSYPAL, J., VECEREK, M. Ultrasound Medical Image Recognition with Artificial Intelligence for Parkinson's Disease Classification. In *Proceedings of the 35<sup>th</sup> International Convention, MIPRO 2012*, Opatija, Croatia, May 21-25, 2012. pp. 958-962.
  34. BLAZEJEWSKA, A. I., SCHWARZ, S. T., PITIOT, A., STEPHENSON, M., LOWE, J., BAJAJ, N., BOWTELL, R. W., AUER, D. P., GOWLAND, P. A. Visualization of Nigrosome 1 and Its Loss in PD. In *Neurology*. 2013, 81, 535-540. ISSN 0028-3878.
  35. BOCKLET, T., NOTH, E., STEMMER, G., RUZICKOVA, H., RUSZ, J. Detection of Persons with Parkinson's Disease by Acoustical, Vocal, and Prosodic Analysis. In *IEEE Workshop on Automatic Speech Recognition and Understanding (ASRU)*, Waikoloa, December 11-15, 2011. pp. 478-483.
  36. BOUWMANS, A. E. P., VLAAR, A. M. M., MESS, W. H., KESSELS, A., WEBER, W. E. J. Specificity and Sensitivity of Transcranial Sonography of the Substantia Nigra in the Diagnosis of Parkinson's Disease: Prospective Cohort Study in 196 Patients. In *BMJ Open*. 2013, 3(4), 1-8. ISSN 2044-6055.
  37. BREIMAN, L. Random Forests. In *Machine Learning*. 2001, 45(1), 5-32. ISSN 0885-6125.
  38. BROOKS, D. J. Imaging Approaches to Parkinson Disease. In *The Journal of Nuclear Medicine*. 2010, 51(4), 596-609. ISSN 0161-5505.
  39. BURCKHARDT, C. B. Speckle in Ultrasound B-Mode Scans. In *IEEE Transactions on Sonics and Ultrasonics*. 1978, 25(1), 1-6. ISSN 0885-3010.
  40. CAO, G., SHI, P., and B. HU. Liver Fibrosis Identification Based on Ultrasound Images. In *Proceedings of 2005 IEEE Engineering in Medicine and Biology 27<sup>th</sup> Annual Conference*, China, Shanghai, September 1-4, 2005, 2006. pp. 6317-6320.
  41. Centre National De La Rechercher Scientifique – CNRS. *Method and Non-Invasive Device for Focusing Acoustic Waves*. Inventors: AUBRY, J. F., FINK, M. A.,

- TANTER, M., THOMAS, J. US patent, US 7101337 B2, 05-10-2006. [reviewed 22-05-2013] Link: <https://www.google.com/patents/US7101337>.
42. ČERVIKOV, S., MOVŠOVIČ, I., OSIPOV, L. *Galvos smegenų kokybiško ultragarsinio vaizdo gavimo būdas*. LT patent, LT2008069A, 2008.
  43. CHAN, T. F., and L. A. VESE. Active Contours without Edges. In *IEEE Transactions on Image Processing*. 2001, 10(2), 266-277. ISSN 1057-7149.
  44. CHEN, L., HAGENAH, J., and A. MERTINS. Feature Analysis for Parkinson's Disease Detection Based on Transcranial Sonography Image. In *Proceedings of the 15<sup>th</sup> International Conference on Medical Image Computing and Computer Assisted Intervention (MICCAI)*, Nice, October 1-5, 2012. pp. 272-279.
  45. CHEN, L., HAGENAH, J., and A. MERTINS. Texture Analysis Using Gabor Filter Based on Transcranial Sonography Image. In *Proceedings of the Bildverarbeitung für die Medizin*, 2011. pp. 249-253.
  46. CHEN, L., SEIDEL, G., and A. MERTINS. Multiple Feature Extraction for Early Parkinson Risk Assessment Based on Transcranial Sonography Image. In *Proceedings of the 17<sup>th</sup> IEEE International Conference on Image Processing, ICIP*, September 26-29, 2010. pp. 2277-2280.
  47. CHRISTENSEN, A. E., FRANDBSEN, R., KEMPFNER, J., ARVASTSON, L., CHRISTENSEN, S. R., JENNUM, P., SORENSEN, H. B. D. Separation of Parkinson's Patients in Early and Mature Stages from Control Subjects Using One EOG Channel. In *34<sup>th</sup> Annual International Conference of the IEEE EMBS*, San Diego, August 28 - September 1, 2012. pp. 2941-2944.
  48. CHRISTODOULOU, C. I., PATTICHIS, C. S., PANTZIARIS, M., NICOLAIDES, A. Texture-Based Classification of Atherosclerotic Plaques. In *IEEE Transactions on Medical Imaging*. 2003, 22(7), 902-912. ISSN 1558-0062.
  49. CIULLA, M., PALIOTTI, R., HESS, D. B., TIAHJA, E., CAMPBELL, S. E., MAGRINI, F., WEBER, K. T. Echocardiographic Patterns of Myocardial Fibrosis in Hypertensive Patients: Endomyocardial Biopsy Versus Ultrasonic Tissue Characterization. In *Journal of American Society Echocardiography*. 1997, 10(6), 657-664. ISSN 0894-7317.
  50. COLUCCIA, D., FANDINO, J., SCHWYZER, L., O'GORMAN, R., REIMONDA, L., ANON, J., MARTIN, E., WERNER, B. First Noninvasive Thermal Ablation of a Brain Tumour with MR-Guided Focused Ultrasound. In *Journal of Therapeutic Ultrasound*. 2014, 16, 2-17. ISSN 2050-5736.
  51. COOTES, T. An Introduction to Active Shape Models. Model-Based Methods in Analysis of Biomedical Images in Image Processing and Analysis. In Baldock R., Graham J. *Image Processing and Analysis: A Practical Approach*. Oxford University Press, 2000.
  52. COOTES, T. F., TAYLOR, C. J., COOPER, D. H., GRAHAM, J. Active Shape Models-Their Training and Application. In *Comput Vision Image Und*. 1995, 61, 38-59. ISSN 1077-3142.
  53. CORTES, C., and V. VAPNIK. Support-Vector Networks. In *Machine Learning*. 1995, 20 (3), 273-297. ISSN 0885-6125
  54. CULJAT, M. O., GOLDENBERG, D., TEWARI, P., SINGH, R. S. A Review of Tissue Substitutes for Ultrasound Imaging. In *Ultrasound in Medicine and Biology*. 2010, 36(6), 861-873. ISSN 0301-5629.
  55. CUNNINGHAM, D. J. *Cunningham's Textbook of Anatomy*. Oxford University Press; 11<sup>th</sup> edition, 0192631233, 1972.

56. DAMIER, P., HIRSCH, E. C., AGID, Y., GRAYBIEL, A. M. The Substantia Nigra of the Human Brain. II. Patterns of Loss of Dopamine-Containing Neurons in Parkinson's Disease. In *Brain*. 1999, 122, 1437-1448. ISSN 0006-8950.
57. DAMIER, P., HIRSCH, E. C., AGID, Y., GRAYBIEL, A. M. The Substantia Nigra of the Human Brain. I. Nigrosomes and the Nigral Matrix, a Compartmental Organization Based on Calbindin D<sub>28K</sub> Immunohistochemistry. In *Brain*. 1999, 122, 1421-1436. ISSN 0006-8950.
58. DERVISHI, E., BENOIT, L., PERNOT, M., ADAM, C., MARIE, Y., FINK, M., et al. Transcranial High Intensity Focused Ultrasound Therapy Guided by 7 TESLA MRI in a Rat Brain Tumour Model: A Feasibility Study. In *International Journal of Hyperthermia*. 2013, 29(6), 598-608. ISSN 0265-6736.
59. EGGERS, J. Sonothrombolysis for Treatment of Acute Ischemic Stroke. Current Evidence and New Developments. In *Perspectives in Medicine*. 2012, 1, 14-20. ISSN 2211-968X.
60. EL-BAZ, A. S., ACHARYA, U. R., MIRMEHDI, M., SURI, J. S. *Multi-Modality State-of-the-Art Medical Image Segmentation and Registration Methodologies*. Volume 1, 1<sup>st</sup> Edition, XII, ISBN 978-1-4419-8194-3, 2011.
61. ENGEL, K. and K. TOENNIES. Segmentation of the Midbrain in Transcranial Sonographies Using a Two-Component Deformable Model. In *Proceedings of the MIUA, Citeseer*, 2008, 3-7.
62. ENGEL, K., and K. TOENNIES K. Segmentation of the Midbrain in Transcranial Sonographies using a Two-Component Deformable Mode. In *Annals of the BMVA*. 2009, 4, 1-13.
63. ENGEL, K., and K. TOENNIES, K. An Evolutionary Strategy for Model-Based Segmentation of Medical Data. In *GI Jahrestagung*. 2009, 154, 1294-1308.
64. ENTREKIN, R. R., PORTER, B. A., SILLESEN, H. H., WONG, A. D., COOPERBERG, P. L., and C. H. FIX. Real-Time Spatial Compound Imaging: Application to Breast, Vascular, and Musculoskeletal Ultrasound. In *Seminars in Ultrasound, CT and MRI*. 2001, 22(2), 50-64. ISSN 0887-2171.
65. FEARNLEY, J. M., and A. J. LEES. Ageing and Parkinson's Disease: Substantia Nigra Regional Selectivity. In *Brain*. 1991, 114, 2283-2301. ISSN 0006-8950.
66. FINK, M. Time Reversal of Ultrasonic Fields--Part 1: Basic Principles. In *IEEE Transactions Ultrasonics, Ferroelectrics, and Frequency Control*. 1992, 39(5), 555-566. ISSN 0885-3010.
67. FINN, S., and M. GLAVIN. Echocardiographic Speckle Reduction Comparison. In *IEEE Transactions on Ultrasonics Ferroelectrics and Frequency Control*. 2011, 58(1), 82-101. ISSN 0885-3010.
68. FLEISS J. L. Measuring Nominal Scale Agreement among Many Raters. In *Psychological Bulletin*. 1971, 76(5), 378-382. ISSN 0033-2909.
69. FRY, F. J., and J. E. BARGER. Acoustical Properties of the Human Skull. In *Journal of Acoustic Society of America*. 1978, 63(5), 1576-90. ISSN 0001-4966.
70. GAENSLER, A., UNMUTH, B., GODOU, J., LIEPELT, I., DI SANTO, A., SCHWEITZER, K. J. The Specificity and Sensitivity of Transcranial Ultrasound in the Differential Diagnosis of Parkinson's Disease: A Prospective Blinded Study. In *The Lancet Neurology*. 2008, 7, 417-424. ISSN 1474-4422.
71. GATEAU, J., PERNOT, M., AUBRY, J. F., TANTER, M., FINK, M. Acoustically Induced and Controlled Micro-Cavitation Bubbles as Active Sources for Transcranial Adaptive Focusing. In *Proceedings of the 7<sup>th</sup> International Symposium on Cavitation*, Michigan, August 16-22, 2009. pp. 1-6.

72. GILL, P. E., MURRAY, W., and M. H. WRIGHT. *Practical Optimization*. London. Academic Press, 1981.
73. GOETZ, C. G., FAHN, S., MARTINEZ-MARTIN, P., POEWE, W., SAMPAIO, C., STEBBINS, G. T., STERN, M. B., TILLEY, B. C., DODEL, R., DUBOIS, B., HOLLOWAY, R., JANKOVIC, J., KULISEVSKY, J., LANG, A. E., LEES, A., LEURGANS, S., LEWITT, P. A., NYENHUIS, D., OLANOW, C. W., RASCOL, O., SCHRAG, A., TERESI, J. A., VAN HILTEN, J. J., LAPELLE, N. Movement Disorder Society-Sponsored Revision of the Unified Parkinson's Disease Rating Scale (MDS-UPDRS): Process, Format, and Clinimetric Testing Plan. In *Movement Disorders*. 2007, 22(1), 41-47. ISSN 1531-8257.
74. GOMEZ, W., PEREIRA, W. C. A., and A. F. C. INFANTOSI. Analysis of Co-Occurrence Texture Statistics as a Function of Gray-Level Quantization for Classifying Breast Ultrasound. In *IEEE Transactions on Medical Imaging*. 2012, 31(10), 1889-1899. ISSN 0278-0062.
75. GONZALEZ, R. C., and R. E. WOODS. *Digital Image Processing*. Second Edition, Prentice Hall, 2002.
76. GOODALL C. Procrustes Methods in the Statistical Analysis of Shape. In *Journal of Royal Statistical Society B*. 1991, 53(2), 285-339. ISSN 1467-9868.
77. HAGENAH, J. M., BECKER, B., BRUGGEMANN, N., DJARMATI, A., LOHMANN, K., SPRENGER, A., KLEIN, C., SEIDEL, G. Transcranial Sonography Findings in a Large Family with Homozygous and Heterozygous PINK1 Mutations. In *Journal of Neurology, Neurosurgery and Psychiatry*. 2008, 79, 1071-1074. ISSN 0022-3050.
78. HARALICK, R. M., and L. G. SHAPIRO. *Computer and Robot Vision*, Vol I, Addison-Wesley, 1992.
79. HARALICK, R. M., SHANMUGAM, K., and I. DINSTEN. Textural Features for Image Classification. In *IEEE Transactions on Systems, Man and Cybernetics*. 1973, 3(6), 610-621. ISSN 1083-4419.
80. HE, P., and J. ZHENG. Segmentation of Tibia Bone in Ultrasound Images Using Active Shape Models. In *Proceedings of the 23<sup>rd</sup> Annual International Conference of the IEEE Engineering in Medicine and Biology Society*, Turkey, Istanbul, October 25-28, 2001. pp. 2712-2715.
81. HOEHN, M., and M. YAHR. Parkinsonism: Onset, Progression and Mortality. In *Neurology*. 1967, 17(5), 427-442. ISSN 0028-3878.
82. HOEPPNER, J., PRUDENTE-MORRISSEY, L., HERPERTZ, S. C., BENECKE, R., WALTER, U. Substantia Nigra Hyperechogenicity in Depressive Subjects Relates to Motor Asymmetry and Impaired Word Fluency. In *The European Archives of Psychiatry and Clinical Neuroscience*. 2009, 259, 92-97. ISSN 0940-1334.
83. HOSKINS, P. R., MARTIN, K., and A. THRUSH. *Diagnostic Ultrasound. Physics and Equipment*. Cambridge University Press; 2<sup>nd</sup> edition, ISBN: 052175710X, 2010.
84. HOWRY, D., POSAKONY, G., CUSHMAN, R., HOMES, J. H. Three-Dimensional and Stereoscopic Observation of Body Structures by Ultrasound. In *Journal of Applied Physiology*. 1956, 9, 304-306.
85. HU, M. K. Visual Pattern Recognition by Moment Invariants. *The IEEE Transactions on Information Theory*. 1962, 8, 179-187. ISSN 0018-9448.

86. HUANG, Y. W., JENG, J. S., TSAI, C. F., CHEN, L. L., WU, R. M. Transcranial Imaging of Substantia Nigra Hyperechogenicity in Taiwanese Cohort of Parkinson Disease. In *Movement Disorders*. 2007, 22, 187-192. ISSN 1531-8257.
87. IVANCEVICH, M. N. *Phase Aberration Correction for Real-Time 3D Transcranial Ultrasound Imaging*. PhD. Thesis. Department of Biomedical engineering in the Graduate School of Duke University, 2009.
88. IVANCEVICH, N. M., DAHL, J. J., TRAHEY, G. E, SMITH, S. W. Phase-Aberration Correction with a 3-D Ultrasound Scanner: Feasibility Study. In *IEEE Transactions on Ultrasonics, Ferroelectrics and Frequency Control*. 2006, 53(8), 1432-1439. ISSN 0885-3010.
89. IVANCEVICH, N. M., PINTON, G. F., NICOLETTO, H. A., BENNET, E., LASKOWITZ, D. T., SMITH, S. W. Real-Time 3-D Contrast-Enhanced Transcranial Ultrasound and Aberration Correction. In *Ultrasound in Medicine and Biology*. 2008, 34, 1387-1395. ISSN 0301-5629.
90. JAIN, A. K., DUIN, P. W., and M. JIANCHANG. Statistical Pattern Recognition: A Review. In *IEEE Transactions on Pattern Analysis and Machine Intelligence*. 2000, 22(1), 4-37. ISSN 0162-8828.
91. JARQUIN-VALDIVIA A., MCCARTNEY, J., PALESTRANT, D., JOHNSTON, S. C., GRESS, D. The Thickness of the Temporal Squama and Its Implication for Transcranial Sonography. In *Journal of Neuroimaging*. 2004, 14(2), 139-142. ISSN 1552-6569.
92. JURKONIS, R., JANUŠAUSKAS, A., MAROZAS, V., JEGELEVIČIUS, D., DAUKANTAS, S., PATAŠIUS, M., PAUNKSNIS, A., LUKOŠEVIČIUS, A. Algorithms and Results of Eye Tissues Differentiation Based on RF Ultrasound. In *The Scientific World Journal*. 2012, 1-6. ISSN 1537-744X.
93. JURKONIS, R., JEGELEVIČIUS, D., MAROZAS, V. Virtualus prietaisas akies ultragarsinio B skenavimo signalų registravimui ir vaizdų formavimui. In *Virtualūs instrumentai biomedicinoje 2009: tarptautinės mokslinės-praktinės konferencijos pranešimų medžiaga*, Klaipėdos universitetas. Sveikatos mokslų fakultetas. Klaipėda. Klaipėdos universiteto leidykla, 2009. pp. 55-60.
94. JURKONIS, R., MAROZAS, V., and S. KURAPKIENĖ. Development and Evaluation of Virtual Instrument to Supplement Ultrasonic Echoscope System for Ophthalmology. In *Ultrasound*. 2007, 62(1), 12-17. ISSN 1392-2114.
95. KASS, M., WITKIN, A., and D. TERZOPOULOS. Snakes: Active Contour Models. In *International Journal of Computer Vision*. 1988, 1(4), 321-331. ISSN 0920-5691.
96. KIER, C., CYRUS, C., SEIDEL, G., HOFMANN, U. G., AACH, T. Segmenting the Substantia Nigra in Ultrasound Images for Early Diagnosis of Parkinson's Disease. In *International Journal of Computer Assisted Radiology and Surgery*. 2007, 2, 83-85. ISSN 1861-6410.
97. KIER, C., SEIDEL, G., BREGEMANN, N., HAGENAH, J., KLEIN, C., AACH, T., MERTINS, A. Transcranial Sonography as Early Indicator for Genetic Parkinson's Disease. In *4<sup>th</sup> European Conference of IFMBE*, Belgium, Antwerpen, November 23-29, 2008, 2009. pp. 456-459.
98. KONOFAGOU, E. E. Optimization of the Ultrasound-Induced Blood-Brain Barrier Opening. In *Theranostics*. 2012, 2(12), 1223-1237. ISSN 1838-7640.
99. KOVESI, P. *Invariant Measures of Image Features from Phase Information*. Ph.D. thesis, University of Western Australia, 1996.

100. KRISIAN, K., WESTIN, C. F., KIKINIS, R., VOSBURGH, K. Oriented Speckle Reducing Anisotropic Diffusion. In *IEEE Transactions on Image Processing*. 2007, 16(5), 1412-1424. ISSN 1057-7149.
101. KWON, J. H., KIM, J. S., KANG, D. W., BAE, K. S., KWON, S. U. The Thickness and Texture of Temporal Bone in Brain CT Predict Acoustic Window Failure of Transcranial Doppler. In *Journal of Neuroimaging*. 2006, 16(4), 347-352. ISSN 1552-6569.
102. LARRAT B., PERNOT M., MONTALDO G., FINK M., TANTER M. MR-Guided Adaptive Focusing of Ultrasound. In *IEEE Transactions on Ultrasonics, Ferroelectrics and Frequency control*. 2010, 57(8), 1734-1747. ISSN 0885-3010.
103. LAUČKAITĖ, K., RASTENYTĖ, D., ŠURKIENĖ, D., VAITKUS, A., SAKALAUŠKAS, A., LUKOŠEVIČIUS, A., GLEIZNIENĖ, R. Specificity of Transcranial Sonography in Parkinson Spectrum Disorders in Comparison to Degenerative Cognitive Syndromes. In *BMC Neurology*. 2012, 12, 12. ISSN 1471-2377.
104. LIN, N., YU, W.C., and J. S. DUNCAN. Combinative Multi-Scale Level Set Framework for Echocardiographic Image Segmentation. In *Medical Image Analysis*. 2003, 7(4), 529-537. ISSN 1361-8415.
105. LIU, X., and J. TANG. Mass Classification in Mammograms Using Selected Geometry and Texture Features, and a New SVM-Based Feature Selection Method. In *IEEE Systems Journal*. 2014, 8(3), 910-920. ISSN 1932-8184.
106. LOGISHETTY, K., and K. R. CHAUDHURI. Parkinson's disease. In *Movement Disorders in Clinical Practice*. Edited by: Chaudhuri K. R., Ondo W. G. London: Springer; 2010.
107. LORENSEN, W. E., and E. CLINE HARVEY. Marching Cubes: A High Resolution 3D Surface Construction Algorithm. In *ACM Computer Graphics*, 21(4), 163-169. ISSN 0097-8930.
108. MAHALANOBIS, P.C. On the Generalised Distance in Statistics. In *Proceedings of the National Institute of Science of India*, 1936. pp. 49-55.
109. MARIANI, B., JIMENEZ, M. C., VINGERHOETS, F. J. G., AMINIAN, K. On-Shoe Wearable Sensors for Gait and Turning Assessment of Patients with Parkinson's Disease. In *IEEE Transactions on Biomedical Engineering*. 2013, 60(1), 155-158. ISSN 0018-9294.
110. MCDANNOLD, N., ARVANITIS, C. D., VYKHODTSEVA, N., LIVINGSTONE, M. S. Temporary Disruption of the Blood-Brain Barrier by Use of Ultrasound and Microbubbles: Safety and Efficacy Evaluation in Rhesus Macaques. In *Cancer Research*. 2012, 1-12. ISSN 0008-5472.
111. MEHNERT, S., REUTER, I., SCHEPP, K., MAASER, P., STOLZ, E., KAPS, M. Transcranial Sonography for Diagnosis of Parkinson's Disease. In *BMC Neurology*. 2010, 10(9), 1-7. ISSN 1471-2377.
112. MULET-PARADA, M., and J. A. NOBLE. 2D+T Acoustic Boundary Detection in Echocardiography. In *Medical Image Analysis*. 2000, 4, 21-30. ISSN 1361-8415.
113. Netter, F. H. *Atlas der Anatomie*. Elsevier GmbH, Urban & Fischer Verlag, ISBN 978-3-437-41603-3, 2011.
114. NOBLE, J. A., and D. BOUKERROUI. Ultrasound Image Segmentation: A Survey. In *IEEE Transactions on Medical Imaging*. 2006, 25(8), 987-1010. ISSN 1558-0062.
115. NOGUERA, A. G. *Propagation of Ultrasound through Freshly Excised Human Calvarium*, Master thesis, University of Nebraska 2012.

- 116.OKAWA, M., MIWA, H., KAJIMOTO, Y., et al. Transcranial Sonography of the Substantia Nigra in Japanese Patients with Parkinson's Disease or Atypical Parkinsonism: Clinical Potential and Limitations. In *Internal Medicine Journal*. 2007, 46, 1527–1531. ISSN 1445-5994.
- 117.OLANOW, C. W., STERN, M. B., and K. SETHI. The Scientific and Clinical Basis for the Treatment of Parkinson Disease. In *Neurology*. 2009, 72(Suppl4), 1-136. ISSN 0028-3878.
- 118.OSMANSKI, B. F., MONTALDO, G., TANTER, M., FINK, M. Aberration Correction by Time Reversal of Speckle Noise. In *IEEE Transactions on Ultrasonics, Ferroelectrics and Frequency Control*. 2012, 59 (7), 1575-1582. ISSN 0885-3010.
- 119.OTSU, N. A Threshold Selection Method From Gray-Level Histograms. In *IEEE Trans. Sys., Man., Cyber*. 1979, 9(1), 62–66. ISSN 1083-4419.
- 120.PAULY, O., AHMADI, S. A., PLATE, A., BOETZEL, K., NAVAB, N. Detection of Substantia Nigra Echogenicities in 3D Transcranial Ultrasound for Early Diagnosis of Parkinson Disease. In *Proc. International Conference on Medical Image Computing and Computer Assisted Intervention (MICCAI)*, Nice (FR), October 01-05, 2012. pp. 443-450.
- 121.PETROUDI, S., LOIZOU, C., PANTZIARIS, M., PATTICHIS, C. Segmentation of the Common Carotid Intima-Media Complex in Ultrasound Images Using Active Contours. In *IEEE Transactions on Biomedical Engineering*. 2012, 59(11), 3060-3069. ISSN 0018-9294.
- 122.PICHARDO, S., SIN, W. V., and K. HYNYNEN. Multi-Frequency Characterization of the Speed of Sound and Attenuation Coefficient for Longitudinal Transmission of Freshly Excised Human Skulls. In *Physics in Medicine and Biology*. 2011, 56, 219-250. ISSN 0031-9155.
- 123.PLATE, A., AHMADI, S. A., PAULY, O., KLEIN, T., NAVAB, N., BOTZEL, K. Three-Dimensional Sonographic Examination of the Midbrain for Computer-Aided Diagnosis of Movement Disorders. In *Ultrasound in Medicine and Biology*. 2012, 38(12), 2041-2050. ISSN 0301-5629.
- 124.REFAEILZADEH, P., TANG, L., and LIU H. Cross-Validation. In *Encyclopedia of Database Systems*, 2009. ISBN 978-0-387-35544-3.
- 125.ROHLING, R. N. *3D Freehand Ultrasound: Reconstruction and Spatial Compounding*. PhD. thesis, 1998.
- 126.SAKALAUŠKAS, A., LUKOŠEVIČIUS, A., and K. LAUČKAITĖ. Texture Analysis of Transcranial Sonographic Images for Parkinson Disease Diagnostics. In *Ultragarsas*. 2011, 66(3), 32-36. ISSN 1392-2114.
- 127.SAKALAUŠKAS, A., LUKOŠEVIČIUS, A., and LAUČKAITĖ, K. Semi-Automatic Method for Delineation of Midbrain in Transcranial Ultrasound Images. In *Biomedical Engineering - 2013: Proceedings of 17<sup>th</sup> International Conference*, Kaunas, November, 26-27, 2013. pp. 91-96.
- 128.SAKALAUŠKAS, A., LUKOŠEVIČIUS, A., LAUČKAITE, K., JEGELEVIČIUS, D., RUTKAUSKAS, S. Automated Segmentation of Transcranial Sonographic Images in the Diagnostics of Parkinson's Disease. In *Ultrasonics*. 2013, 53(1), 111-121. ISSN 0041-624X.
- 129.SANZARO, E., IEMOLO, F., DURO, G., MALFERRARI, G. A New Assessment Tool for Parkinson Disease: The Nigral Lesion Load Obtained by Transcranial Sonography. In *Journal of Ultrasound in Medicine*. 2014, 33(9), 1635-1640. ISSN 0278-4297.

130. SCHWARZ S.T., RITTMAN, T., GONTU, V., PAUL, S., NIN BAJAJ, M., DOROTHEE, P. T1-Weighted MRI Shows Stage-Dependent Substantia Nigra Signal Loss in Parkinson's Disease. In *Movement Disorders*. 2011, 26(9), 1633-1638. ISSN 1531-8257.
131. ŠKOLOUDIK, D., FADRNA, T., BARTOVA, P., LANGOVA, K., RESSNER, P., ZAPLETALOVA, O., HLUSTIK, P., HERZIG, R., KANNOVSKY, P. Reproducibility of Sonographic Measurement of the Substantia Nigra. In *Ultrasound in Medicine and Biology*. 2007, 33, 1347-1352. ISSN 0301-5629.
132. ŠKOLOUDIK, D., JELÍNKOVÁ, M., BLAHUTA J., ČERMÁK, P., SOUKUP, T., BĀRTOVÁ, P. Transcranial Sonography of the Substantia Nigra: Digital Image Analysis. In *American Journal of Neuroradiology*. 2014, 35 (12), 2273-2278. ISSN 0195-6108.
133. ŠPEČKAUSKIENĖ, V. *Informacinio klinikinių sprendimų metodo sudarymas ir tyrimas*. PhD. thesis. Kaunas: Technologija, 2011.
134. SZCZYPINSKI, P., STRZELECKI, M., and A. MATERKA. MaZda - a Software for Texture Analysis. In *Proc. of ISITC*, Republic of Korea, November 23, 2007. pp. 245-249.
135. SZCZYPINSKI, P., STRZELECKI, M., MATERKA, A., KLEPACZKO, A. Mazda-A Software Package for Image Texture Analysis. In *Computer Methods and Programs in Biomedicine*. 2009, 94(1), 66-76. ISSN 0169-2607.
136. TAKIUCHI, S., RAKUGI, H., HONDA, K., MASUYAMA, T., HIRATA, N., ITO, H., SUGIMOTO, K., YANAGITANI, Y., MORIGUCHI, K., OKAMURA, A., HIGAKI, J., OGIHARA, T. Quantitative Ultrasonic Tissue Characterization Can Identify High-Risk Atherosclerotic Alteration in Human Carotid Arteries. In *Circulation*. 2000, 102(7), 766-70. ISSN 0009-7322.
137. TANOUE, H., HAGIWARA, Y., KOBAYASHI, K., SAIJO, O. Ultrasonic Tissue Characterization of Prostate Biopsy Tissues by Ultrasound Speed Microscope. In *IEEE Annual International Conference EMBC*, Boston, August 30-September 3, 2011. pp. 8499-8502.
138. TANTER, M., THOMAS, J. L., and M. FINK. Ultrasonic Focusing and Steering Through the Skull: Toward Brain Imaging. In *The Journal of the Acoustical Society of America*. 1998, 103 (5), 2792-2792. ISSN 0001-4966.
139. TRUMPAITIS J., JURKONIS R., IMBRASIENĖ D., GRIZICKAITĖ A., PAUNKSNIS A. Application of Ultrasound Spectral Analysis for Intraocular Tissues Differentiation. In *Journal of Vibroengineering*. 2014, 16(7), 3586-3594. ISSN 1392-8716.
140. TSIAPARAS, N. N., GOLEMATI, S., ANDREADIS, I., STOITSIS, J. S., VALAVANIS, I., NIKITA, K. S. Comparison of Multiresolution Features for Texture Classification of Carotid Atherosclerosis From B-Mode Ultrasound. In *IEEE Transactions on Information Technology in Biomedicine*. 2011, 15(1), 130-137. ISSN 1089-7771.
141. VAILIONYTĖ, S., SAKALAUŠKAS, A., and A. LUKOŠEVIČIUS. Analysis of Midbrain Area Echogenicity in Diagnostic Transcranial Ultrasound Images. In *Biomedical Engineering 2014: Proceedings of the 18<sup>th</sup> International Conference*, Lithuania, Kaunas, 27-28 November, 2014. pp. 158-161.
142. VIGNON, F., AUBRY, J. F., TANTER, M., FINK, M. High Resolution Ultrasonic Brain Imaging: Adaptive Focusing Based on Twin-Arrays. In *IEEE International Conference on Acoustics, Speech, and Signal Processing*, March 18-23, 2005. pp. 973-976.

143. VIGNON, F., SHI, W., SHAMDASANI, V., KALMAN, P., MAXWELL, D., POWERS, J. Transcranial Image Quality Improvement with a Multi-Step Approach. In *IEEE International Ultrasonics Symposium*, Prague, July 21-23, 2013. pp. 1284-1287.
144. VIGNON, F., SHI, W. T., ERKAMP, R., RADULESCU, E., SHAMDASANI, V., POWERS, J. E. Mapping Skull Attenuation for Optimal Probe Placement in Transcranial Ultrasound Applications. In *IEEE International Ultrasonics Symposium Proceedings*, 2009. pp. 2336-2339.
145. VIGNON, F., SHI, W. T., YIN, X., HOELSCHER, T., POWERS, J. Implications of Mode Conversion on Transcranial Ultrasound Imaging. In *IEEE Ultrasonics Symposium*, Rome, September 20-23, 2007. pp. 1752-1755.
146. VIGNON, F., WILLIAM, T. S., BURCHER, M.R., POWERS, J. E. Determination of Temporal Bone Isoplanatic Patch for Transcranial Phase Aberration Correction. In *IEEE International Ultrasonics Symposium Proceedings*, Beijing, November 2-5, 2008. pp. 1286-1289.
147. VLAAR, M. M. A, DE NIJS, T., VAN KROONENBURGH, M. J. P. G., MESS, W. H., WINOGRODZKA, A., TROMP, S. C., WEBER, W. E. J. The Predictive Value of Transcranial Duplex Sonography for the Clinical Diagnosis in Undiagnosed Parkinsonian Syndromes: Comparison with SPECT Scans. In *BMC Neurology*. 2008, 8, 42. ISSN 1471-2377.
148. VLAAR, M. M. A, VAN KROONENBURGH, M. J. P. G., KESSELS, A. G. H., WEBER, W. E. J. Meta-Analysis of the Literature on Diagnostic Accuracy of SPECT in Parkinsonian Syndromes. In *BMC Neurology*. 2007, 7(27). ISSN 1471-2377.
149. WALTER U. Substantia Nigra Hyperechogenicity Is a Risk Marker of Parkinson's Disease: No. In *Journal of Neural Transmission*. 2011, 118, 607-612. ISSN 0300-9564.
150. WALTER U., KIRSCH, M., WITTSTOCK, M., MÜLLER, J. U., BENECKE, R., WOLTERS A. Transcranial Sonographic Localization of Deep Brain Stimulation Electrodes Is Safe, Reliable and Predicts Clinical Outcome. In *Ultrasound in Medicine and Biology*. 2011, 37(9), 1382-1391. ISSN 0301-5629.
151. WALTER, U., BEHNKE, S., EYDING, J., NIEHAUS, L., POSTERT, T., SEIDEL, G., et al. Transcranial Brain Parenchyma Sonography in Movement Disorders: State of the Art. In *Ultrasound in Medicine and Biology*. 2007, 33, 15-25. ISSN 0301-5629.
152. WALTER, U., KANOWSKI, M., KAUFMANN, J., GROSSMANN, A., BENECKE, R., NIEHAUS, L. Contemporary Ultrasound Systems Allow High-Resolution Transcranial Imaging of Small Echogenic Deep Intracranial Structures Similarly as MRI: A Phantom Study. In *NeuroImage*. 2008, 40, 551 – 558. ISSN 1053-8119.
153. WALTER, U., KLEIN, C., and R. HILKER. Brain Parenchyma Sonography Detects Preclinical Parkinsonism. In *Movement Disorders*. 2004, 19, 1445-1449. ISSN 1531-8257.
154. WHITE, P. J., CLEMENT, G. T., and K. HYNYNEN. Transcranial Ultrasound Focus Reconstruction with Phase and Amplitude Correction. In *IEEE Transactions on Ultrasonics, Ferroelectrics, and Frequency Control*. 2005, 52(9), 1518-1522. ISSN 0885-3010.

155. WHITE, P. J., CLEMENT, G. T., and K.HYNYNEN. Longitudinal and Shear Mode Ultrasound Propagation in Human Skull Bone. In *Ultrasound in Medicine and Biology*. 2006, 32, 1085-1096. ISSN 0301-5629.
156. *World Health Organization. Neurological Disorders: Public Health Challenges*. WHO Press, 2008.
157. XU, C., and J. L. PRINCE. Snakes, Shapes and Gradient Vector Flow. In *IEEE Transactions on Image Processing*. 1998, 7, 359–369. ISSN 1057-7149.
158. YAN, P., XU, S., TURKBAY, B., KRUECKER, J. Adaptively Learning Local Shape Statistics for Prostate Segmentation in Ultrasound. In *IEEE Transactions on Biomedical Engineering*. 2011, 58(3), 633-641. ISSN 0018-9294.
159. YU, Y., and S. T. ACTON. Speckle Reducing Anisotropic Diffusion. In *IEEE Transactions on Image Processing*. 2002, 11(11), 1260-1270. ISSN 1057-7149.
160. YUE, Y., CROITORU, M. M., BIDANI, A., ZWISCHENBERGER, J. W. CLARK, J. R. Nonlinear Multiscale Wavelet Diffusion for Speckle Suppression and Edge Enhancement in Ultrasound Images. In *IEEE Transactions on Medical Imaging*. 2006, 25(3), 297-311. ISSN 1558-0062.

### **LIST OF THE PUBLICATIONS**

#### **Publications referred in Journals from the master list of Thomson Reuters Web of Science (with impact factor)**

1. Sakalauskas, A., Lukoševičius, A., Laučkaitė, K., Jegelevičius, D., Rutkauskas, S. Automated Segmentation of Transcranial Sonographic Images in the Diagnostics of Parkinson's Disease // *Ultrasonics*. Amsterdam: Elsevier Science. ISSN 0041-624X. 2013, vol. 53, iss. 1, pp. 111-121. DOI: 10.1016/j.ultras.2012.04.005. [Science Citation Index Expanded (Web of Science); Academic Search Premier; Compendex; Inspec; MEDLINE; Science Direct]. [IF (E): 1,805 (2013)].
2. Laučkaitė, K., Rastenytė, D., Šurkienė, D., Vaitkus, A., Sakalauskas, A., Lukoševičius, A., Gleiznienė, R., Specificity of Transcranial Sonography in Parkinson Spectrum Disorders in Comparison to Degenerative Cognitive Syndromes // *BMC Neurology*. London: BioMed Central. ISSN 1471-2377. 2012, Vol. 12, Article No. 12, pp. 1-14. DOI: 10.1186/1471-2377-12-12. [Science Citation Index Expanded (Web of Science); Academic Search Complete]. [IF (E): 2,564 (2012)].

#### **Publications in Journals from the other international databases**

1. Sakalauskas, A., Lukoševičius, A., Laučkaitė, K. Transcranial Echoscapy for Diagnostic of Parkinson Disease: Technical Constraints and Possibilities // *Ultragarsas = Ultrasound* / Kauno technologijos universitetas. Kaunas: Technologija. ISSN 1392-2114. 2010, Vol. 65, No. 4, pp. 47-50. [INSPEC].
2. Sakalauskas, A., Lukoševičius, A., Laučkaitė, K. Texture Analysis of Transcranial Sonographic Images for Parkinson Disease Diagnostics //

*Ultragarsas = Ultrasound* / Kauno technologijos universitetas. Kaunas: Technologija. ISSN 1392-2114. 2011, Vol. 66, No. 3, pp. 32-36. [INSPEC].

### **Publications in Reviewed Proceedings of International Scientific Conferences**

1. Sakalauskas, A., Lukoševičius, A., Laučkaitė, K., Rutkauskas, S., Rastenytė, D. Automatic Segmentation of Substantia Nigra Area in Transcranial Sonography Images // *Biomedical Engineering - 2011: Proceedings of International Conference, Kaunas University of Technology, 27, 28 October 2011* / Kaunas University of Technology. Kaunas: Technologija. ISSN 2029-3380. 2011, pp. 46-52.
2. Laučkaitė, K., Gleiznienė, R., Sakalauskas, A., Šurkienė, D., Rastenytė, D., Lukoševičius, A. Imaging of Substantia Nigra Degeneration by Transcranial Sonography and Magnetic Resonance in Parkinson's Disease // *Biomedical Engineering - 2011: Proceedings of International Conference, Kaunas University of Technology, 27, 28 October 2011* / Kaunas University of Technology. Kaunas: Technologija. ISSN 2029-3380. 2011, pp. 53-56.
3. Kybartaitė, A., Sakalauskas, A., Laučkaitė, K., Lukoševičius, A. Information Collection and Management for Diagnostics of Parkinson's Disease // *Biomedical Engineering - 2011: Proceedings of International Conference, Kaunas University Of Technology, 27, 28 October 2011* / Kaunas University of Technology. Kaunas: Technologija. ISSN 2029-3380. 2011, pp. 57-60.
4. Sakalauskas, A., Lukoševičius, A., Laučkaitė, K., Semi-Automatic Method for Delineation of Midbrain in Transcranial Ultrasound Images // *Biomedical Engineering - 2013: Proceedings of 17<sup>th</sup> International Conference, Kaunas University of Technology, 28-29 November, 2013* / Kaunas University of Technology Biomedical Engineering Institute. Kaunas: Technologija. ISSN 2029-3380. 2013, pp. 91-96.
5. Vailionytė, S., Sakalauskas, A., Lukoševičius, A., Analysis of Midbrain Area Echogenicity in Diagnostic Transcranial Ultrasound Images // *Biomedical Engineering 2014: Proceedings of the 18<sup>th</sup> International Conference, 27-28 November, 2014, Kaunas, Lithuania* / Kaunas University of Technology Biomedical Engineering Institute. Kaunas: Technologija. ISSN 2029-3380. 2014, pp. 158-161.

### **Publications in Reviewed Proceedings of Lithuanian Scientific Conferences**

1. Sakalauskas, A., Lukoševičius, A., Laučkaitė, K., Špečkauskienė, V. Transkranijinės sonografijos vaizdų apdorojimo sistema galvos smegenų audinio echogeniškumui vertinti // *Fizinių ir technologijos mokslų tarpdalykiniai tyrimai [elektroninis išteklius]: 5-oji jaunųjų mokslininkų konferencija, 2015 m. vasario 10 d: pranešimų tezės* / Lietuvos mokslų akademija. [S.l.: s.n, 2015]. psl. 64-65.
2. Laučkaitė, K., Sakalauskas, A., Šurkienė, D., Gleiznienė, R., Kuprionis, G., Rastenytė, D. *Transkranijinės sonografijos vertė diagnozuojant Parkinsono*

*ligą. Mokslas - sveikatai [elektroninis išteklius]: V nacionalinė doktorantų mokslinė konferencija, 2012 m. balandžio 11 d., Kaunas, [Lietuva]: konferencijos tezių rinkinys. Kaunas: Lietuvos sveikatos mokslų universiteto Leidybos namai, 2012. psl. 75.*

## APPENDIX 1:

The main features used for the quantitative evaluation of the echogenicity degree are presented in Table 3.3. This appendix gives a more detailed description of the used features (very common and trivial parameters such as area, perimeter, mean intensity value are not explained).

**Table 3.3** Quantitative features used for the echogenicity estimation

REGION	1. ½ ROI	2. RROI	3. SN
FEATURES	1. Area 2. Skewness 3. Kurtosis 4. Entropy 5. Moment of Inertia (MoI) 6. 1 <sup>st</sup> Hu moment invariant 7. EI (Školoudik et al., 2014) 8. Mean intensity 9. Length of EI curve	1. Otsu criterion 2. Aspect Ratio 3. RROI entropy 4. Area 5. Circularity 6. Perimeter 7. EI 8. Length of EI curve 9. Mean Intensity	1. Area 2. Circularity 3. Perimeter 4. Entropy
	<b>Mixed features</b>		
	1. Ratio of mean intensities in RROI / ½ROI 2. Contrast: mean intensities ROI / Surroundings 3. Areas Ratio SN / RROI 4. Areas Ratio SN / ½ROI 5. Areas Ratio RROI / ½ROI 6. Entropy Ratio RROI / ½ROI 7. SN area with a RROI constraint		

Skewness is a measure of asymmetry of distribution. It was expected that the intensity distribution would be closer to the symmetric in abnormal case. Skewness could be expressed:

$$\psi = \frac{1}{3} \cdot \frac{\sum_{i=1}^n (I_i - \bar{I})}{n \cdot \sigma^2}, \quad (55)$$

where  $n$  – number of pixels in region 1. Region,  $\bar{I}$  - mean value of intensities in the region (½ ROI),  $\sigma$  – variance.

Kurtosis measures the degree of peakedness of a distribution:

$$\kappa = \frac{1}{n \cdot \sigma^2} \cdot \sum_{i=1}^n (I_i - \bar{I})^4 - 3. \quad (56)$$

Entropy is the measure of randomness of the image (see formula 38). In case of hyperechogenicity, the number of pixels having relatively higher intensity values should increase, thus increasing all the range so that the increment of entropy could be expected as well.

Moment of inertia and 1<sup>st</sup> Hu moment invariant were relatively successfully used for the hyperechogenicity recognition by previous authors (Kier et al., 2009; Vailionyte et al., 2014). These features are introduced in the 1.6.2.2 subsection, see formulas (10) – (13). Moment invariants are used for the pattern recognition even if it is rotated, shifted or scaled. This makes the moments into an attractive tool for the pattern recognition.

The same Otsu variance separation criterion was used as a potential parameter, since it could be expected that, in abnormal case, it should be easier to find the distinction between two distributions (increment of inter-class variance). For details, see formulas (41) – (43) and description in subsection 3.3.2.

It is known that the SN region of healthy subjects is stripe-shaped structure from anatomical prior; meanwhile, in abnormal cases, it is expanding. It was hypothesized that the expansion has a dominating direction ( $s_y$ ). Therefore, the circularity and aspect ratio parameters were employed. Aspect Ratio:

$$AR = \frac{s_x}{s_y}, \quad (57)$$

where  $s_x, s_y$  are established scale parameters obtained during RROI segmentation. Circularity is the measure of roundness showing how the shape is close to a circle (in the range 0 – 1). It could be expressed:

$$C = \frac{4\pi S}{P^2}, \quad (58)$$

where  $S$  – area of the region,  $P$  – perimeter of the contour marking region boundary. The circularity and perimeter metrics were as well used in the case of SN region. It should be mentioned that, in some cases, SN extraction algorithm finds few connected regions. In these cases, the largest segment of SN was used for the evaluation of circularity and perimeter.

The relative contrast between the midbrain region and surrounding tissue was employed for the global contrast estimation expecting that the midbrain hyperechogenicity could reduce the contrast. Moreover, it could serve as an image quality criterion for the categorization of the input images. The contrast is expressed as:

$$Contrast = \frac{\overline{I_{ROI}}}{I_{SR}}, \quad (59)$$

the ratio between the mean intensity inside ROI (*mesencephalon*) and the surrounding tissue  $I_{SR}$  (basal cisterns). The reference (SR) region was extracted by applying 20% increment of the ROI contour scale. An example of the regions used for the contrast evaluation is presented in Fig. A1. (B).

Novel EI parameter (area under the curve) proposed by Sklodudek et al. (2014) was as well included into the list of potential features. Moreover, the additional parameter from the EI curve was derived. The length of the EI curve

between the intensity values giving the relative changes of the area was estimated. An example of the curve used for the EI estimation is presented in Fig. A1 (A).

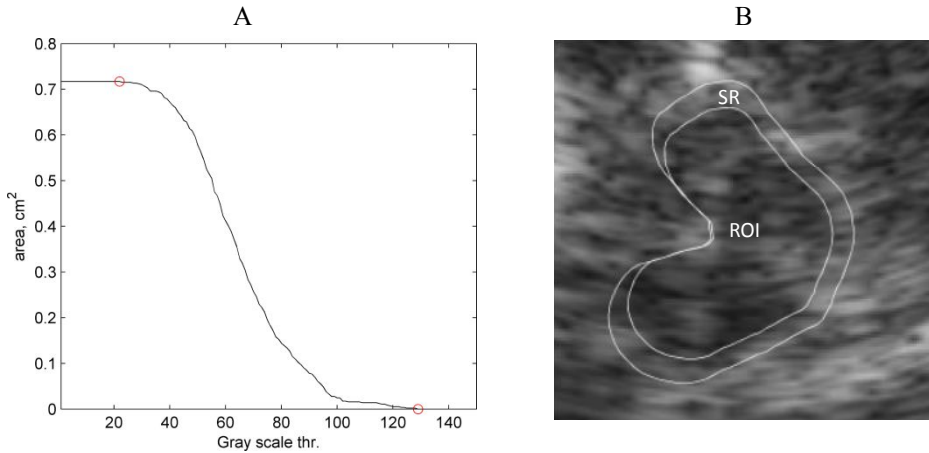


**Fig. A1.** The example (A) is the curve used for *EI* and *EI curve length* estimation; (B) is an example of the regions used for the contrast estimation (ROI – midbrain region, SR – surroundings)

Moreover, 7 mixed parameters measuring relative areas, intensity levels and entropy between the extracted regions ( $\frac{1}{2}$  ROI, RROI and SN area) were proposed.

One of the most informative metrics for echogenicity evaluation from the tested was the “SN area with a RROI constraint”. SN area with a RROI constraint is a mixed feature obtained by combining the results of SN and RROI extraction algorithms. All the pixels outside the RROI region extracted in the SN segmentation stage were filtered out.